博士論文

Search for neutralino production in final states with low transverse momentum muon in pp collision at $\sqrt{s} = 13$TeV

(重心系エネルギー 13TeV の陽子陽子衝突における終状態に低運動量ミューオンをもつニュートラリーノ生成過程の探索)

令和 4 年 1 月

神戸大学大学院 理学研究科
日比 宏明

Abstract

The Standard Model(SM) is the successful theory to describe the current particle physics. The prediction from SM is consistent with most of the experimental results. However, there are still several unresolved problems, such as the hierarchy problem related to the Higgs mass, the grand unification of forces, and the identity of dark matter. Recently, the Fermilab Muon g-2 Experiment has reported that the muon magnetic moment deviates from the SM prediction by 4.2σ. This result may be a sign of new physics.

Supersymmetry (SUSY) with the *R*-parity conservation is one of the most elegant extension of SM that can solve the above problems. The theory suggests the existence of superpartners which are particles whose spin differs from the SM particles by 1/2. For electroweak gauge bosons and Higgs bosons, eight superpartners, called neutralinos and charginos, are introduced.

This thesis report an updated result of a search for neutralino using the decay mode that next-to-lightest neutralino ($\tilde{\chi}_2^0$) decays into lightest neutralino ($\tilde{\chi}_1^0$) and two muons. Also, the target phase space is the region where the mass difference between $\tilde{\chi}_1^0$ and $\tilde{\chi}_2^0$ is a few GeV. This thesis uses data collected by the ATLAS detector in 2015-2018 corresponding to the integrated luminosity of 139 fb^{-1}. In the past search in the ATLAS experiment, the bottleneck was the poor identification efficiency for muons with low transverse momentum (low-p_T). To solve the problem, a new muon identification algorithm dedicated to low-p_T muons (Low p_T calo tag muon ID) has been developed for this analysis. Also, Deep Neural Networks, which is one of the machine learning techniques, are introduced to improve the sensitivity for the neutralinos.

Finally, the discovery and the exclusion test are performed. No significant excess over expected background is observed, and thus exclusion limits are set for neutralino as a function of $\tilde{\chi}_2^0$ mass and $\Delta m(\tilde{\chi}_2^0, \tilde{\chi}_1^0)$. For the scenario which the main component of $\tilde{\chi}_1^0$ is superpartners of Higgs (Higgsino), $\tilde{\chi}_2^0$ is excluded up to 125 GeV on $\tilde{\chi}_2^0$ mass at the region that $\Delta m(\tilde{\chi}_2^0, \tilde{\chi}_1^0)$ is 3 GeV. This is the result of the world's highest sensitivity.

Contents

List of Figures

List of Tables

1. Introduction

What is the origin of matter? What interactions do work between them? These are one of the ancientest age-old questions. In modern science, the Standard Model(SM)[5] of particle physics is known as the theory closest to the answer. The Lagrangian of SM, shown in Fig.1.1, describes the universe well and gives us well-consistent predictions with most of the results of the experiments.

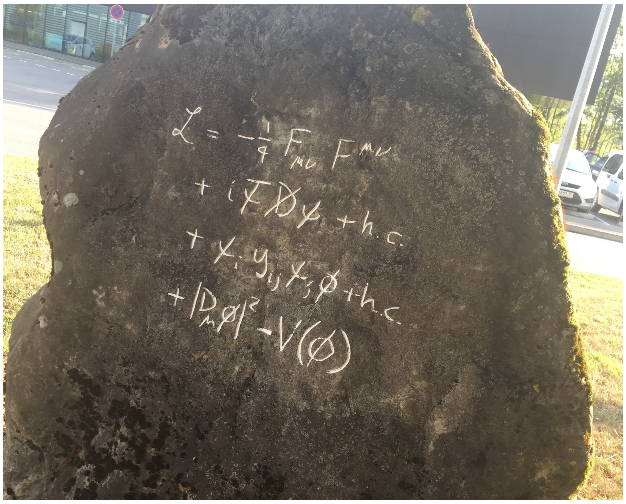

Figure1.1 One of the best formulas to describe the world

However, there are still some unsolved problems, such as Higgs' hierarchy problem and dark matter, and so on. Therefore, it is obvious that SM is not perfect. The SUper SYmmetry Theory (SUSY)[6] is one of the most promising theories that can solve these problems. In this theory, an undiscovered particle called the SUSY particle is introduced to make a pair with each particle in the SM. In other words, the discovery of such a particle is proof of the SUSY theory.

Recently, a deviation of 4.2 σ from the SM expectation has been reported in measurements of the muon magnetic moment[7]. The deviation may be a sign of SUSY. If neutralino ($\tilde{\chi}_1^0$) is the lightest SUSY particle and its mass is less than 500 GeV, this muon magnetic moment deviation can be explained. Moreover, if the Dark matter is $\tilde{\chi}_1^0$, the mass difference between the first and second lightest neutralinos, $\Delta m(\tilde{\chi}_1^0, \tilde{\chi}_2^0)$ is suggested to be less than O(10GeV). On the other hand, the results of direct SUSY searches using LEP[8] also suggest that the $\tilde{\chi}_1^0$ mass is above 92.4 GeV. Consequently, the phase space is strictly limited by considering the multi experiments; $m(\tilde{\chi}_1^0)$

should be between 92.4 GeV and 500 GeV and the $\Delta m(\tilde{\chi}_1^0, \tilde{\chi}_2^0)$ should be less than $O(10\text{GeV})$.

Currently, the only experiment that can approach this region is the world's highest energy proton-proton collision experiment using the Large Hadron Collider (LHC), such as the ATLAS experiment. In the previous analysis[9][10], the ATLAS experiment has explored the region below $O(0.1\text{GeV})$ and above $O(1\text{GeV})$. However, the region where $\Delta m(\tilde{\chi}_1^0, \tilde{\chi}_2^0)$ is 1 GeV to 5 GeV has not been explored yet since the LEP result. The main difficulty in this region is the poor muon identification efficiency at the low momentum region, because such muons cannot reach the muon spectrometer used to identify them.

In this thesis, a new dedicated identification algorithm for low momentum muon using tracker and calorimeter information has been developed for the ATLAS experiment. This algorithm discriminates muon from other particles using the difference of behavior in the calorimeter. In this identification algorithm, Deep Neural Network (DNN)[11], a class of machine learning algorithms, is used to achieve the high performance. The new algorithm allows us to search the region of $\Delta m(\tilde{\chi}_1^0, \tilde{\chi}_2^0)$ from 1 to 5 GeV. In this search of neutralinos, it is important to discriminate SUSY signal from background efficiently to achieve high sensitivity. However, it is not easy to establish an optimized search method by one DNN algorithm since different kinematics are predicted for different Δm regions. Therefore, pNN, a kind of DNN, is employed. The pNN uses not only measured parameters such as four-momentum of muons but also physics parameter Δm as the input. It makes discrimination performance efficient for all over Δm region. Finally, the results of this neutralino search with the 13 TeV pp-collision data of 139 fb^{-1}, and discuss a SUSY model.

Outline of the dissertation

In this thesis, a search for neutralino production with small Δm is reported. The search uses 139 fb^{-1} of $\sqrt{s} = 13$ TeV proton-proton collision data collected in ATLAS experiment. The outline of this thesis is summarized below.

- Chapter 2 describes theoretical background, especially about motivation for SUSY.
- Chapter 3 describes the LHC-ATLAS experiment.
- Chapter 4 describes data and MC samples used for the analysis.
- Chapter 5 describes definition of the objects in the analysis.
- Chapter 6 describes newly developed low-p_T muon identification algorithm.
- Chapter 7 describes event selection to maximize the sensitivity for neutralino.
- Chapter 8 describes how to estimate the background.

- Chapter 9 describes the systematic uncertainty for background and signal.
- Chapter 10 describes statistical treatment and statistical test for discovery and exclusion of neutralino.
- Chapter 11 describes the result and impact on SUSY.

2. Theoretical Background

This chapter describes the supersymmetry theory, which is the target of this thesis, especially models with neutralino as a LSP, the motivation and current limitations of the theory are summarized. Finally, the strategy to test the remaining possible phase space is discussed.

2.1 Standard Model

The Standard Model (SM) is a theory that can explain almost all the experimental results in modern particle physics. Figure 2.1 shows particles in SM.

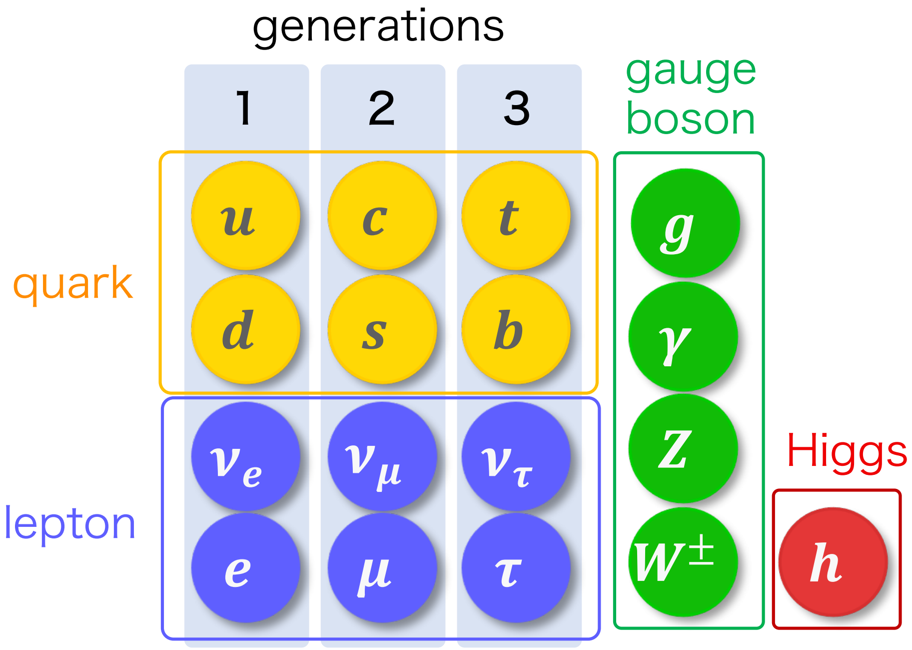

Figure2.1 SM particles

In SM, 12 fermions, four gauge bosons, and one Higgs boson are introduced. The fermions are the elementary particles that make up matter and are divided into quarks and leptons based on the characteristics of their interactions. Strong, weak, and electromagnetic interaction act on quarks, while weak and electromagnetic interaction act on leptons. Gauge bosons are introduced as mediators for each interaction: gluon for the strong interaction, Z boson and W boson for the weak interaction, and photon for the electromagnetic interaction. Finally, the Higgs boson, a complex scalar field, is introduced to obtain mass to the particle. Using the field of these particles, the Lagrangian is described as follows.

$$\begin{aligned}\mathcal{L} = &-\frac{1}{4}F_{\mu\nu}F^{\mu\nu} \\ &+ i\bar{\psi}\,\not{D}\psi \\ &+ y\bar{\psi}\psi\phi \\ &+ |D\phi|^2 + V(\phi)\end{aligned} \tag{2.1}$$

Here, $F_{\mu\nu}$ represents the strength of the gauge field, and ψ, ϕ are the fermion field and the Higgs field, respectively. The first term describes the momentum and self-coupling of the gauge boson. The second term describes the momentum and interaction of the fermion. The third term describes the Yukawa coupling between Higgs and fermions. The fourth term describes the Higgs momentum and its interaction with gauge boson. The last term, $V(\phi)$, is a function of the Higgs potential. According to the form of this function, Higgs has a vacuum expectation value (VEV). This mechanism is called the Brout–Englert–Higgs mechanism[12, 13]. The term with VEV gives mass to the fermion and gauge particles.

One of the most elegant properties of the lagrangian of the SM is that the theory is invariant under the Poincaré transformation in real space, and invariant under the $SU(3)_c \times SU(2)_L \times U(1)_Y$ transformation in internal space. The fact that the lagrangian has a certain symmetry is an important guiding principle in constructing the theory. Therefore, many theories of the Beyond standard Model (BSM) are often described as extensions of symmetry.

2.2 Supersymmetry

This section explains Supersymmetry theory (SUSY), which is one of the promising BSMs. The Coleman-Mandula theorem denotes that a symmetry for S-matrix should be a direct product of the Poincaré group and an internal group. However, the theorem is limited within transformations defined by commutation relation. The Haag-Lopuszanski-Sohnius theorem extends the Poincaré transformation by considering transformations involving an anti-commutation relation. This extended Poincaré transformation is called the SUSY transformation, and the extended elements are defined as follows.

$$\{Q_\alpha, \bar{Q}_{\dot{\alpha}}\} = 2(\sigma^\mu)_{\alpha\dot{\alpha}}P_\mu \tag{2.2}$$

$$\{Q_\alpha, Q_\beta\} = \{\bar{Q}_{\dot{\alpha}}, \bar{Q}_{\dot{\beta}}\} = 0 \tag{2.3}$$

$$[P^\mu, Q_\alpha] = [P^\mu, \bar{Q}_{\dot{\alpha}}] = 0 \tag{2.4}$$

Q_α is the generator of the SUSY transformation, and $\alpha, \dot{\alpha}$ is the spinor index, 1 or 2.Also, μ is the index of the real space, and σ^μ is the Puli matrix.

SUSY can be considered as an extension of the real space, which is called super space and uses $(x_\mu, \theta_\alpha, \bar{\theta}_{\dot{\alpha}})$ as the coordinate system. The θ_α and $\bar{\theta}_{\dot{\alpha}}$ are the extended coordinates of weyl spinor, which are anti-commute with each other. Also, a field of a particle in super space is called super field. Chiral and vector super fields are introduced as irreducible representations for the global SUSY transformation. The chiral super field consists of filed with spin 0 and 1/2 and an auxiliary filed. The vector super field consists of filed with spin 1/2 and 1 and the auxiliary filed. It is noteworthy that fields with different spins are treated in a single expression. It implies that there is a super partner particle (SUSY particle), whose spin is different by 1/2, for every particle. Also, according to 2.4, the SUSY transformation and P^μ are exchangeable. It means that the mass of the SM particle and its SUSY particle are equal. Fig.2.2 shows the particles introduced in the Minimal Supersymmetric Standard Model (MSSM), which is the minimal model of SUSY. The details of MSSM are described in section 2.2.5.

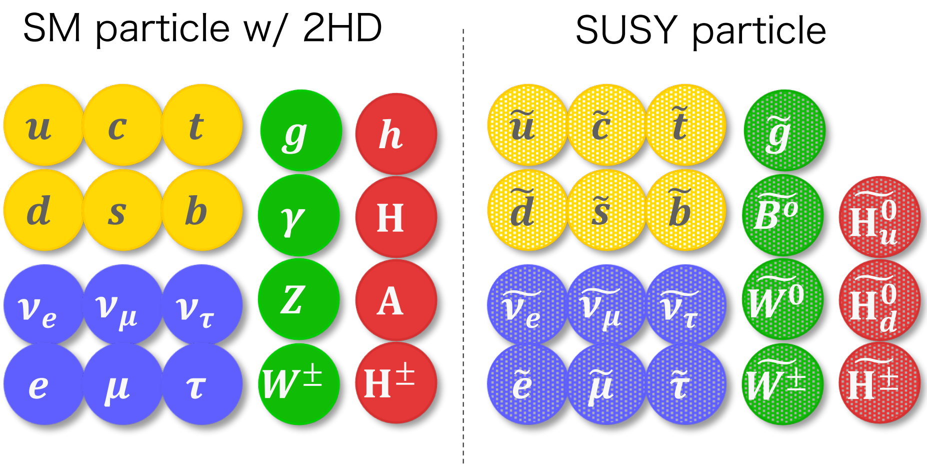

Figure2.2 MSSM particles

Newly introduced SUSY particles for fermion are called sup, stop, smuon, and so on. "s-" is added to the name of SM fermions. Also, newly introduced SUSY particles for the gauge particles and higgs are called gluino, higgsino, and so on. "-ino" is added to the name of SM gauge particles and higgs. In SUSY, the Yukawa coupling is described in the super potential, consisting of the chiral superfields, and the chirality must be the same as all in the potential. Therefore, SM higgs cannot give mass to all the fermions. Therefore, the 2 Higgs Doublet Model (2HDM) is naturally introduced in SUSY, and H_u and H_d of the two-dimensional representation of $SU(2)_L$ give masses for up-type and down-type fermions, respectively.

2.2.1 SUSY soft breaking

As shown in Fig. 2.2, SUSY requires particles more than twice as many SM particles, but half of them have not currently been found yet. Therefore, it is assumed that SUSY is broken in our universe. However, it is known that the supersymmetrized Lagrangian of the SM cannot be successfully explained by a broken SUSY. On the other hand, it is obvious that the Lagrangian of the SM is incomplete (for example, it does not include the gravitational interaction). Therefore, we consider a scenario in which SUSY breaking occurs in the "hidden sector," which we don't yet know, and the effect appears in the "visible sector," which we know. In this case, the effects that appear in the visible sector are shown below[6].

$$\mathcal{L}^{MSSM} = \mathcal{L}^{MSSM}_{SUSY} + \mathcal{L}^{MSSM}_{soft} \tag{2.5}$$

$$\begin{aligned}\mathcal{L}^{MSSM}_{soft} =& -\frac{1}{2}(M_3\tilde{g}\tilde{g} + M_2\tilde{W}\tilde{W} + M_1\tilde{B}\tilde{B} + c.c.)\\ &- \tilde{Q}^{\dagger}\mathbf{m_Q}^2\tilde{Q} - \tilde{L}^{\dagger}\mathbf{m_L}^2\tilde{L} - \tilde{\bar{u}}\mathbf{m_{\bar{u}}}^2\tilde{\bar{u}}^{\dagger} - \tilde{\bar{d}}\mathbf{m_{\bar{d}}}^2\tilde{\bar{d}}^{\dagger} - \tilde{\bar{e}}\mathbf{m_{\bar{e}}}^2\tilde{\bar{e}}^{\dagger}\\ &- (\tilde{\bar{u}}\mathbf{a_u}\tilde{Q}H_u - \tilde{\bar{d}}\mathbf{a_d}\tilde{Q}H_d - \tilde{\bar{e}}\mathbf{a_e}\tilde{Q}H_d + c.c.)\\ &- m^2_{H_u}H^*_uH_u + -m^2_{H_d}H^*_dH_d - (bH_uH_d + c.c.)\end{aligned} \tag{2.6}$$

Here, $\mathcal{L}^{MSSM}_{SUSY}$ represents the Lagrangian obtained by supersymmetrization of SM, and $\mathcal{L}^{MSSM}_{soft}$ is the SUSY soft breaking term introduced explicitly. Soft breaking means the term of SUSY breaking that does not affect the solution of the hierarchy problem described in section 2.3.2. $\mathcal{L}^{MSSM}_{soft}$ is eq.(2.6). M_3, M_2, M_1 are the mass parameters of gluino, wino, and bino, respectively, and $\mathbf{m_Q}, \mathbf{m_L}, \mathbf{m_{\bar{u}}}, \mathbf{m_{\bar{u}}}, \mathbf{m_{\bar{d}}}$ and $\mathbf{m_{\bar{e}}}$ are mass matrices of squarks and sleptons. The $\mathbf{a_u}, \mathbf{a_d}, \mathbf{a_e}$ are the matrix of couplings in $(scalar)^3$. The last line in eq.(2.6) is a term related to the higgs potential.

2.2.2 Electroweakino

In this section, neutralino,which is the target of this paper, is describe and summarize various scenarios about neutralino.

Mass eigenstates

SUSY partners for 2Higgs doublet and gauge boson for electroweak interaction are called Higgsino, Wino, and Bino, respectively, and they are collectively called Electroweakino. The same charged components of Bino, Wino, and Higgsino are mixed. when the gauge-eigenstate of the neutral component is written as $\psi^0 = (\tilde{B}, \tilde{W}^0, \tilde{H}_d^0, \tilde{H}_u^0)$, the mixsing matrix ($\mathbf{M}_{\tilde{N}}$) is written as follows.

$$\mathbf{M}_{\tilde{N}} = \begin{pmatrix} M_1 & 0 & -g'v_d/\sqrt{2} & g'v_u/\sqrt{2} \\ 0 & M_2 & gv_d/\sqrt{2} & -gv_u/\sqrt{2} \\ -g'v_d/\sqrt{2} & gv_d/\sqrt{2} & 0 & -\mu \\ g'v_u/\sqrt{2} & -gv_u/\sqrt{2} & -\mu & 0 \end{pmatrix} \tag{2.7}$$

Here, M_1 and M_2 are mass parameters for Bino and Wino derived from susy soft breaking (see section 2.2.1), respectively. The μ is the mass parameter of Higgs, and v_u and v_d are the VEVs of H_u and H_d, respectively. Also, g and g' are the gauge coupling constants of $SU(2)_L$ and $U(1)_Y$, respectively. The off-diagonal term of the mixing matrix can be written down since the terms are originated from the gaugeino-higgsino-higgs coupling with VEV of higgs.

In the same way, when the gauge-eigenstate of the charged component is written as $\psi^{\pm} = (\tilde{W}^+, \tilde{H}_u^+, \tilde{W}^-, \tilde{H}_d^-)$, the mixsing matrix ($\mathbf{M}_{\tilde{C}}$) can be written as follows.

$$\mathbf{M}_{\tilde{C}} = \begin{pmatrix} 0 & 0 & M_2 & gv_d \\ 0 & 0 & gv_u & \mu \\ M_2 & gv_u & 0 & 0 \\ gv_d & \mu & 0 & 0 \end{pmatrix} \tag{2.8}$$

The results of calculating the each mass eigenstates from eq.2.7 and eq.2.8 are shown below.

$$m_{\tilde{N}_1} = M_1 - \frac{m_Z^2 s_W^2 (M_1 + \mu \sin 2\beta)}{\mu^2 - M_1^2} + ... \tag{2.9}$$

$$m_{\tilde{N}_2} = M_2 - \frac{m_W^2 (M_2 + \mu \sin 2\beta)}{\mu^2 - M_2^2} + ... \tag{2.10}$$

$$m_{\tilde{N}_3} = |\mu| - \frac{m_Z^2 (I - \sin 2\beta)(\mu + M_1 c_W^2 + M_2 s_W^2)}{2(\mu + M_1)(\mu + M_2)} + ... \tag{2.11}$$

$$m_{\tilde{N}_4} = |\mu| - \frac{m_Z^2 (I + \sin 2\beta)(\mu - M_1 c_W^2 - M_2 s_W^2)}{2(\mu - M_1)(\mu - M_2)} + ... \tag{2.12}$$

$$m_{\tilde{C}_1} = M_2 - \frac{m_W^2 (M_2 + \mu \sin 2\beta)}{\mu^2 - M_2^2} + ... \tag{2.13}$$

$$m_{\tilde{C}_2} = |\mu| - \frac{I m_W^2 (\mu + M_2 \sin 2\beta)}{\mu^2 - M_2^2} + ... \tag{2.14}$$

To calculate the mass eigenstates, the equation of VEV of higgs(v), $v^2 = v_u^2 + v_d = 2m_Z^2/(g^2 + g'^2)$, is used. Here, $\tan\beta$ is the ratio of the VEVs of 2HD and is defined by $\tan\beta = v_u/v_d$. Also, s_W,c_W represent the weinberg angle.

Particles in the mass eigenstates of the neutral and charged components are called neutralino and chargino, respectively. As for the neutralino, $m_{\tilde{N}_1}$ is called "Bino like" because the main component of $m_{\tilde{N}_1}$ is Bino. Similarly, $m_{\tilde{N}_2}$ is called "Wino like", $m_{\tilde{N}_3}$ and $m_{\tilde{N}_4}$ are called "Higgsino like". As for the chargeino, $m_{\tilde{C}_1}$ is called "Wino like" and $m_{\tilde{C}_2}$ is called "Higgsino like". Each masses depend on the unknown parameter $M_1, M_2, \mu, \tan\beta$. Therefore, it is not sure which one is the smallest. For convenience, the neutralino is written as $\tilde{\chi}_1^0, \tilde{\chi}_2^0, \tilde{\chi}_3^0, \tilde{\chi}_4^0$, starting with the lightest mass. The chargino is also described as $\tilde{\chi}_1^\pm, \tilde{\chi}_2^\pm$ in order from lightest to lightest.

Neutralino LSP scenarios

The neutralino is a candidate for the lightest supersymmetric particle (LSP), and various scenarios are possible depending on which of the four neutralinos is the lightest. In this thesis, the target is the Higgsino like LSP scenario, which means Higgsino is the main component of LSP. In other words, the target scenario has $|\mu| << M_1, M_2$. In this case, the mass spectrum of neutralino and chargino is typically $m(\chi_1^\pm) = \frac{1}{2}(m(\chi_1^0) + m(\chi_2^0))$.

2.2.3 Naturalness

Naturalness gives us an important guideline about the relation between mass parameters and Z boson mass in MSSM (discussed in section 2.2.5) [14].

$$-\frac{m_Z^2}{2} = |\mu|^2 + m_{H_u}^2 \tag{2.15}$$

m_Z is the mass of the Z boson, and its value is 91 GeV. The m_{H_u} is the mass parameter of Higgs, which gives the mass to the up-type fermions in 2HDM. The value is affected by the radiation correction of the stop and the gluino loop. Since the left term of eq.2.15 is the electroweak scale, it is natural that the right term is also the electroweak scale. On the other hand, since the mass of stop and gluino is rejected up to a few TeV[**?**], m_{H_u} is expected to be large. However, considering the value of *tanβ* and other factors, the stop and gluino masses can be larger than a few TeV with a reasonable level of fine-tuning of 1% [15]. In this case, $|\mu| < 700 GeV$ is required. Therefore, the Higgsino like LSP scenario is very motivative for the naturalness.

2.2.4 R-parity

The SUSY transformation introduced by eq.(2.2) and eq.(2.3) satisfies a kind of U(1) chiral symmetry as follows.

$$Q \to Q' = e^{i\lambda\gamma_5}\begin{pmatrix}Q_\alpha \\ Q_{\dot{\alpha}}\end{pmatrix} \tag{2.16}$$

As well as with this transformation, the following symmetry for the coordinate system of super space is considered.

$$\begin{pmatrix}\theta_\alpha \\ \bar{\theta}_{\dot{\alpha}}\end{pmatrix} \to e^{i\lambda\gamma_5}\begin{pmatrix}\theta_\alpha \\ \bar{\theta}_{\dot{\alpha}}\end{pmatrix} \tag{2.17}$$

The symmetry of eq.(2.17) is called R-symmetry. The R-symmetry must obviously be broken since it prohibits the Majorana mass (the gaugeino mass). However, when $\lambda = \pi$, it does not prohibit the Majorana mass. Therefore, R-parity can be conserved. The eigenvalues of R-parity are -1 for SUSY particles and +1 for SM particles. It can be formulated as follows.

$$R = (-1)^{2s}(-1)^{3B+L} \tag{2.18}$$

SUSY generally predicts interactions that have not yet been observed experimentally, such as interaction with violation of the Lepton and Baryon numbers (e.g. proton decay). It is preferable to assume that the R-parity is conserved since the conservation prohibits such interactions. Additionally, assuming the conservation of R-parity, it is able to explain what Dark Matter is, which will be discussed later in section2.3.3. Therefore, this paper targets the SUSY model in which R-parity is conserved.

2.2.5 Minimal Supersymmetric Standard Model

This section discusses the Minimal Supersymmetric Standard Model (MSSM) and Phenomenological MSSM (pMSSM). MSSM refers to the minimal SUSY model, which satisfies the following conditions.

- minimal gauge group ($SU(3)_c \times SU(2)_L \times U(1)_Y$)
- minimal particle content
- R parity conservation
- soft SUSY breaking

This section discusses the Minimal Supersymmetric Standard Model (MSSM) and Phenomenological MSSM (pMSSM). MSSM refers to the minimal SUSY model, which satisfies the fol-

lowing conditions. When the above conditions are satisfied, the number of parameters that must be measured in experiments that don't appear in SM is 105. MSSM has many parameters, but the number can be reduced from 105 to 19 by adding some conditions based on the current experimental results. The MSSM model with the newly added conditions is called pMSSM. The following list shows the newly added conditions.

- No new source of CP-violation
- No flavor changing nuetoral current
- First and second generation universality

The remaining parameters after requesting the above conditions are summarized in Table2.2.5.

Table2.1 Description of the pMSSM parameter

parameter	description
$\tan\beta$	the ratio of the vacuum expectation values of the two Higgs doublets
M_A	the mass of the pseudoscalar Higgs boson
μ	the higgsino mass parameter
M_1	the bino mass parameter
M_2	the wino mass parameter
M_3	the gluino mass parameter
$m_{\tilde{q}L}$	the first and second generation squark masses
$m_{\tilde{u}R}$	
$m_{\tilde{d}R}$	
$m_{\tilde{l}L}$	the first and second generation slepton masses
$m_{\tilde{l}R}$	
$m_{\tilde{Q}L}$	the third generation squark masses
$m_{\tilde{t}R}$	
$m_{\tilde{b}R}$	
$m_{\tilde{\tau}L}$	the third generation slepton masses
$m_{\tilde{\tau}R}$	
A_t	the third generation trilinear couplings
A_b	
A_τ	

2.3 Motivation of SUSY

This section summarizes the four motivations of SUSY.

2.3.1 Grand unification theory

The first is the unification of the gauge coupling constants. The SM has coupling constants $\alpha_3, \alpha_2, \alpha_1$ corresponding to $SU(3)_c, SU(2)_L, U(1)_Y$ respectively. Since these values cannot be predicted from the theory, it needs to measure them experimentally. The Grand Unification Theory (GUT) is a theory that can combine these parameters into one.

The well-known GUT has the structure of $SU(5)$. Since $SU(5)$ contains $SU(3)_c, SU(2)_L, U(1)_Y$ as subgroups, the three coupling constants can be computed with α_G. Since the present universe is cold and low energy, α_G looks like to separated into $\alpha_3, \alpha_2, \alpha_1$ according to the renormalization group equation (eq.(2.20))[6].

$$\frac{d}{dt}\alpha_i^{-1} = -\frac{b_i}{2\pi} \quad (i = 1, 2, 3) \tag{2.19}$$

$$(b_1, b_2, b_3) = \begin{cases} (41/10, -19/6, 7) & \text{SM} \\ (33/5, 1, -3) & \text{MSSM} \end{cases} \tag{2.20}$$

b_i is a value determined by the structure of groups, the number of particles, and their quantum numbers. Therefore, differences appear between SM and MSSM. Fig.2.3 shows the energy scale dependence of gauge coupling. The dotted line is extrapolated coupling constants according to the renormalization group equation with SM. the coupling constants are not unified even at the GUT scale (10^{15} GeV). On the other hand, in MSSM (blue and red lines in Fig.2.3), the gauge coupling is unified at the GUT scale. This result strongly suggests that SUSY particles exist at the TeV scale.

2.3.2 Hierarchy problem

The fundamental scale of elementary particles is the GUT scale (10^{15} GeV) or Planck scale (10^{19} GeV), which can include quantum gravity. On the other hand, the masses of W boson and Higgs are on the Electroweak scale (10^2 GeV). There is a large deviation between Higgs mass and fundamental scale.The hierarchy problem is how to solve such unnatural differences from the fundamental scale. According to 't Hooft, "at any energy scale μ, a physical parameter α_μ is allowed to be very small only if the replacement $\alpha_\mu = 0$ would increase the symmetry of the system.". For example, chiral symmetry and gauge symmetry ensure the light mass for

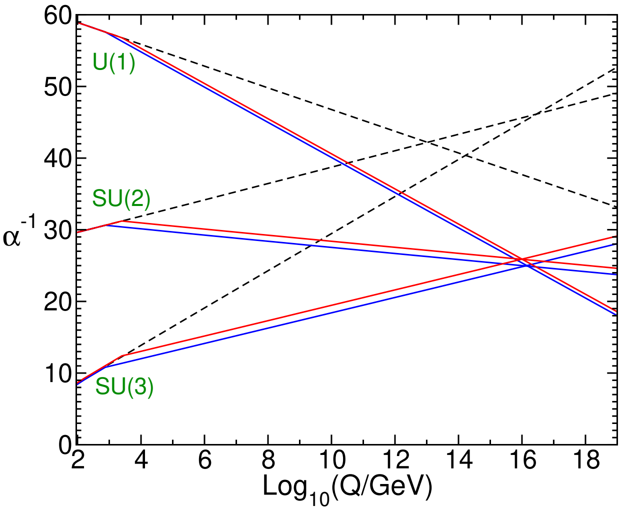

Figure2.3 The blue and red lines assume that the SUSY particle appears at 750 GeV and 2.5 TeV, respectively. Under both assumptions, the couplings are unified in the GUT scale.[6]

fermion for gauge particles, respectively. However, there is no such symmetry for Higgs, and thus the hierarchy problem cannot be explained. In fact, when the bare mass of Higgs and the experimentally observed Higgs mass are m_{h_0} and m_h, respectively, the difference between them is written by the following equation.

$$m_h^2 - m_{h_0}^2 = \Delta m_h^2 = -\frac{3|\lambda|}{8\pi^2}\Lambda^2 + ... \tag{2.21}$$

Here, Λ is the cutoff scale, and λ is the coupling constant of interaction between higgs and particles. The first term in eq.(2.21) is the radiative correction effect of one loop (Fig.2.4), which affects as the quadratic radiative corrections with respect to the cutoff scale Λ. Especially for top, which has the strongest coupling with higgs, λ is $O(1)$, and Λ is 10^15 GeV (GUT scale). As a result, the effect of the quadratic radiative is as much as 10^{30} GeV. Since $m_h = 125$ GeV is obtained from the experiment result, a large discrepancy about $m_h^2/\Lambda^2 = 10^{-26}$ cannot be avoided. This means that there is unnatural fine-tuning between the m_{h_0} and radiation correction terms.

SUSY can solve this problem by indirectly introducing a symmetry that ensures the light higgs mass. As mentioned above, in SUSY theory, higgs with spin 0 and higgsino with spin 1/2 are included in the same representation. Therefore, if SUSY is not broken, the masses of higgs and higgsino must be equal. Since higgsino mass is ensured light by chiral symmetry, it is indirectly suggested that the higgs mass is also light. In fact, by taking into account the radiation correction term from SUSY particles, eq.(2.21) can be rewritten as follows.

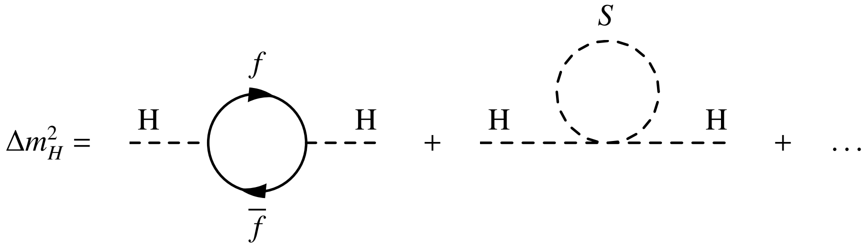

Figure2.4 The diagrams for one-loop quantum corrections to the Higgs squared mass parameter m_H^2, due to a Dirac fermion f (left), and a scalar S (right).

$$\Delta m_h^2 = -\frac{3|\lambda|}{8\pi^2}\Lambda^2 + \frac{3|\lambda|}{8\pi^2}\Lambda^2 + O(\log \Lambda) \tag{2.22}$$

The new term is the contribution of one loop of SUSY, and the term of the quadratic radiative is canceled completely. In other words, SUSY solves the Hierarchy problem. Another critical point is that the quadratic radiative term does not depend on the mass of the particles in the loop. Therefore, the quadratic divergence term is completely canceled even if SUSY is broken.

2.3.3 Dark matter

By observing the motions of galaxies in the Coma Cluster, it was claimed that the cluster contains more than 100 times the mass of stars in optically observable galaxies[16]. Furthermore, by measuring the rotational velocity of spiral galaxies, it was observed that the velocities of the stars and hydrogen gas belonging to the galaxy don't change with increasing distance from the galactic center [17]. In general, one would expect the rotational velocity v to decrease in proportion to $1/\sqrt{r}$ outside the central region of the galaxy, but as shown in Figure 2.5, the observation of M33 galaxy shows a constant velocity distribution. This indicates the existence of optically unobservable masses beyond a few kpc from the galactic center.

Dark matter (DM) is a particle which a candidate for the identity of the unobservable masses, and it should be stable, neutral, cold, and abundant.

Neutrino satisfies most of the requirements for the DM, but neutrino is not Cold (not in relativistic motion) because of its low mass. Therefore, DM is not SM particle. The LSP with R-parity conservation satisfies the requirements of DM. In the scenario with R-parity conservation, as shown in Fig.2.6, the SUSY particle must decay to another lighter SUSY particle, and decaying to SM particle only is prohibited. Therefore, the LSP is stable and can be a dark matter.

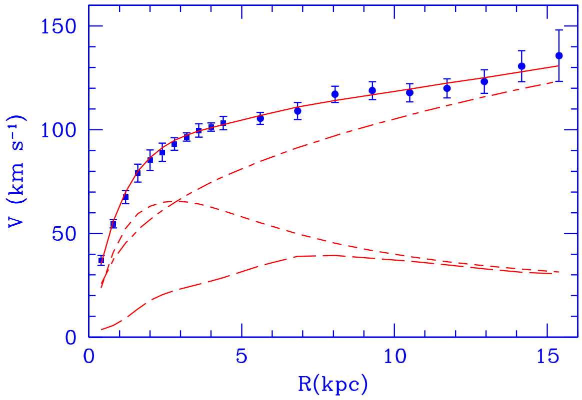

Figure2.5 The M33 galaxy rotational curve [18]. The x-axis is the distance from the center of the galaxy to the orbiting object and y-axis is the rotational velocity. The filled circles are the measured data points. The solid line is the best fit model considered on the halo contribution (dashed line), stellar disk contribution (short dashed line) and gas contribution (long dashed line).

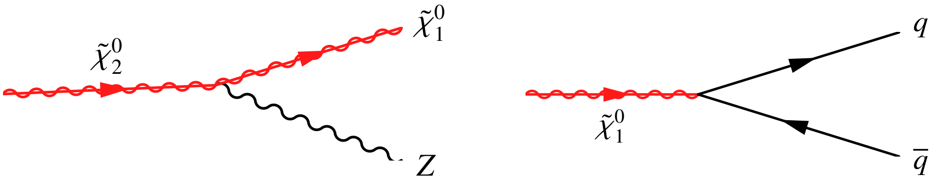

(a) Allowed SUSY particle decay

(b) Prohibited dark matter decay

Figure2.6 R parity conservation

When SUSY is DM, the main contribution of the spin-independent crosssection between proton and DM (σ_p^{SI}) is scattering via Higgs particle, and the coupling is described as the following equation[19].

$$c_{h\tilde{\chi}_1^0\tilde{\chi}_1^0} \simeq -\frac{1}{2}(1+\sin 2\beta)\left(\tan^2\theta_w \frac{M_w}{M_1-\mu} + \frac{M_w}{M_2-\mu}\right) \tag{2.23}$$

Here, $\mu > 0$ is assumed. From eq.2.23, coupling is large when $\mu \simeq M_1$ or $\mu \simeq M_2$. Since

$\Delta m(\tilde{\chi}_1^0, \tilde{\chi}_2^0)$ is large when μ is close to M_1 or M_2, large Δm is excluded by the DM direct ditection experiment, such as the Xenon1T experimen[20]. The results of the Xenon1T experiment, which currently reports the strictest lower limit for σ_p^{SI}, suggest $\Delta m(\tilde{\chi}_1^0, \tilde{\chi}_2^0) < O(10\text{GeV})$.

2.3.4 Muon g-2

In 2021, Felmi lab reported a new measurement of muon anomalous magnetic moment (Fig.2.7). Here, the muon magnetic moment is refferd to as g_μ ,and define a_μ as $(g_\mu - 2)/2$. the predicted value of a_μ in the SM is a_μ^{SM} =116 591 810(43)×10^{-11}. (Values in parentheses are error). On the other hand, the Muon g-2 group of Felmilab (FNAL) reported a_μ^{SM} =116 592 040(54)×10^{-11}. Also, by combining the result with the Brookhaven National Laboratory (BNL) result[21], the deviation with SM is 4.2σ. This result may be a sign of new physics.

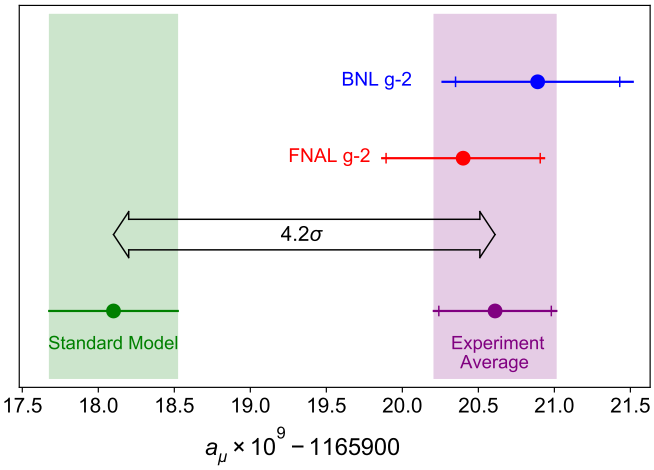

Figure2.7 From top to bottom: experimental values of a_μ from BNL E821[21], FNAL measurement[7], and the combined average. The inner tick marks indicate the statistical contribution to the total uncertainties. The Muon g − 2 Theory Initiative recommended[22] value for the standard model is also shown.

The loop of the Feynman diagram in Fig. 2.8 contributes to the muon magnetic moment. The magnitude of the contribution is sensitive to the value of μ, M_1, M_2. The details are discussed in Ref.[23, 24, 25]. Typically, $\tilde{\chi}_1^0$ and $\tilde{\chi}_1^\pm$ must be light in order to generate a 4.2σ deviation , and the result of scanning the pMSSM parameters [26][27] claim $m(\tilde{\chi}_1^0) < 500$ GeV as a typical value.

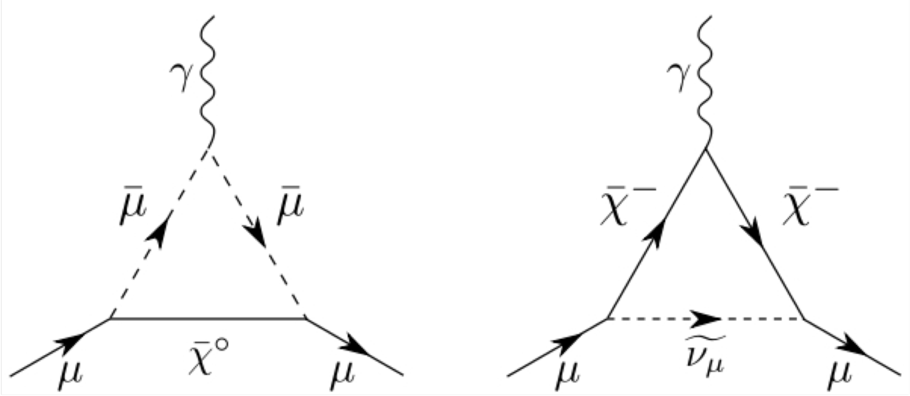

Figure2.8 contribution of SUSY particle on muon magnetic moment.

2.4 Target scenario

In the region of $\Delta m(\tilde{\chi}_1^0, \tilde{\chi}_2^0) < 10\text{GeV}$, which is not excluded by the DM direct detection experiment, a large region is excluded by some analysis with the Large Electron-Positron Collider (LEP) and analysis in the LHC-ATLAS experiments. The LEP is a collider that finished the operation in 2000. By combining the results of experiments on the LEP, the region in which $m(\tilde{\chi}_1^{\pm})$ is less than 92.4 GeV are excluded [8]. The LHC-ATLAS experiment is proton-proton collision experiment. In the experiment, the disappearing track search[28] exclude the region where $\Delta m(\tilde{\chi}_1^0, \tilde{\chi}_2^0)$ ($\Delta m(\tilde{\chi}_1^0, \tilde{\chi}_0^{\pm})$) is less than 0.4(0.8) GeV. Also, The region where $\Delta m(\tilde{\chi}_1^0, \tilde{\chi}_2^0)$ is more than a few GeV is exclude by the di-lepton search [9].

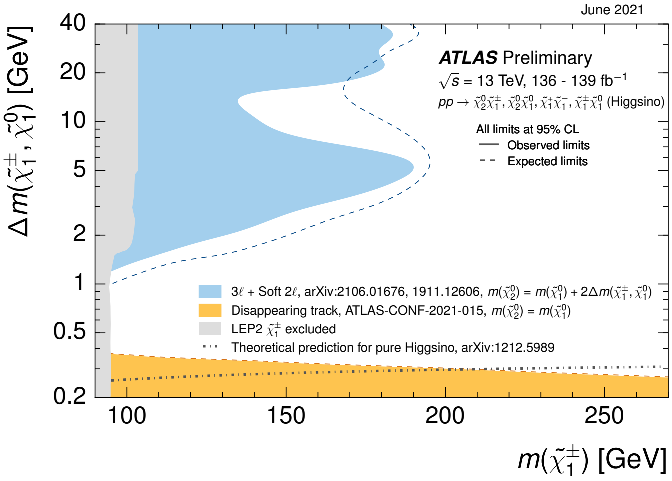

Figure2.9 Exclusion limits at 95 % CL for higgsino pair production as a function of the $\Delta m(\tilde{\chi}_1^{\pm}, \tilde{\chi}_1^0)$ and $\tilde{\chi}_1^0$ mass.

The target of this thesis is to explore the region where $\Delta m(\tilde{\chi}_1^0, \tilde{\chi}_2^0)$ is 1 GeV to 5 GeV, which has not been explored since LEP, by using a channel in which $\tilde{\chi}_2^0$ decays into $\tilde{\chi}_1^0$ and two muons.

3. LHC-ATLAS experiment

3.1 Large Hadron Collider

The Large Hadron Collider (LHC)[29], located near the Swiss-French border, is the world's largest hadron collider and is used to verify the Standard Model and study physics beyond the Standard Model. The LHC had been designed to be center of mass energy of 14 TeV and a peak luminosity of $10^{34}\mathrm{cm}^{-2}\mathrm{s}^{-1}$. The LHC operation in Run-2 has proceeded very well. It achieved the center of mass energy of 13 TeV and a peak luminosity of $2.14^{34}\mathrm{cm}^{-2}\mathrm{s}^{-1}$, which is more than double the design value.

The overview of the accelerator is shown in Fig.3.1. Four accelerators are provided to inject protons into LHC rings. First, Linear Accelerator 2 (Linac2) accelerates the protons to about 50 MeV of kinetic energy. Second, They are accelerated to 1.4 GeV in the Proton Synchrotron Booster (PSB). Third, They are accelerated to 25 GeV by the Proton Synchrotron (PS), and forth, proton energy reaches 450 GeV at the Super Proton Synchrotron (SPS).Finally, protons are injected into the LHC and accelerated to 6.5 TeV. In the LHC, 1232 superconducting dipole magnets are used to bend the direction of the protons in order to orbit them. Some of these dipole magnets provide magnetic fields of up to 8.33 T to control the high energy protons.

A proton beam is composed of a series of bunches, which contains about 10^{11} protons. The design value for the number of bunches per Large Hadron Collider (LHC) ring is 2808, and the interval between bunches is 25ns. Therefore, the detectors at the interaction point detect bunch crossing (BX) at 40 MHz. Figure 3.2 shows a histogram of the number of proton-proton collisions in a BX. In Run 2, an average of 34.2 proton-proton collisions occurred in one BX.

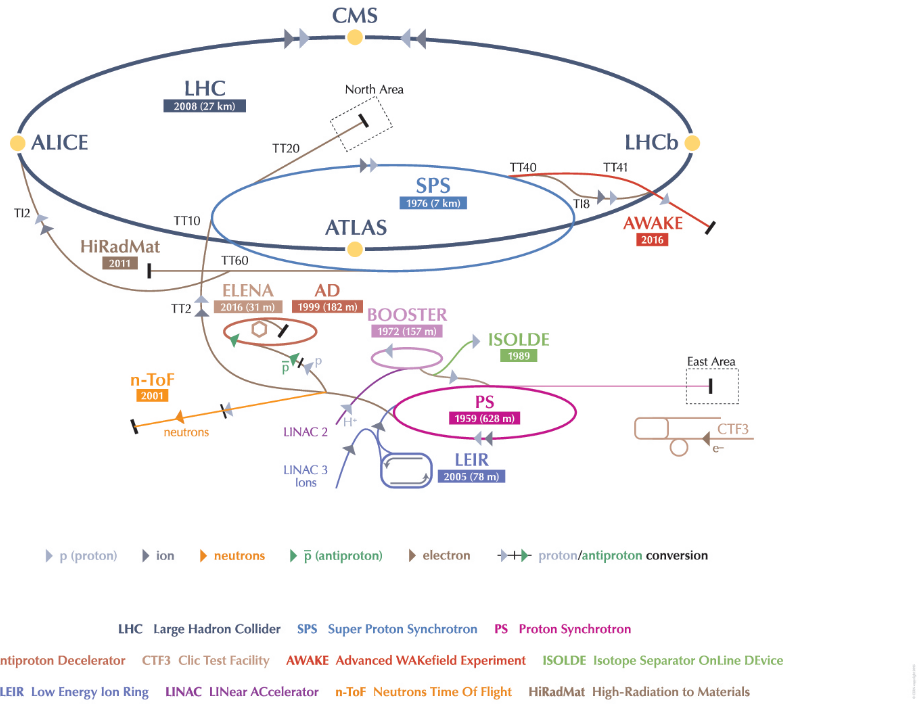

Figure3.1 Accelerator system at CERN[1]. The LINAC2, BOOSTER, PS, and the SPS are used as the injector to the LHC.

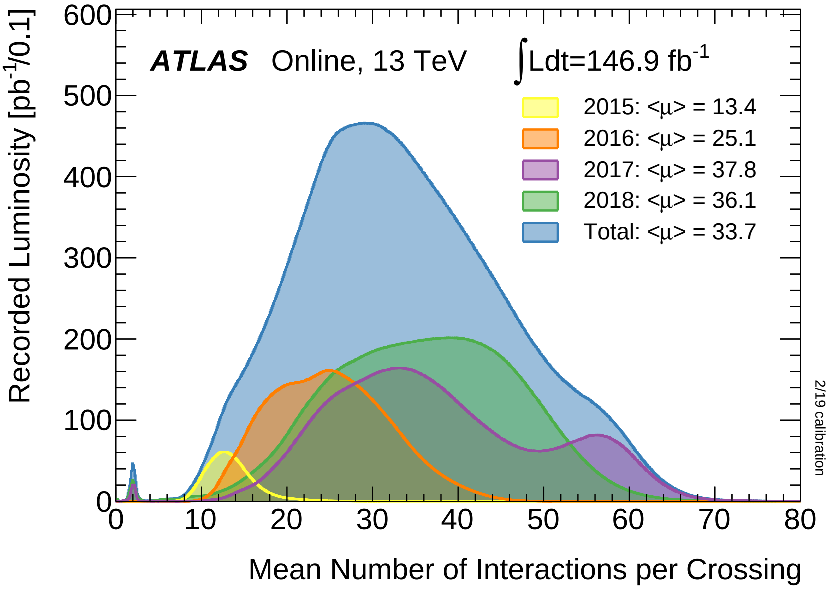

Figure3.2 Number of interactions per proton bunch crossing [1] . The yellow, orange, purple and green graphs are the distributions for 2015, 2016, 2017 and 2018, respectively. The distribution for the entire period of 2015–2018 are shown with blue graph, with 33.7 average number of interaction per proton bunch.

3.2 ATLAS Detector

The ATLAS (A Toroidal LHC ApparatuS) detector[2] is the largest, general-purpose particle detector at the Large Hadron Collider (LHC). It is a cylinder with a diameter of 25 meters, a longitudinal length of 44 meters, and a total weight of 7,000 tons. Fig.3.3 shows overview of the ATLAS detector. It is constructed with various sub-detectors, starting from the one closest to the interaction point, internal detector, calorimeter, and muon spectrometer. In addition to the detectors, there is a superconducting solenoid magnet between the internal detector and the calorimeter, and a toroid magnet outside the calorimeter. This section briefly describes each of the instruments and the magnet system.

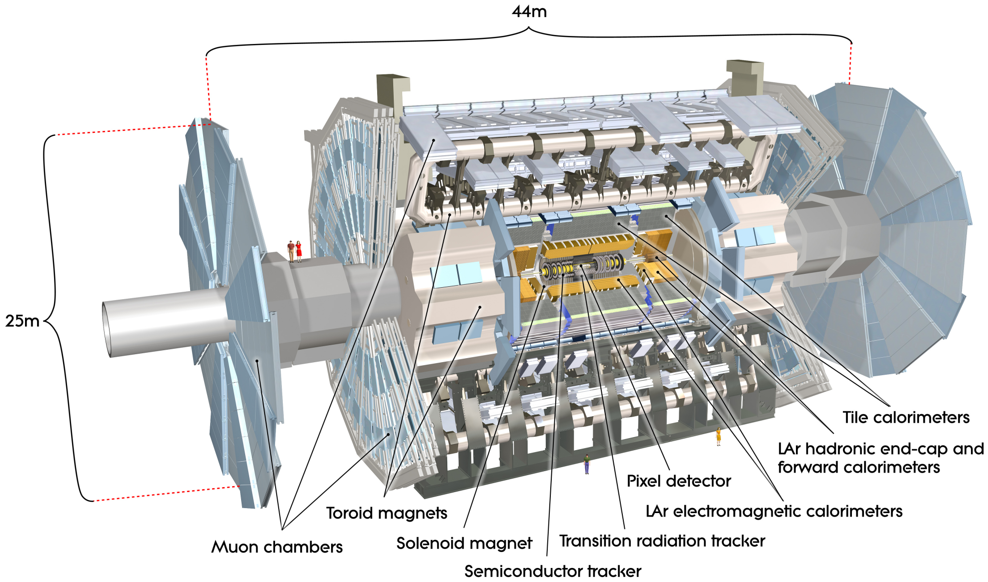

Figure3.3 Cut-away view of the ATLAS detector. The dimensions of the detector are 25 m in height and 44 m in length. The overall weight of the detector is approximately 7000 tonnes.[30]

Coordinate system in ATLAS

This section describes the coordinate system used in the ATLAS detector. Figure 3.4 shows the axes. The z-axis is the same as the beam pipe, which passes through the center of the ATLAS detector. The x-axis is defined to be perpendicular to the z-axis and pointing to the center of the LHC beam ring. Also, the y-axis is defined to be perpendicular to the z-axis and pointing to the zenith. Furthermore, radial direction is defined as $R = \sqrt{x^2 + y^2}$. the azimuthal angle in the x-y plane is defined as ϕ and the zenithal angle from the z-axis as θ. Also, pseudorapidity is often used in hadron collision type experiments such as the ATLAS experiment. It is defined as $\eta = -\ln\tan(\theta/2)$. The region of $|\eta| \leq 1.05$, which corresponds to the tube part of the cylinder, is called the barrel, and the region with $|\eta| > 1.05$ is called the end cap.

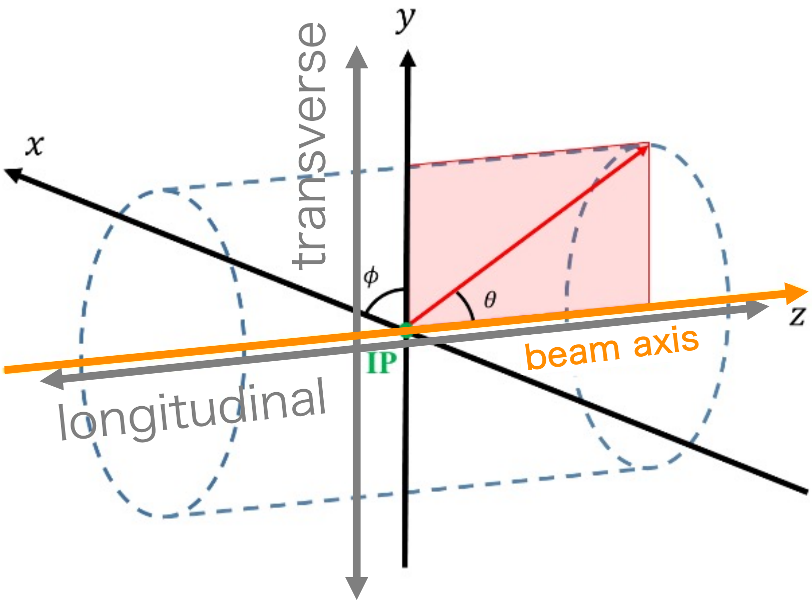

Figure3.4 The ATLAS coordinate system. The origin of the coordinates are the center of the interaction point, x-axis is taken to point to the center of the LHC ring, y-axis to point upwards, and z-axis along the beam pipe.Pseudo-rapidity $\eta = -\ \ln\tan(\theta/2)$ is often used instead of θ.

3.2.1 Magnet System

Magnetic fields are provided inside the ATLAS detector by three system (Fig.3.5): a solenoid magnet surrounding the collision point, a toroidal magnet in the barrel, a toroidal magnet in each end cap. The solenoid magnet provides a 2T magnetic field along the z-axis for the Inner Detector. Toroidal magnets、which are composed of eight-fold symmetrical coils, provide the magnetic field in the ϕ direction. In order to avoid multiple scattering, the inside of the magnet has an empty core. The barrel part provides a magnetic field of 0.5 T in the ϕ direction, and the end cap part also provides a magnetic field of 1 T in the ϕ direction.

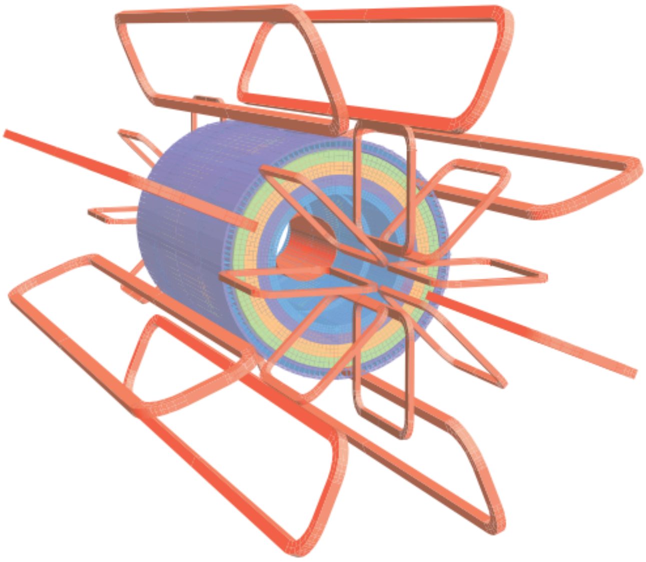

Figure3.5 Layout of the superconducting magnet system in the ATLAS detector[2]. The solenoid magnet is placed at the innermost part of the detector. The barrel and the end-cap toroidal magnets are placed at the outer part of the detector.

3.2.2 Inner Detectors

The Inner Detector (ID) is located in the innermost layer of the ATLAS detector and consists of three types of detectors from the inside: the Pixel detector (PIX), the Semiconductor tracker (SCT), and the Transition Radiation Tracker (TRT). Additionally, Insertable B-Layer (IBL)[31] was introduced between Run1 and Run2, at the innermost layer of the Pixel detectors. The overall image, except for IBL, is shown in Fig.3.6, and the hierarchical structure of the barrel section is shown in Figure 3.7. The purpose of these detectors is to precisely measure the trajectory of charged particles and determine the positions of interaction points with high accuracy from the reconstructed trajectories. There is a magnetic field of 2 T along the z-axis in the inner detector provided by the superconducting solenoid magnet. As a result, the charged particle is bent in the ϕ direction, and the transverse momentum can be measured by analyzing their trajectory.

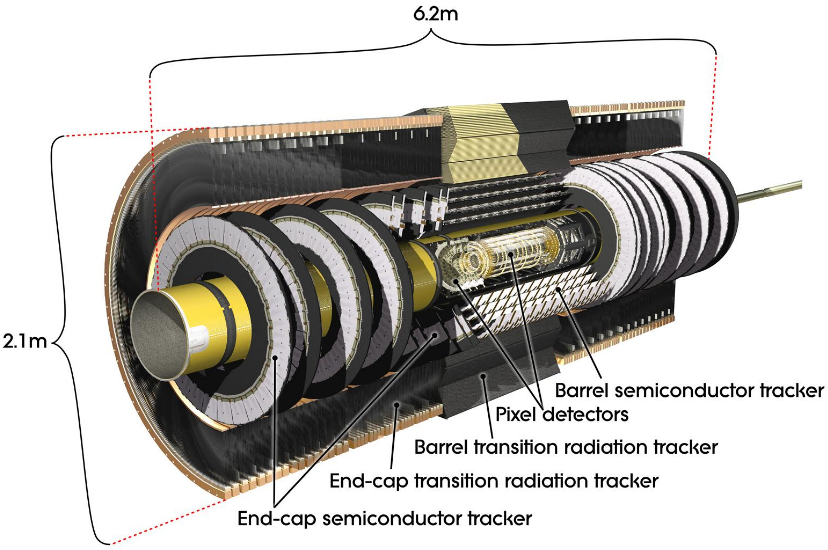

Figure3.6 A cut-away view of the inner detectors. The inner detectors consists of the Pixel detectors,the semiconductor trackers, and the transition radiation trackers.[32]

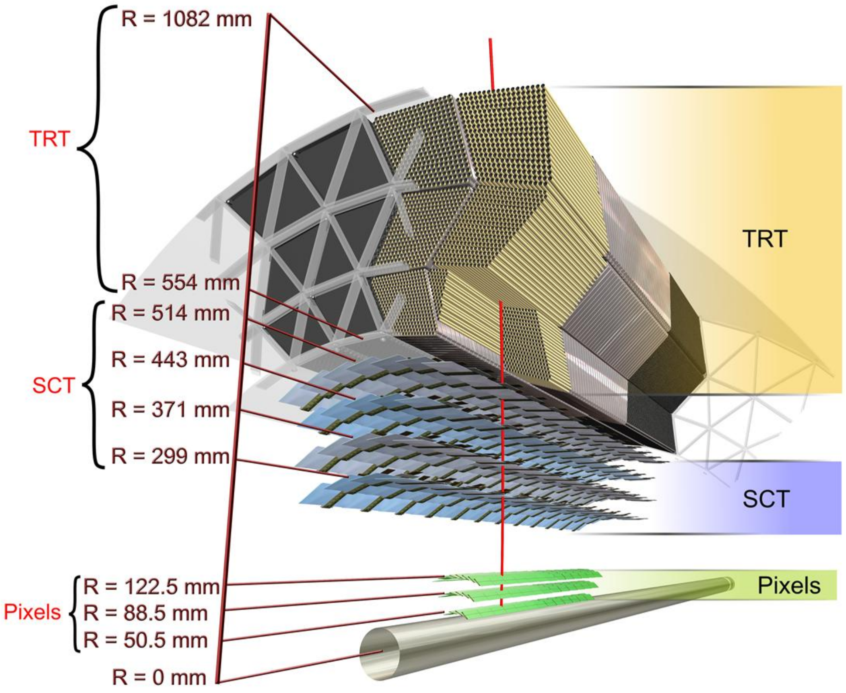

Figure3.7 the ATLAS Inner Detector in the barrel region.[32]

Pixel detector : PIX

PIX is located in the innermost layer of the ATLAS detector. It has a vital role in measuring precise position measurement of the interaction point. It covers the region of $|\eta| \leq 2.5$. The barrel section has detectors arranged in a coaxial cylindrical shape, and the end cap section has disc-shaped detectors arranged so that they are perpendicular to the z-axis. The total number of channels is 80.4 million with a pixel size of 50 μm × 400 μm and a position resolution of 10 μm in the $R - \phi$ plane and 115 μm in the z-axis direction. For IBL, channel size is 50 μm × 250 μm.

Semiconductor tracker : SCT

SCT is located outside of the pixel detector. It covers a region of $|\eta| \leq 2.5$, and like the pixel detector, the barrel has a coaxial cylindrical arrangement of detectors, while the end cap has disk-shaped detectors arranged perpendicular to the z-axis. A high positional resolution is required to measure the decay points of B-mesons and τ leptons. The strip size is 80 μm × 12.8 cm, and They can be measured in the z-axis direction by tilting the two layers by 40 mrad to each other. The positional resolution is 17 μm in the $R - \phi$ plane and 580 μm in the z-axis direction.

Transition Radiation Tracker : TRT

TRT is located outside the silicon detector and covers the region of $|\eta| \leq 2.0$. It is a detector with a multi-layer of 4 mm diameter drift straw tube with carbon fiber. The drift-straw tube detector is stacked 73 layers at the barrel and 160 layers at the end cap. The position resolution in the $R - \phi$ plane is 130 μm. However, the detector is placed parallel to the z-axis, so it cannot measure in the z-axis direction. It is also possible to identify particles using the principle of transition radiation. Polypropylene fibers are inserted between the drift-straw tube detectors as a transition radiation material, and photons are emitted when charged particles pass the material. This phenomenon is called transition radiation, and the energy spectrum of the emitted photon can be used to distinguish whether the passed particle is an electron or a hadron.

3.2.3 Calorimeters

The calorimeter is located outside the inner trackers. It is used to identify photons, electrons, and jets and to measure their energies and positions. The overall image is shown in Fig.3.8 The calorimeters can be divided into electromagnetic calorimeter and hadron calorimeter, and their structures are described below.

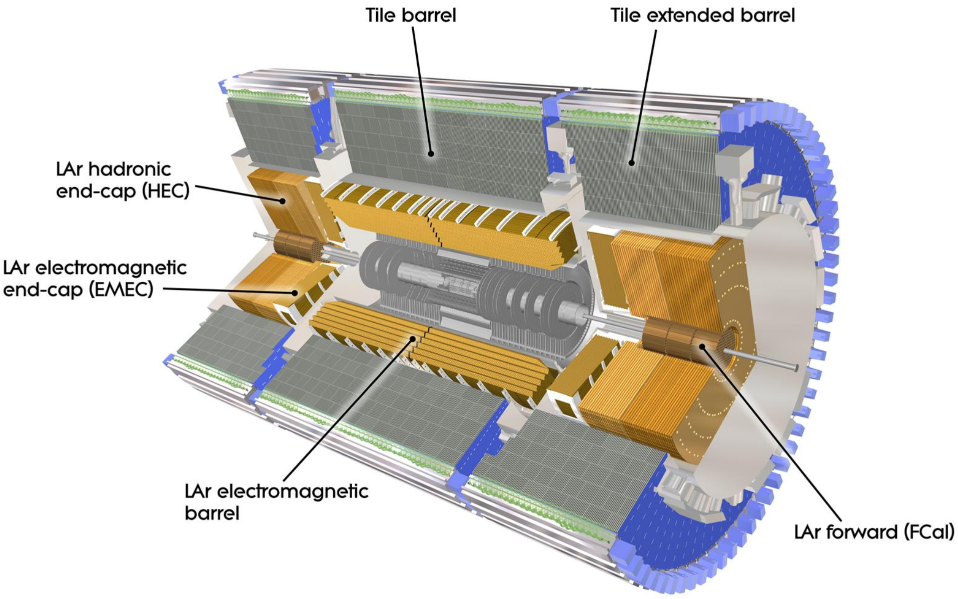

Figure3.8 The layout of the ATLAS calorimeter system[33]. The LAr electromagnetic calorimeters are installed inside the hadronic calorimeters. The electromagnetic calorimeters are subdivided into barrel and end-cap components. The hadronic calorimeters are subdivided into tile, end-cap, and forward.

Electromagnetic calorimeter

Electromagnetic calorimeter identifies electrons and photons and precisely measures their energies. The absorption layer is made of lead, and the detection layer is made of liquid argon (LAr).The detector is divided into a $|\eta| \leq 1.5$ barrel section and a $1.5 \leq |\eta| \leq 3.2$ end cap section. The accordion-like structure eliminates the insensitive region and reduces in-uniformities in the ϕ direction. The designed energy resolution is

$$\sigma E = 10\% \sqrt{E} \oplus 17\% E \oplus 0.7\% \tag{3.1}$$

for the measured energy of E [GeV].

Hadron calorimeter

Hadron calorimeter is used to reconstruct the jet and measure the jet's energy and direction, along with the electromagnetic calorimeter. In the barrel part($|\eta| \leq 1.6$), iron is used for the absorption layer, and a tiled scintillator is used for the detection layer. The endcap section($1.6 \leq$

| ≤ 3.2) contains a LAr Hadronic Endcap Calorimeter(HEC), which constrains liquid argon (LAr) as the detection layer and copper as the absorption layer. In the high radiation intensity region of $3.2 \leq |\eta| \leq 4.9$, a liquid argon forward calorimeter(FCal) are used for electrons, photons, and hadrons. For the detector, tungsten is installed in addition to copper as the absorption layer.

3.2.4 Muon spectrometers

The muon spectrometer (Fig.3.9), located at the outermost part of ATLAS, is a detector for measuring the momentum of muons from their trajectory. A muon is a charged lepton with a long lifetime of 2.2 μm In addition, because of their high penetrating power through matter, muons and neutrinos are the only particles that can reach the muon spectrometer from the interaction point. However, since neutrinos are not charged particles, most of them don't leave a signal. Therefore, the signal on the muon spectrometer is originated from muon.

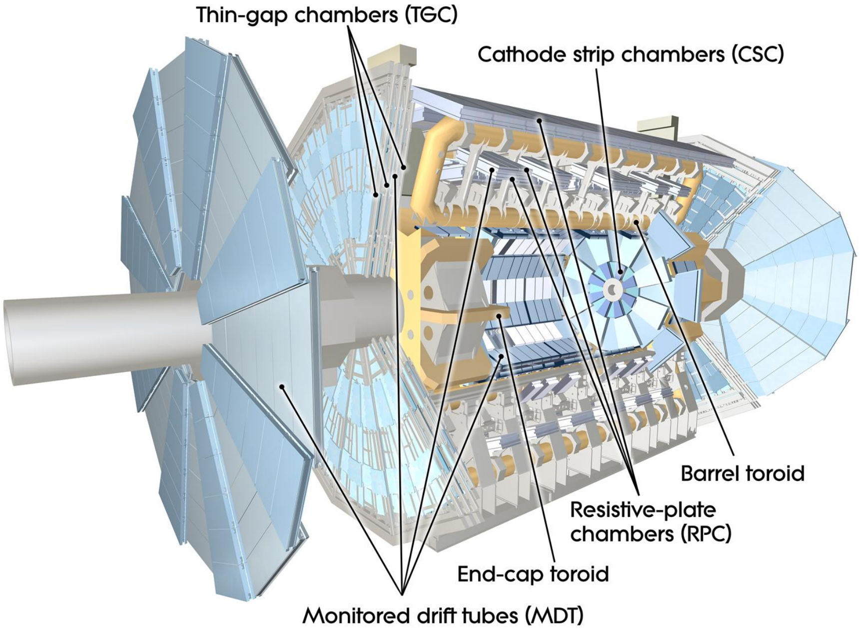

Figure3.9 The cut-away view of the muon spectrometer system[34], composed of four types of detectors, the Monitored Drift Tubes (MDT), the Cathode Strip Chambers (CSC), the Resistive Plate Chambers (RPC), and the Thin Gap Chambers (TGC).

Monitored Drift Tube : MDT

The MDT is a type of gas detector of a drift tube with a diameter of 30 mm and a wire diameter of 50 μm. It is filled with a three bar mixture of argon and carbon dioxide. A voltage of about 3080 V is applied between the anode and cathode. When a charged particle passes through the anode, the gas is ionized, and electrons drift to the anode wire. The position of the passing particle can be measured by the drift time. The position resolution of a single drift tube detector is about 80 μm and a resolution of 35 μm can be achieved. It is mainly used for precise measurements of Z coordinate in the barrel and R coordinate in the end cap.

Cathode Strip Chamber : CSC

As well as the MDT, this detector is designed to measure muon trajectory precisely. It is installed in the high radiation intensity region of $2.0 \leq |\eta| \leq 2.7$. The upper limit of the readout frequency for MDT is 150 $\mathrm{Hz/cm^2}$, but for CSC, it is 1000 $\mathrm{Hz/cm^2}$. The anode wires and the cathode strips are arranged orthogonally, allowing two-dimensional measurements. The wire spacing is 2.5 mm, and the strip spacing is 5.3 mm or 5.6 mm. The position resolution becomes 60 μm using induced charge on the strips.

Resistive Plate Chamber : RPC

The RPC is a gaseous parallel electrode-plate detector covering the barrel section of $|\eta| \leq 1.05$. It is mainly used for triggering. The RPC is a type of gas detector, and a mixture of $C_2H_2F_4$, $\mathrm{iso} - C_4H_{10}$, and SF_6 gas is sealed inside. A electric field of about 4.9 kV/mm is applied between the plates, and when a charged particle passes between them, the gas molecules are ionized. The electrons are attracted to the anode, causing an electron avalanche in the process. Strips are installed behind the plate at intervals of 30 mm. The electron avalanche induces a charge on the strips and readout it as a signal.

Thin Gap Chamber : TGC

The TGC is a type of MWPC (Multi Wire Proportional Chamber) covering $1.05 \leq |\eta| \leq 2.42$. It is mainly used as a trigger detector. The TGC is filled with a mixture of CO2 and n-pentane. The anode wire is installed so that it is parallel to the top and bottom of the trapezoidal-shaped TGC. The cathode surface is made of a glass epoxy plate. A copper strip divided TGC plane into 32 sections is installed on the backside of this cathode surface to intersect the anode wire.

3.3 Trigger and data acquisition systems

In the ATLAS experiment, a two-step triggering system consisting of a level 1 trigger and a high-level trigger is used. Figure 3.10 shows the trigger process. In this section, the two steps are briefly described.

Level-1 trigger

The level-1 trigger is done in hardware within 2.5 μs. Therefore, only the detectors with fast readout are used (calorimeter, TGC, and RPC). The level-1 trigger selects events with 100kH frequency against 40 MHz of the bunch crossing frequency. Energy thresholds are set for objects such as $E_T^{miss}, e/\gamma, \mu$ and Jet. When a signal exceeds the trigger threshold, the information is sent to the Central Trigger Processor(CTP) as the Region of Interest(RoI). Finally, a Level 1 Accept (L1A) is issued for an event that satisfies the trigger criteria, and the RoI information for the event is sent to the High Level Trigger.

High level trigger

In the High-level triggering, the events with L1A are analyzed in more detail by software to narrow down the number of saved events to 1 kHz. High-level triggers are analyzed based on the RoI information received from Level 1 triggers and using highly accurate detectors such as MDT, CSC, and ID. First, only the signal of detectors near the RoI is read out to enable calculations quickly, and the first trigger decision is made. After the first step, the information from all detectors is combined to identify the particles and reconstruct the trajectory. It is almost the same performance as the offline analysis, and the final trigger decision is made. The decision to save the event is made approximately 1 s after the bunch crossing of the event.

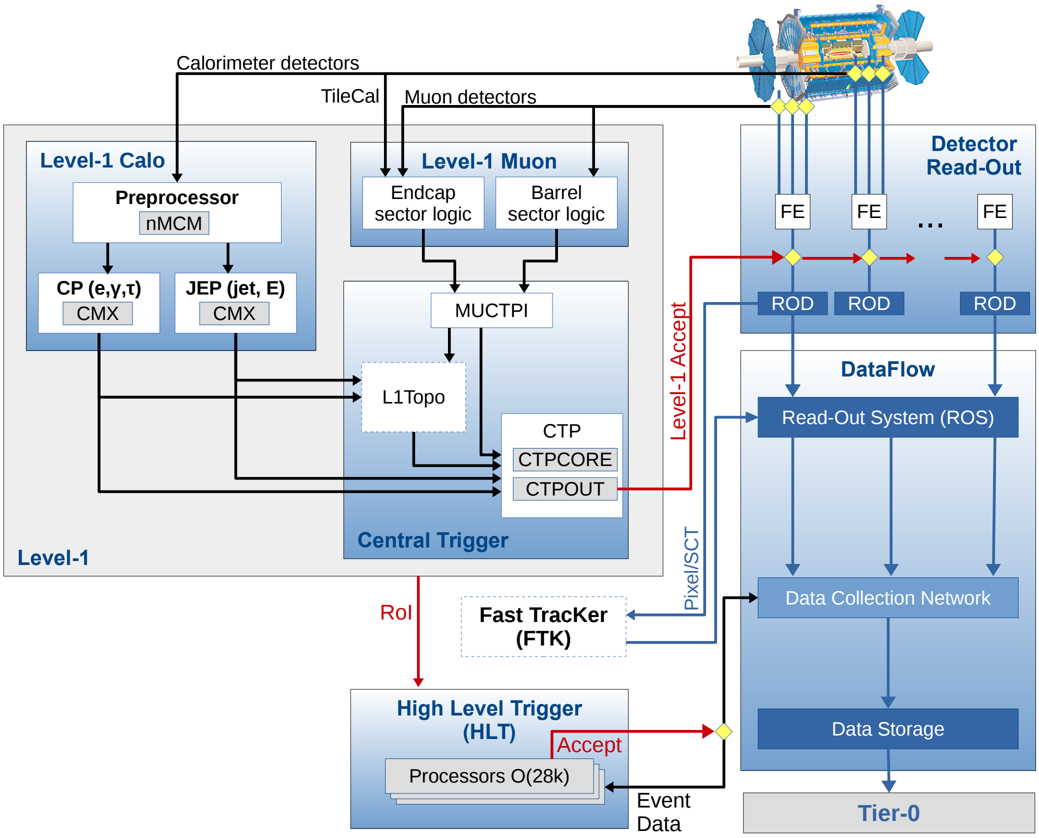

Figure3.10 A schematic diagram of the ATLAS trigger and data acquisition system in Run2[3].

4. Data and Monte-calro sample

In this section, the proton-proton collision data observed with the LHC-ATLAS experiment and simulated with the Monte Carlo method [35] used in this thesis are discussed. The MC simulation samples are used to understand the feature of the events that originated SM and SUSY.

4.1 Run2 data

The LHC provided 156 fb^{-1} of pp collision data with $\sqrt{s}$ = 13TeV during Run 2 in 215-2018. The ATLAS detector acquired 139 fb^{-1} of these pp collisions as data that can be used for physics analysis. As shown in Fig.3.2, about 33.7 collisions were observed per bunch crossing, and the discovery of neutralino using this data is aimed in this thesis.

4.2 Monte Carlo Simulation

In order to understand the characteristics of the events with neutralino and event of background(originated SM), MC simulation samples are generated. This simulation is divided into the following three processes.

- Hard scatter event generation
- pileup simulation
- detector simulation

Hard scatter event generation

First, how the pp collision generates particles is simulated. Protons have an internal structure, which is described as a Parton Distribution Function (PDF) (Figure 4.1).

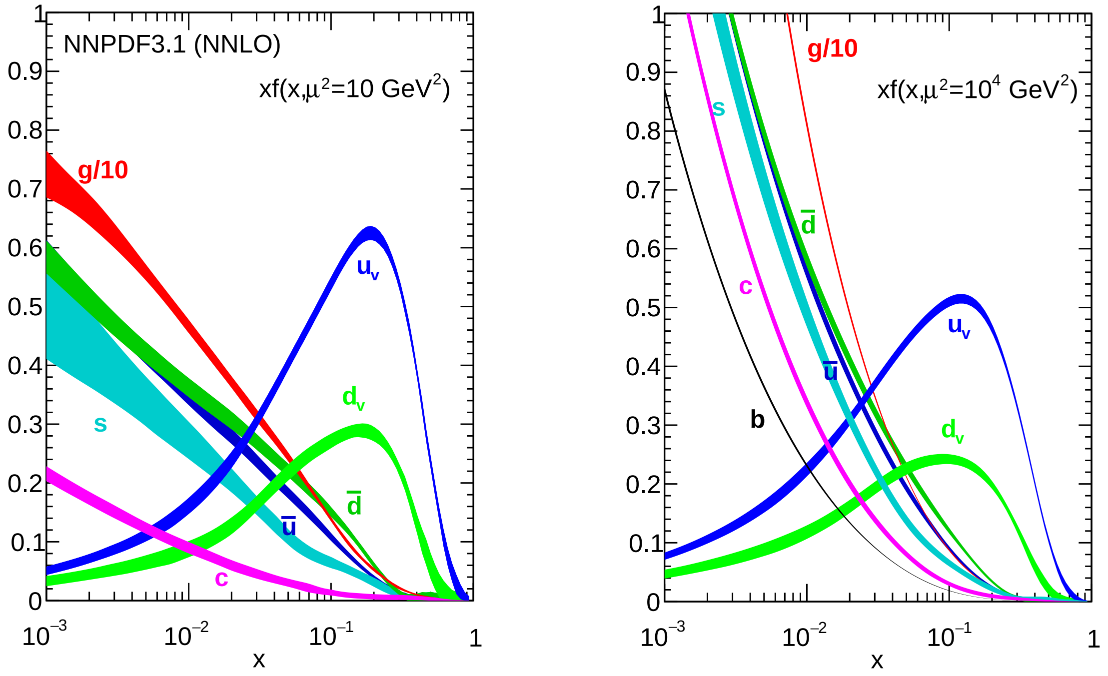

(a) μ^2 =10 GeV (b) μ^2 =10^4 GeV

Figure4.1 The NNPDF3.1 NNLO PDFs[4]

The differential cross section at the parton level is described by the matrix element $\mathcal{M}_{ab\to n}$. Here, $\mathcal{M}_{ab\to n}$ is described by the sum of all Feynman diagrams of the transition process of particles a and b to n ($ab \to n$). The gluons and color-charged particles emitted from the pp collision emit further gluons and quarks by the strong interaction. This continuous emission is referred to as "parton showering". Finally, all the color-charged particles are changed into color-neutral hadrons. This process is called hadronization. In this study, the W+jet sample and $t\bar{t}$ sample were used to understand the background. In the $W + jet$ sample, **NNPDF 3.0NNLO**[36] is used as PDF and **SHERPA2.2.1**[37] is used to calculate the matrix element and parton showering. In the $t\bar{t}$ sample, **NNPDF 2.3 LO**[38] is used as the PDF and **POWHEG − Box**[39] and **PYTHIA8.230**[40] are used to calculate the matrix element and parton showering, respectively.

Pileup simulation

As shown in Fig.3.2, multiple pp collisions occur in a single bunch crossing, and pile-up simulation simulates these effects. Moreover, this process considers not only pp collisions in the same bunch crossing but also neighboring bunch crossings.

Detector simulation

The response of the detector when a particle passes through the detector is simulated using the ATLAS simulation framework[41]. The simulation uses GEANT4 (GEometry And Tracking)[42], a widely used radiation simulation tool in high energy physics research.

4.3 Signal MC

In this Higgsino like LSP search, $pp \to \tilde{\chi}^0_2\tilde{\chi}^\pm_1$ and $pp \to \tilde{\chi}^0_2\tilde{\chi}^0_1$ samples are used. As a typical mass spectrum for the Higgsino like LSP scenario is $m(\tilde{\chi}^\pm_1) = \frac{1}{2}[m(\tilde{\chi}^0_1) + m(\tilde{\chi}^0_2))$. This sample was simulated using **MG5_aMC@NLO 2.6.1**[43] to simulate the hard scatter event and **MadSpin**[44] to simulate the neutralinos and chargeino decay. The neutralinos and chargeino's decays are simulated using **MadSpin**[44] . Also, **Pythia8.212**[40] is used to calculate the parton showering.

5. Object reconstruction

This chapter describes the object reconstruction and identification methods used in this study and the calibration method. The Low p_T calo tag muon, an object using the newly developed identification method, is discussed in the next chapter.

5.1 Track

The charged track is reconstructed as *track* using the signals from the pixel and silicon detectors. When the charged track passes through the pixel and silicon detectors, it loses energy and fires multiple channels. First, the signals of these channels are clustering using connected component analysis[45]. Three-dimensional space points are created from these clusters, and track seeds are reconstructed roughly using them. Next, based on the seeded tracks, the tracks are selected using Kalman filter[46].

A track candidate may have the same overlapping cluster with another track. It means the cluster is incorrectly assigned. In order to handle this overlapping correctly, the score of the track is calculated. The score is computed by the value of the cluster, hole, χ^2 of the track fit corresponding to the track. This score is used to reject the track or redistribute the clusters. Then, a high-resolution fit is performed based on the reassigned cluster information. Also, the reconstructed tracks are extrapolated to the TRT to improve the p_T resolution further. (The details can be found in Ref.[47].)

Track variables

The reconstructed track is described by the following five helix parameters;

$$P = (d_0, z_0, \phi_0, cot\theta, Q/p) \tag{5.1}$$

where, the d_0 and z_0 are the transverse impact parameter and the longitudinal impact parameter, respectively. The latter represents the distance from an arb point on the z-axis (beam pipe). Also, ϕ_0 and θ are the azimuthal and polar angles, respectively. The Q is the charge of the particle, and p is the momentum. The each parameters are depicted in Figure 5.1.

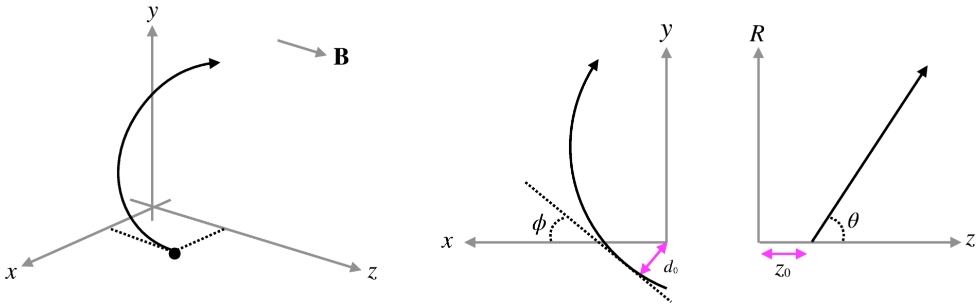

Figure5.1 Overview of a trajectory by a single charged particle, the three-dimensional view(left), xy-plane projected trajectory(center), Rz-plane projected trajectory(right).

5.1.1 Primary vertex

Based on the reconstructed tracks, the vertex is reconstructed using the vertex finding algorithm[48]. Each vertex is reconstructed with at least two tracks. Among the reconstructed vertexes, the vertex with the largest sum of p_T is referred to as Primary Vertex(PV), where a hard scattering occurred in pp collision

5.2 Jet

The quarks and gluons are converted into multiple hadron particles. In the ATLAS detector, this phenomenon is observed as a set of multiple tracks and topological clusters[49]. Topological cluster is an object reconstructed by merging energy deposits in each calorimeter cell. The object reconstructed from tracks and topo cluster is called a jet. In this section, the jet reconstruction method is summarized.

5.2.1 PFlow jet algorithm

The information from the topo cluster and tracks is used for the reconstruction and energy measurement of the jet. Typical energy and momentum resolutions for topo cluster and track are shown in eq.(5.2) and eq.(5.3), respectively.

$$\frac{\sigma(E)}{E} = \frac{50\%}{\sqrt{E}} \oplus 3.4\% \oplus \frac{1\%}{E} \tag{5.2}$$

$$\sigma(\frac{1}{p_T})p_T = 0.036\% \cdot p_T \oplus 1.3\% \tag{5.3}$$

Typically, in higher energy, the topo cluster has better energy resolution, while in the low energy,

p_T resolution of the track is better.

The PFlow jet algorithm[50] is used to subtract track energy from energy in the topo cluster to avoid a double count. The algorithm can be divided into four steps: track-topo cluster matching, split shower recovery, cell subtraction, and remnant removal. A schematic diagram is shown in Figure 5.2.

Track-Topo cluster matching

The first step is matching between the charged track and the topo cluster. The following equation is used.

$$\Delta R = \sqrt{\left(\frac{\Delta\phi}{\sigma_\phi}\right)^2 + \left(\frac{\Delta\eta}{\sigma_\eta}\right)^2} \tag{5.4}$$

Where $\Delta\phi$ and $\Delta\eta$ are the distance between the track and the center of the topo cluster, and σ_ϕ and σ_η are the width of the cluster. The topo cluster with the smallest ΔR is the topo cluster matched to the track.

Split shower recovery

A single particle-derived cluster may split into multiple clusters (the black and blue dotted lines in the second line of Figure 5.2). This process merges these split clusters into one. Since there is a correlation between track p_T and the energy of the topo cluster, the nominal deposited energy $< E^{ref}_{dep} >$ for track p_T is obtained. The reference deposited energy is given from the MC simulation. the clusters merged to be consistent with the $< E^{ref}_{dep} >$.

Cell subtraction

In this process, the energy of the cluster is subtracted. The subtraction of cells starts with the cell with the highest energy and then subtracts the energies of the cells closest to the cell. This process is repeated until the sum of subtracted energy reaches $< E^{ref}_{dep} >$.

Remnant removal

If a cell remains after the cell subtraction, the cell should originate neutral hadron or shower fluctuation. If the remaining energy is larger than 1.5σ compared to the E^{dep}/p_T^{track} distribution obtained from MC simulation, the cell remains as neutral-origin, and if it is smaller than 1.5σ, the cells are removed.

5.2.2 Jet reconstruction

After the energy subtraction, For jet reconstruction, the anti-k_T algorithm[51] is used, and The positive energy topo-clusters surviving the energy subtraction step and the selected tracks are used as inputs. In the algorithm, a distance is defined by the following equation.

$$d_{ij} = min(p_{Ti}^{-2}, p_{Tj}^{-2})\frac{\Delta R_{ij}^2}{r^2} \tag{5.5}$$

$$\Delta R_{ij} = \sqrt{(\eta_i - \eta_j)^2 + (\phi_i - \phi_j)^2} \tag{5.6}$$

Here, r is the parameter that determines the size of the jet, and r=0.4 is used in this thesis. To merge the objects, d_{ij} is calculate for all objects, and if the smallest d_{ij} is smaller than p_T^2, object i and j are merged into one. This process continues until $p_T^2 < any d_{ij}$. After the process, The merged objects is called jet.

5.2.3 Jet calibration

The jet energy scale calibration[52] restores the jet energy to that of jets reconstructed at the particle level. The full chain of corrections is illustrated in Figure 5.3. In every stage, the four-momentum, scaling the jet p_T,energy, and mass are recalculated according to each correction.

Pile-up corrections

In this process, the excess energy due to additional proton–proton interactions within the same or nearby bunch crossings is removed. These corrections consist of two components: a correction based on the jet area and transverse momentum density of the event, and a residual correction derived from MC simulation and parameterized as a function of the mean number of interactions per bunch crossing (μ) and the number of reconstructed primary vertices in the event (N_PV).

Absolute JES calibration corrects

This process correct the jet so that it agrees in energy and direction with truth jets from dij-et MC events.

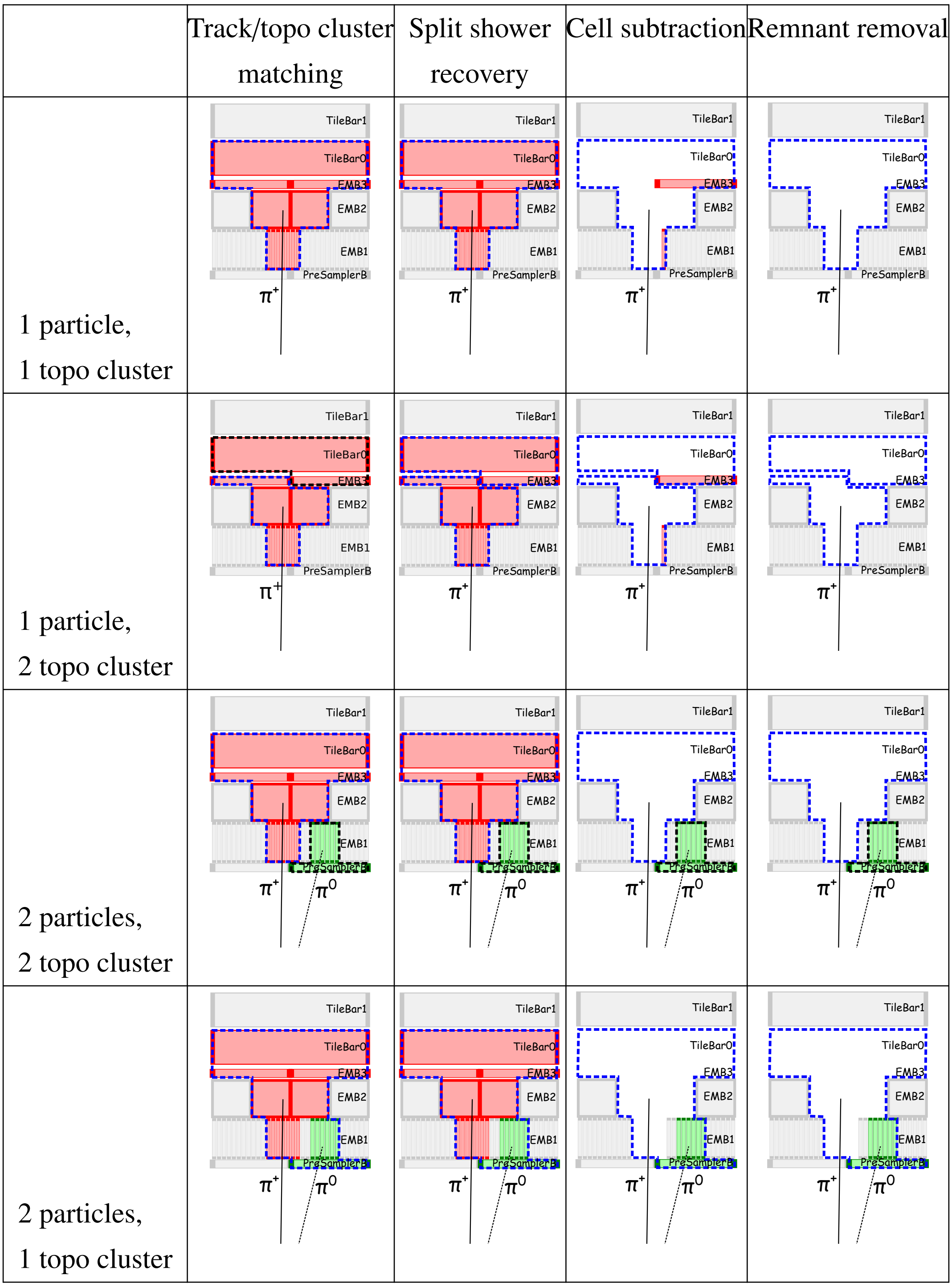

Figure5.2 Idealised examples of how the algorithm is designed to deal with several different cases. The red cells are those which have energy from the π^+, the green cells energy from the photons from the π^0 decay, the dotted lines represent the original topo cluster boundaries with those outlined in blue having been matched by the algorithm to the π^+, while those in black are yet to be selected. The different layers in the electromagnetic calorimeter (Presampler, EMB1, EMB2, EMB3) are indicated. In this sketch only the first two layers of the Tile calorimeter are shown (TileBar0 and TileBar1).

Global sequential calibration

This process (derived from dijet MC events) improves the jet p_T resolution and associated uncertainties by removing the dependence of the reconstructed jet response on observables constructed using information from the tracking, calorimeter, and muon chamber detector systems.

Residual in situ calibration

This process is applied to data only to correct for remaining differences between data and MC simulation. It is derived using well-measured reference objects, including photons, Z bosons, and calibrated jets, and for the first time benefits from a low-p_T measurement using the E_T^{miss} projection fraction method for better pile-up robustness.

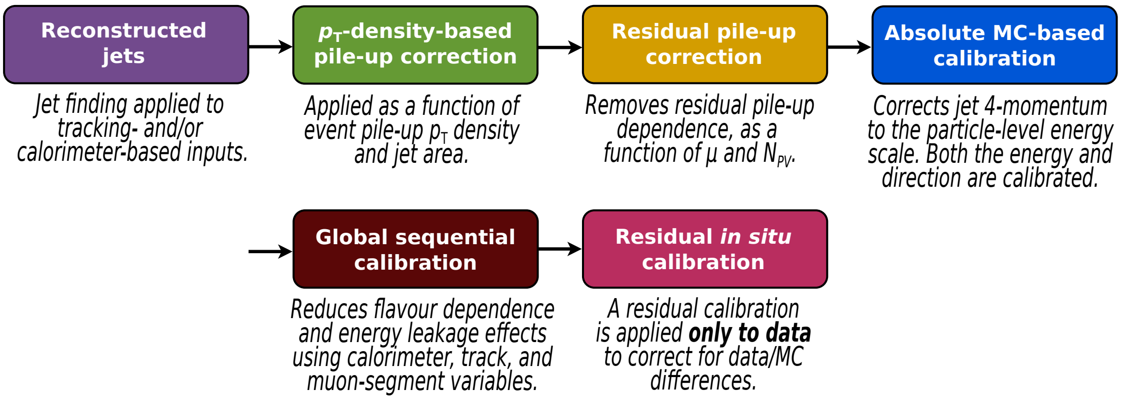

Figure5.3 Over view of the jet calibration[52]

5.2.4 Flavor tagging

Among the jets, the jet of b-hadron can be distinguished from other jets because the b-hadron has a longer lifetime of $c\tau \simeq 500\mu$m. As a result, the impact parameters of tracks of the jet, such as d_o and z_0, become larger, and the secondary vertex, which is farther away from the primary vertex, is reconstructed. Also, the decay of the b-hadron can be identified by finding the chain that contains the third vertex since the decay chain of the b-hadron → c-hadron → light-hadron create three vertexes. [53] Several b-tagging algorithms have been proposed to take advantage of the above features. As Impact parameter base algorithms, IP3D and RNNIP tagger are used. Also, SV1 as a secondary vertex finding algorithm is used. Furthermore, JetFitter is used as a decay chain multi-vertex algorithm.

The variables obtained from these algorithms are finally used as input for Deep Neural Network (DNN), which is a kind of machine learning, and the output of this DNN is a score from 0 to 1, representing the jet is the b-jet like or not. This algorithm is referred to as DL1r. This study used a working point of 85% b-jet tagging efficiency[54].

5.3 Muon

This section discusses the reconstruction, identification, and isolation of muon candidates. (The detail can be found in Ref.[55]). First, muon candidates can be reconstructed with high efficiency. Next, the identification algorithm suppresses muons from hadron decay-in-flight. In addition, muons originated semi-leptonic decay of heavy hadrons are suppressed by requiring isolation. The details of each step are shown below.

5.3.1 Reconstruction

The muon is reconstructed by four type of methods. Figure 5.4 shows the schematic drawing of the methods.

Combined muons

When a track reconstructed by the inner detector matches a track reconstructed by muon spectrometer, one combined muon is reconstructed by global fitting.

Segment-tagged muons

Segment-tagged muon is an object reconstructed with an inner detector track and a track segment of muon spectrometer. A track segment muon is an object that is reconstructed using the information of a part of layers of the MDT or CSC, which is a looser criterion than one for the muon spectrometer used for the combined muon.

Calorimeter-tagged muons

An inner detector track is identified as a calorimeter-tagged muon if its energy deposit in the calorimeter is compatible with the one of minimum ionizing particle. It is used to recover efficiencies at the $|\eta| < 0.1$ region, where the coverage by the muon spectrometers is limited. Also, inner detector track with $p_T > 15$ GeV is used for the calorimeter-tagged muons reconstruction.

Standalone muons

The muon spectrometer tracks which are extrapolated to the interaction point are reconstructed as standalone muons. The standalone muons are used to recover acceptance in the $2.5 < |eta| < 2.7$ region, where the inner detectors don't cover.

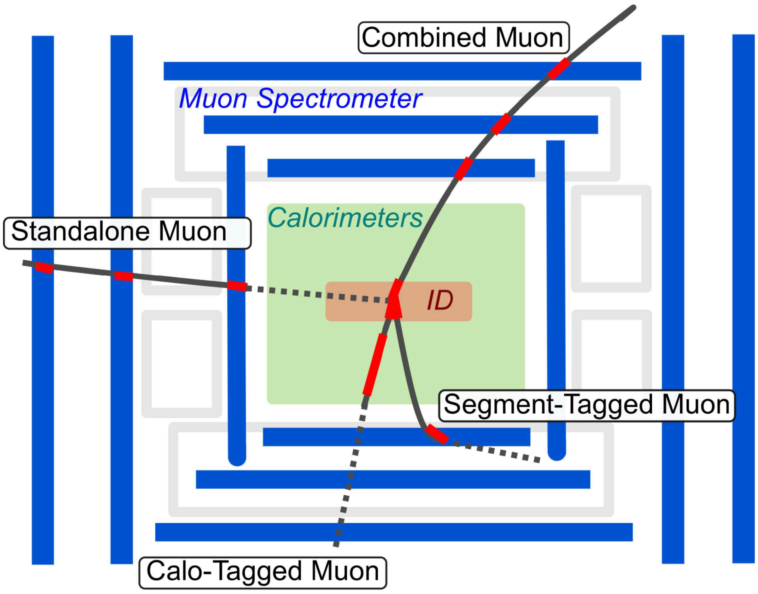

Figure5.4 Schematic drawing of the muon reconstruction methods[56].

5.3.2 Identification

The identification algorithm suppresses muons originated the light hadron decay. Frequently, the decayed muon and th parent charged hadron is reconstructed as a combined muon track. In such a case, muons are characterized by the presence of a distinctive "kink" topology in the reconstructed track. Therefore, the fit quality of the tracks results can be used as the discriminate variable. By using fit quality, five muon identification working points have been defined: Loose, Medium, Tight, LowPt, and HighPt.

Here, LowPt is a WP targeting low p_T region(3 to 10 GeV). For low p_T muon, the deposited energy at the calorimeter should be taken into account when comparing the momentums since the muon momentum and the deposited energy at the calorimeter are equivalent. Also, fake tracks and tracks originated in-flight hadron decays can be suppressed by evaluating the smoothness of inner detector tracks. The performance of LowPt WP is shown in Fig5.5. In the search for Electrowikino with compressed mass spectra, low p_T muon is dominant. Therefore, LowPt WP is used.

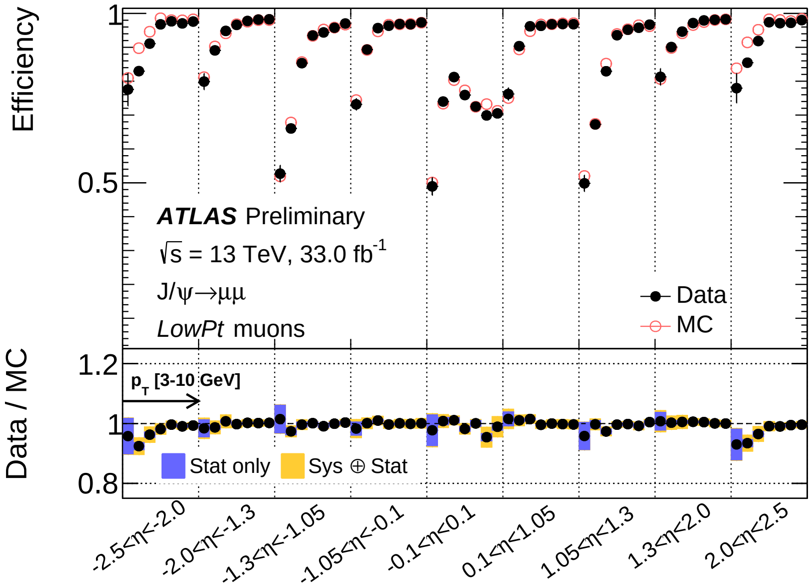

Figure5.5 Muon reconstruction efficiencies for the LowPt WP measured using $J/\psi \to \mu\mu$ events as a function of the muon η and for different p_T ranges, up to 10 GeV[55].

5.3.3 Isolation

This analysis requires track base isolation given by eq.5.7.

$$p_T^{varcone30}/p_T^{\mu} < 0.06 \tag{5.7}$$

Here, p_T^{μ} is the transverse momentum of the muon and $p_T^{varcone30}$ is the sum of p_T of all tracks within ΔR defined by the following equation.

$$\Delta R = \min(10\mathrm{GeV}/p_T^{\mu}, 0.3) \tag{5.8}$$

This working point is called *TightTrackOnly* and has an efficiency of 80% for prompt muons with p_T of 3 to 5 GeV[55].

5.3.4 Calibration

To correct the difference in the LowPt identification efficiency between data and MC, each efficiency is calculated using the tag and probe method with $J/\psi- > \mu\mu$ events. The data/MC ratios are shown in the lower part of Fig5.5. a few % of miss-modeling is observed, and this miss-modeling is corrected by applying a pT-dependent scale factor to the MC events.

5.4 Electron

This section briefly discusses the reconstruction, identification, and isolation of electrons[57]. First, the electron candidates are selected by reconstruction. However, many of them are from backgrounds (from jets and photons), and then an identification algorithm needs to reject them. In addition, electrons from the semi-leptonic decay of hadron can be distinguished by requiring isolation from other objects. The details of each step are discussed below.

5.4.1 Reconstruction

Trajectory of an electron can be observed by the inner detectors. Also, an electron causes an electromagnetic shower in the electromagnetic calorimeter. Therefore, an electron is reconstructed by position matching between track and topo-cluster. After that, the direction and p_T of the matched track is corrected by using taking which takes into account the effect of bremsstrahlung.

5.4.2 Identification

The Identification step rejects background such as photons, hadrons in light flavored jets, and non-prompt electrons from semi-leptonic decay of heavy hadrons. The Identification algorithm is based on likelihood and uses 14 variables, including the shape and depth of the topo-cluster, the quality and impact parameters of the track, and the TRT information. Probability density functions (PDF) derived from $J/psi \to ee$ and $Z \to ee$ MC samples are used in the likelihood. The working point of likelihood threshold is defined as a function of MET and eta since. The ATLAS experiment defines four working points as VeryLoose, Loose, Medium, and Tight. Fig5.6 shows the efficiency at the Loose, Medium, and Tight working points measured using $Z \to ee$ events.

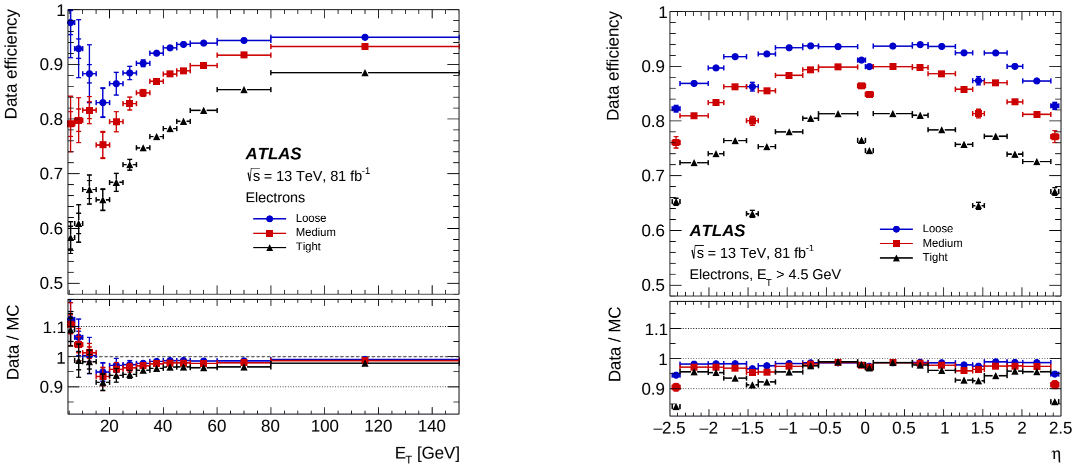

(a) E_T^{miss}

(b) η

Figure5.6 Electron identification efficiency as a function of E_T (left) and η (right) for Loose, Medium and Tight working points[57].

5.4.3 Isolation

Isolation applied the same track base criteria as muon (see section 5.3.3 for details).

5.5 Missing Transverse Energy

Since the LHC has zero initial transverse momentum, the conservation of transverse momentum is useful to find signture from neutrino and neutralino. neutrino and neutralino can be mesured directry but the vector sum of these particle's p_Ts can be estimated from this conservation. The missing transverse momentum (E_T^{miss}) is defined the below[58].

$$E_T^{miss} = -(\Sigma E_T^{jet} + \Sigma E_T^{\mu} + \Sigma E_T^{e} + \Sigma E_T^{\gamma} + \Sigma E_T^{softterm}) \tag{5.9}$$

where E_T^{jet}, E_T^{μ}, E_T^{e}, E_T^{γ}, $E_T^{softterm}$ are the transverse momentum of jet, electron, photon and muon. The soft term ($E_T^{softterm}$) is calculated from tracks in the inner detector. By considering soft term, the pileup contamination of E_T^{miss} can be minimized and thus the resolution become robust to the number of primary vertex.

In addition, **Track E_T^{miss}** is defined based on the momenta of tracks, a measure which is largely independent of the pile-up, but insensitive to neutral particles and has an acceptance limited by the tracking volume of the inner detector.

5.6 Overlap removal

The jet, electron, and muon are reconstructed independently. Therefore, a single particle may be reconstructed as multiple objects. Overlap removal is a process to resolve these ambiguities. The steps are summarized below.

- Muon-Electron overlap
  If the track is shared, remove the electron.
  This will reject electron from the bremsstrahlung.

- Lepton-Non b-tagged jet overlap
  For electron, if $\Delta R_{jet,electron} < 0.2$, jets are removed.
  For muon, if Jets with fewer than three tracks and $\Delta R_{jet,muon} < 0.4$, jets are removed.

- Jet-Lepton overlap
  If $\Delta R_{jet,lepton} < 0.4$, leptons are removed.
  This will reject the lepton from the b- and c-hadron decay.

6. Low pT Muon Identification

This chapter describes a newly developed algorithm dedicated to low-momentum muon identification.The standard muon identification method in the ATLAS experiment is inefficient for muons with p_T below 3 GeV. The red box in Figure 6.1 shows the efficiency which combined reconstruction, identification, isolation, and vertex association efficiency. The reason is that low pT muons stop inside calorimeter and cannot reach the muon spectrometer.

Several other methods have been proposed for muon identification, and the schematic diagram is shown in Figure 6.2. The standard muon identification method uses *Combined Muon*, which is a track reconstructed by both the inner detector and the muon spectrometer. On the other hand, the *Standalone Muon* uses the tracks reconstructed by only the muon spectrometer. Also, the *Segment-tagger Muon* is a combined track of the tracks reconstructed by inner detector and a part of muon spectrometer. In addition, another algorithm named Calo-Tagged Muon doesn't use muon spectrometer bu uses inner detector and calorimeter. The black box in Figure 6.1 shows the efficiency when all the algorithms are used except for the *Combined Muon*. Improvement of the efficiency below 3 GeV can be seen, but still low efficiency below 2 GeV. This is because the Calo-Tagged Muon is developed to cover the muon spectrometer hole, and is basically applied to the High p_T muon. Thus, it cannot recover the efficiency of the low p_T muon.

In this study, We've developed a new algorithm to identify low-momentum muons using only inner detector and calorimeter to improve the efficiency. In addition, deep neural network, a kind of machine learning, is used to maximize performance.

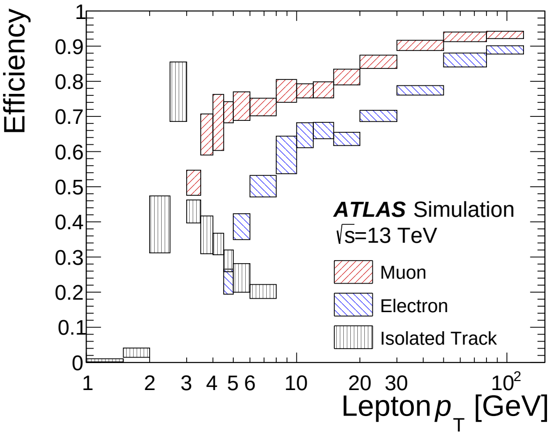

Figure6.1 Efficiencies, which combined reconstruction, identification, isolation, and vertex association efficiency. The red box represents the efficiency for muon and its uncertainty. The black box is the efficiency using several not standard identification algorithms for lepton.

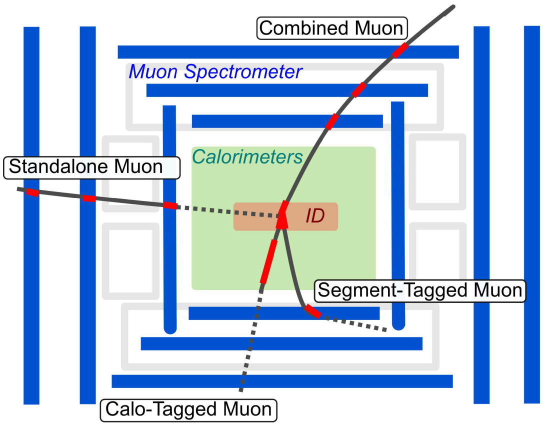

Figure6.2 Identification algorithms available in the ATLAS experiment[55][59]

6.1 Low p_T calo tag muon Algorithm

This section describes the details of newly developed method named as Low p_T Calo Tag muon algorithm (hereafter referred to as LCaT muon algorithm). This algorithm is used to distinguish muons from other particles in low p_T region. Other particles refer to hadrons and fake tracks, where the fake track is a misidentified track which is accidentally reconstructed from hit points of multiple particles.

The basic idea of LCaT muon algorithm is to use the difference of deposit energy in the calorimeter between muons and hadrons. Muons leave small energies like minimum ionization particles (MIP) in the calorimeter. On the other hand, hadronic particles such as pions produce second particles in a cascade due to strong interactions, and therefore give energy clusters with larger than MIP (Figure 6.3). These energy clusters are reconstructed as topological clusters [49](hereafter referred to as calo cluster). The deposited energy in each layer can be larger than MIP for hadrons, while it is almost same as MIP for muons (Figure 6.4).

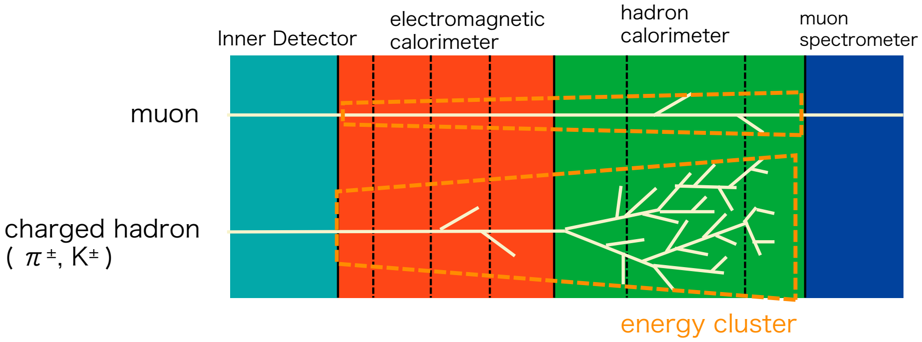

Figure6.3 Diagram of the particle behavior in the detectors. The white line represents a trajectory of a particle. The muon rarely emit particles in the calorimeter and deposits about the energy of MIP in each layer. On the other hand, hadron particles deposits large energy due to emission of many particles.

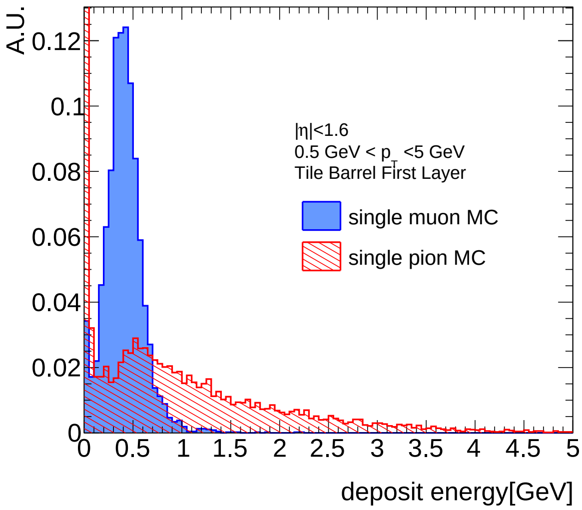

Figure6.4 Deposit energy distributions of muon and pion in the first layer of the Tile barrel. Muon has a peak around 0.5 GeV (MIP), while the deposit energy of pion is mostly distributed above MIP.

Muon calo cluster efficiency

First, we discuss the calo cluster efficiency. The calo cluster efficiency is the efficiency for that muon energy cluster are reconstructed as calo cluster. Figure 6.5 shows the p_T dependence and η dependence of the efficiency. The efficiency decreases in the region where p_T is less than 1 GeV. For $|\eta|$, the efficiency is almost zero in the region outside of the Tile cal including extended barrel (see 3.2.3). The noise to be considered in the calorimetry is the electronics-derived noise and the pileup-derived noise [49]. Pileup-derived noise increases as closer to the beam pipe and increases one order larger than in the small eta region. Thus, pileup-derived noise is so high in FCal ($|\eta|$>1.6) that efficiency decreases so much. For this reason, the LCaT muon algorithm targets muons with p_T higher than 0.5 GeV and $|\eta|$ smaller than 1.6.

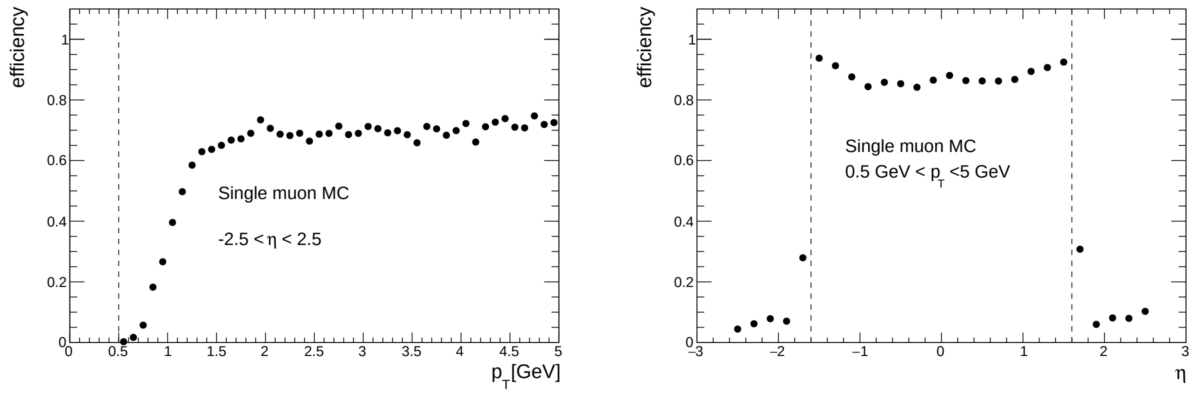

(a) (b)

Figure6.5 p_T and η dependence of the muon calo cluster efficiency in single muon MC. (a) p_T dependence: the efficiency is decreasing since the energy of muon is not enough to produce the calo cluster (b) η dependence: the efficiency is high enough in small $|\eta|$ region. In the high $|\eta|$ region, loose efficiency can be found since tight criteria to produce the calo cluster.

Track and calo cluster position matching

Since multiple calo clusters are reconstructed in an event, position matching is necessary to narrow down the calo clusters generated by a certain track. In order to request the position matching between track and calo cluster, $\Delta\eta$ and $\Delta\phi$, which are defined as equation 6.1 and 6.2, respectively, are used

$$\Delta\eta = \eta_{track\_at\_IP} - \eta_{calo\_cluster} \tag{6.1}$$

$$\Delta\phi = |\phi_{track\_at\_IP} - \phi_{calo\_cluster}| \tag{6.2}$$

Fig 6.6 shows distribution of $\cos\Delta\phi$ and $\Delta\eta$. The matching requests that $\cos\Delta\phi$ should be larger than 0.6 and $|\Delta\eta|$ should be smaller than 0.15. In addition, to examine position matching in ϕ direction, it is necessary to extrapolate the track in the inner detector to the calorimeter surface by taking the solenoid magnetic field into account. The extrapolation equation considering the track charge and p_T is also used below.

$$\sin\Delta\phi = (-1)^{charge} \times A/p_T \tag{6.3}$$

,where A is a constant value that depends on the strength of the magnetic field and the radius of the detector. Fig 6.6(c) shows distribution of $\sin\Delta\phi$ vs $1/p_T$ in single muon MC. From this result, A is set to 0.5.

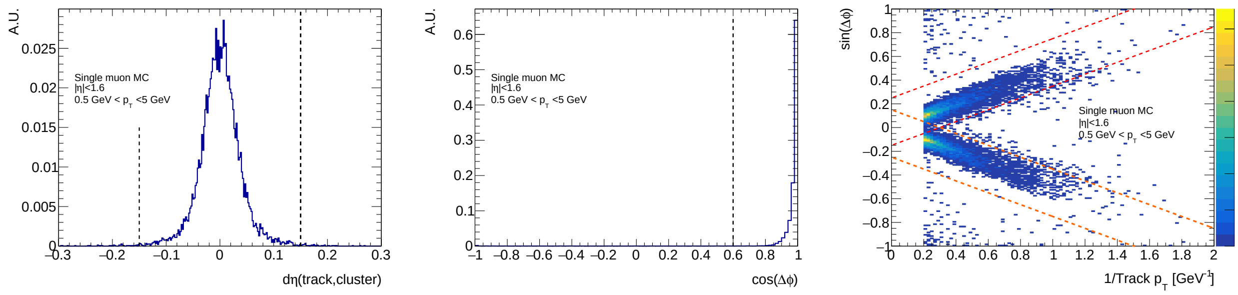

(a) (b) (c)

Figure6.6 Distribution of variables used position matching in single muon MC. (a) $\Delta\eta$ (b) $\cos\Delta\phi$ (c) $\sin\Delta\phi$ vs p_T: entries are separated into two clusters. The upper cluster consists of negative charge muon. The lower cluster consists of positive charge muon.

Position matching criteria are summarized in Table 6.1. Only the calo clusters that satisfy the position matching are used in the LCaT muon algorithm.

Table6.1 Summary of position matching criteria.

variable		range
$\sin\Delta\phi - (-1)^{charge} \times 0.5/p_T$	positive charge	[-0.15,0.25]
	negative charge	[-0.25,0.15]
$\cos\Delta\phi$		> 0.6
$\|\Delta\eta\|$		< 0.15

Deep Neural Network

To discriminate muons from other particles as efficiently as possible, we use a Deep Neural Network (DNN), which is a machine learning algorithm that learns how to discriminate signals and backgrounds from a large amount of signal and background data. The design of the DNN is shown in Figure 6.7 and the detailed role of each layer is described in **??**.Hereafter, refer to this DNN as the LCaT DNN. The track η, p_T, and the deposit energy in each layer of the calo cluster are used as inputs for LCaT DNN. In this study, LCaT DNN is trained using muons as the signal and other particles as the background in J/ψ MC. Speaking precisely, the muon from the J/ψ decay is used as the signal, and tracks that is far enough away from the muon is used as the background.

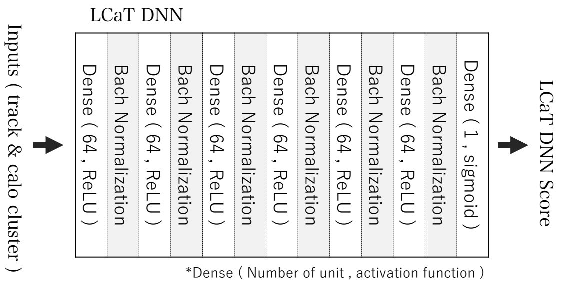

Figure6.7 Design of LCaT DNN. Inputs are track pT and eta and deposit energy in each calorimeter layer. Seven dense layers and six bach normalization layers are used.The last layer is a dense layer with a sigmoid activation function.The output is from 0 to 1.

LCaT DNN learns how to discriminate between muons and other particles based on the distribution and correlation of these variables. The output is a continuous value from 0 to 1, which is refer to as the LCaT DNN score. The score close to 1 means it is more likely to be muon.

In this study, we use a training method called supervised learning, which teaches which data is signal and which data is background while learning how to discriminate them. However, there is a problem with the information of the calo cluster. By using the truth information of the simulation, it is possible to identify whether the track is from muon or background with high accuracy. On the other hand, it is difficult to identify which particle generates a certain calo cluster. As shown in Fig.6.8, multiple candidates remain for one muon even if the position matching is required. However, only one of them is generated by the muon, and the others are calo clusters generated by hadronic particles. Therefore, if all matched clusters are used as 'signal' in learning, the calo cluster generated by the hadronic particles may be taught as the muon-generated calo cluster. As a result, incorrect information is taught. It results in unstable learning and low discrimination performance.

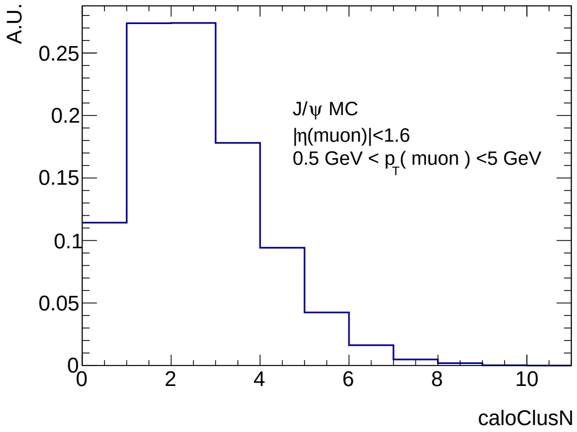

Figure6.8 The number of calo clusters, which satisfied the position matching, in J/ψ MC. Most muons produce one calo cluster. However, muon tracks in J/ψ MC satisfy position matching with many calo clusters since there are hadron-generated calo clusters near the muon track.

A training method named "Supervised training with Self Selected Input data (SSSI)" has been developed to solve this problem. Figure 6.9 shows design of the network used in SSSI.

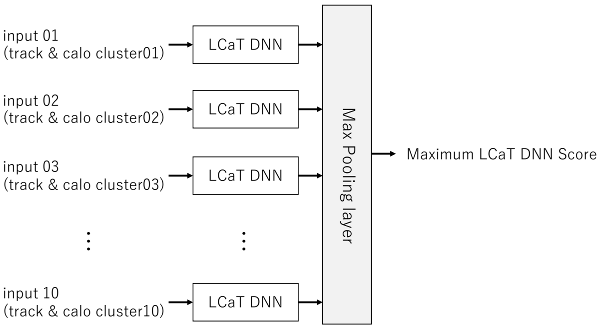

Figure6.9 Design of DNN for SSSI. LCaT DNNs are connected via MaxPooling. The same track information and different calo cluster information are input to each LCaT DNNs.

The outputs of LCaT DNNs (Figure 6.7) are connected in parallel as inputs to MaxPooling. MaxPooling is a layer that selects the cluster with highest score from all inputs. Training is performed using only the information selected by MaxPooling. This design is very similar to CNN, one of deep learning used for image recognition. For example, CNN can identify whether a cat is in a photo with high accuracy. In the training of CNN, the supervisor does not need to tell it where the cat is, but only whether the cat is present or not. Thus, CNN has the ability to search for cats and learn their characteristics by itself. Similarly, SSSI can learn the features of muon-generated calo clusters only from the information on whether there is a muon-generated calo cluster among inputs.

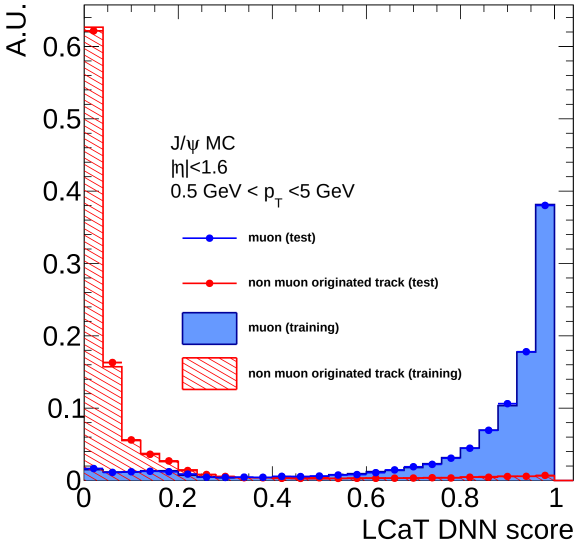

Figure6.10 Distribution of LCaT DNN score. The blue dots and histogram are the distributions of test and training of LCaT DNN scores for the muon, respectively. Similarly, The red dots and histogram are for the non-muon track. There is no difference between test data and training data. Therefore, The LCaT DNN has high generalization performance.

Before the training of the LCaT DNN, the training data and test data were randomly selected, and only the training data was used for training. Figure 6.10 shows the LCaT DNN score distribution. As a result,the same results were obtained for both training and test data. Thus, we conclude that DNN with high generalization performance could be realized without overtraining.

Also, as a caveat, the DNN used for analysis is the LCaT DNN, which is disconnected from MaxPooling after training.

6.2 Working Point

This section describes how to determine muon or not from the LCaT DNN score. Since the LCaT DNN score is a continuous value from 0 to 1, it is necessary to set a threshold value to the score. First, we describe how to set the threshold value and summarize the performance at the threshold.

6.2.1 Definition of WP

The LCaT DNN was trained using data with flat p_T distribution to avoid muon identification only by the value of p_T. However, once the target physics is determined, the p_T distribution can be used to determine whether the track is the muon or not. In detail, since this study aims to identify muons from Electroweakino decay, the threshold of the LCaT DNN score can be loosened in regions where there are many muons originated from Electroweakino decay and few background particles. By contrast, the threshold should be tightened in p_T regions where the number of the muon is small and the background is large. Also, a similar adjustment should be made for eta. In other words, the threshold of LCaT DNN score is determined as a function of p_T and eta.

However, it is not obvious how to set the threshold effectively for Electroweakino search, and what function should be used can't be determined in a simple way. To solve this problem, another DNN, referred to as WP DNN, is introduced to evaluate the LCaT DNN score for given p_T and η. This WP DNN uses p_T, η, and LCaT DNN scores as input, and the output is referred to as WP DNN score. The WP DNN score takes a continuous value from 0 to 1.

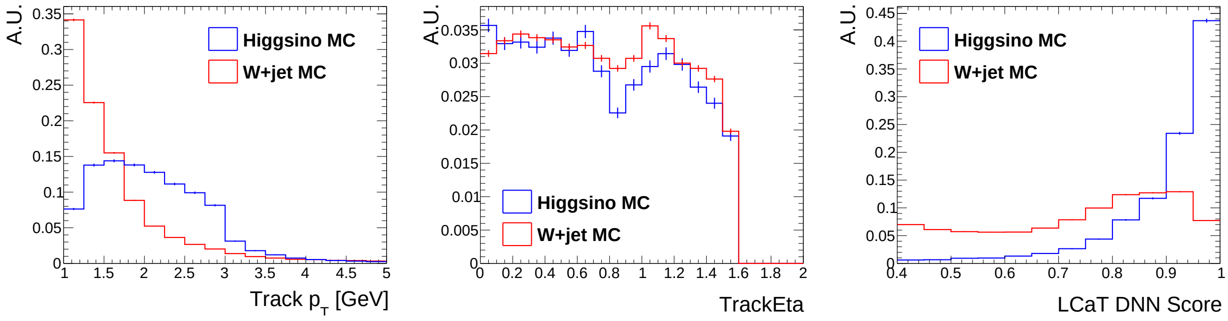

(a) (b) (c)

Figure6.11 Distribution of inputs for WP DNN. The blue line is a distribution of muon in Higgsino MC. The red line is a distribution of non-muon originated track in W+jet MC. (a) track p_T (b) track η (c) LCaT DNN score

Determining the WP DNN score threshold is equivalent to determining the boundary in the 3D space of the p_T, η, and LCaT DNN scores (i.e., determining the threshold for the LCaT DNN score as a function of p_T and eta.) For training, Higgsino MC is used as signal data and W+jet MC is used as background. The distribution of input is shown in Figure 6.11. For p_T distribution, the fraction of muons from Electroweakino decay increases around p_T 2 GeV.

6.2.2 Performance

Figure 6.12 shows the distribution of the output after training.

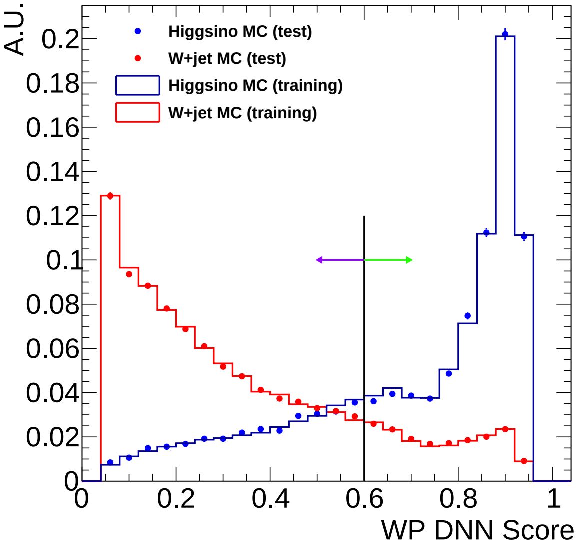

Figure6.12 WP DNN score distributions. The blue dots and histogram are the distributions of test and training of LCaT DNN scores for the muon in Higgsino MC, respectively. Similarly, The red dots and line are for the non-muon track in W+jet MC. There is no difference between test data and training data. Therefore, The WP DNN has high generalization performance.

A good separation between signal and background can be seen, and there is no overlearning. Figure 6.13 shows p_T and η dependence of the LCaT DNN score threshold when the WP DNN score threshold is set to 0.6. Light green and purple are entries distinguished as signal and background, respectively.

It can be seen that the threshold value is loosened in the region where the ratio of muon came from higgsino decay is high (around 2 GeV). For eta, the threshold becomes tighter around |eta| = 1. This region is the boundary between the tile barrel and the tile extended barrel, and it is expected that the threshold is tight because it is difficult to distinguish muon and others due to the complex structure of the calorimeter.As shown in Figure 6.13, complex threshold boundary settings can be made by simply setting the threshold of the WP DNN score. In addition, it is easy to make the threshold boundary tighter or looser by simply shifting the threshold of the WP DNN score. It is an important point in the optimization of the threshold in Higgsino search.

Finally, The pT dependence of efficiency in higgsino MC and W+jet MC is shown in Figure

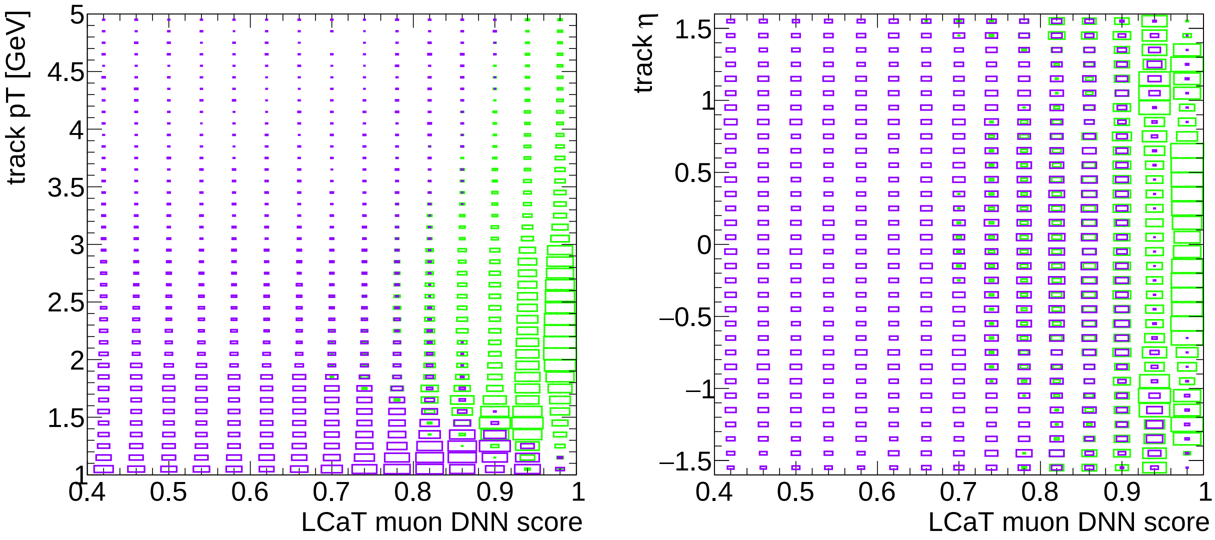

(a) (b)

Figure6.13 Distribution of inputs for WP DNN. Light green is entries that are distinguished as a muon. Purple is entries which identified as a non-muon track. The size of the box represents the number of entries. (a) track p_T (b) track η (c) LCaT DNN score

6.14. The improvement of the identification efficiency can be found when compared to the performance of the conventional algorithm (Fig. 6.1). Especially, the efficiency improved about 2 to 6 times in the p_T region from 1.5 to 2.5 GeV.

In this study, the WP with a threshold at 0.6 for WP DNN score is defined as ***Higgsino WP*** .

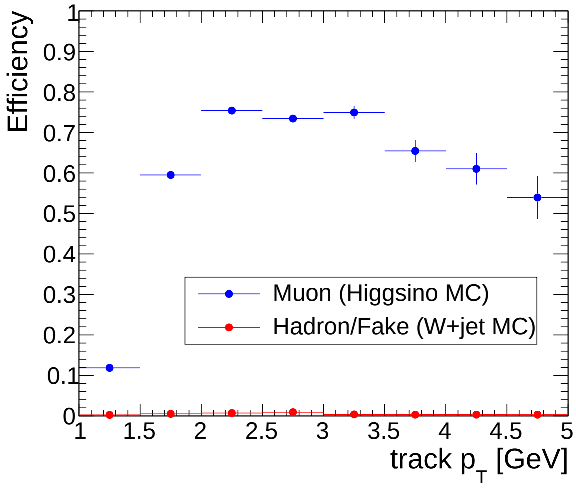

Figure6.14 LCaT muon ID efficiency in Higgsino MC and W+jet MC.The red dot is the identification efficiency for muon in Higgsino MC.The red dot is the identification efficiency for non muon track in W+jet MC. The high efficiency for muon is kept in the low p_T region, while the efficiency for non-muon tracks is kept below 2%.

7. Event Selection

The blind analysis is adopted for the SUSY search. First, the Signal Region (SR) is defined to evaluate number of signal events. The SR is determined to maximize signal to background ratio. Next, The contamination of backgrounds in the SR is estimated without using observed events in the SR (i.e. the SR is blinded from the analysis). Then, the SR is opened to examine how many signal events are. The event selection to the SR is critical for finding that the number of the signals is significantly large with respect to the background error.

In this chapter, we summarize the signal features and discuss the details of the event selection to the SR.

7.1 Analysis strategy

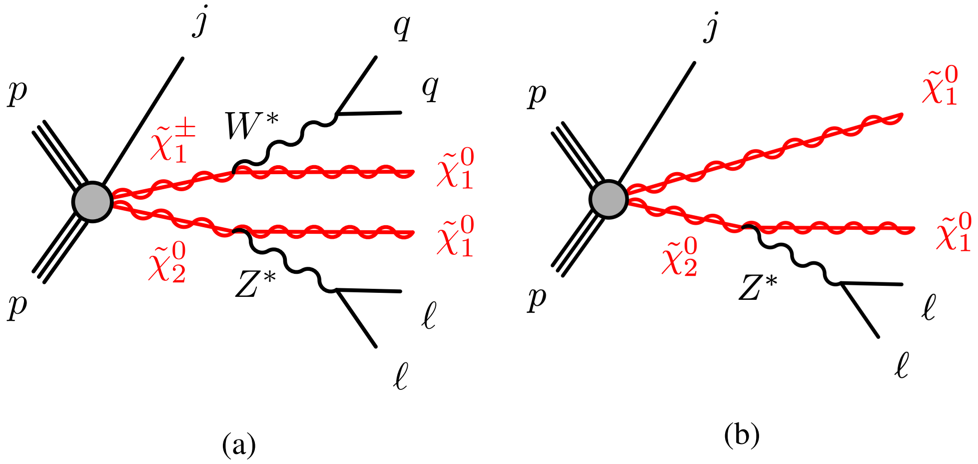

Figure7.1 Feynman diagram of target physics. The j represents the ISR jet. (a) production of $\tilde{\chi}_1^\pm$ and $\tilde{\chi}_2^0$. off-shell W boson can also decay into leptonic. (b) $\tilde{\chi}_2^0$ and $\tilde{\chi}_1^0$

The main production process of $\tilde{\chi}_2^0$ is shown in Figure 7.1. The target event is that $\tilde{\chi}_2^0$ decays into $\tilde{\chi}_1^0$ with an off-shell Z boson which decays into two muons. The decay process of $\tilde{\chi}_1^\pm$ is not specified. It means that $\tilde{\chi}_1^\pm$ may produce an off-shell W boson which decays hadrons or leptons. Furthermore, $\tilde{\chi}_1^0$ is expected to pass through the detector without decaying due to R-parity conservation. Usually, particles that carry away energy are indirectly observed as E_T^{miss}(defined in section 5.5), but when two $\tilde{\chi}_1^0$ are emitted back to back, E_T^{miss} becomes 0. As a result, $\tilde{\chi}_1^0$s can't be observed. To solve this problem, Initial State Radiation jet with high p_T (ISR jet) is required and SUSY system is boosted. Hence, two $\tilde{\chi}_1^0$ are emitted in the opposite direction of the ISR jet ,and can be observed as E_T^{miss}. Moreover, high E_T^{miss} can be used as a trigger signature.

In addition, features of the off-shell Z boson are also useful. The maximum mass of the off-shell Z boson is the same with the mass difference between $\tilde{\chi}_2^0$ and $\tilde{\chi}_1^0$ ($\Delta m(\tilde{\chi}_2^0,\tilde{\chi}_1^0)$). Since the target $\Delta m(\tilde{\chi}_2^0,\tilde{\chi}_1^0)$ of this analysis is between 1 and 5 GeV, a light off-shell Z boson is generated. Therefore, the muons from the off-shell Z boson must be low p_T dominant. Also, since SUSY system is boosted by the ISR jet, the off-shell Z boson is close to E_T^{miss}. Therefore, the two leptons from the off-shell Z boson are boosted. As a result, the direction of the momentum of muons must be close.

The above features are summarized in the following list, and a schematic diagram of a typical event is shown in Figure7.2. The decay-derived particles in $\tilde{\chi}_1^\pm$ are omitted.

- Objects
  - High p_T ISR jet.
  - High E_T^{miss}.
  - 2 low p_T muons.
- small angle between E_T^{miss} and off-shell Z boson
- small invariant mass of off-shell Z boson
- small angle between 2 muons

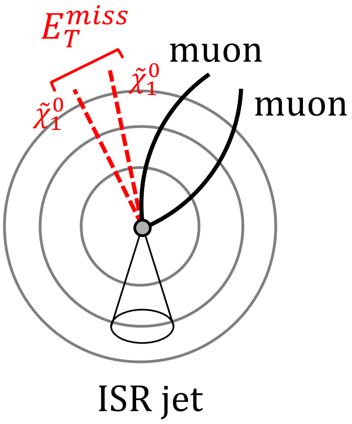

Figure7.2 Event diagram from the cross section of the ATLAS detector. The beam pipe is installed from the front of the paper to the back. muons and E_T^{miss} is SUSY originated objects. ISR jet boosts the SUSY system.

The bottleneck in the previous study [9] was small efficiency of the muon identification in the low pT region. Since small $\Delta m(\tilde{\chi}_2^0, \tilde{\chi}_1^0)$ makes muon p_T smaller, the decrease in muon identification efficiency could be more serious.

To solve this problem, the newly developed LCaT muon ID is applied to one out of two muons. On the other hand, another muon is required to be the signal muon (section 5.3) to suppress the background.

7.2 Trigger Selection

This section describes the triggers used in this analysis. The E_T^{miss} trigger is used since two $\tilde{\chi}_1^0$ with high p_T pass through detectors. $E_T^{miss} > 200$ GeV selection is required in SR.

Figure 7.3 shows the performance of the E_T^{miss} trigger in Run2. [60].

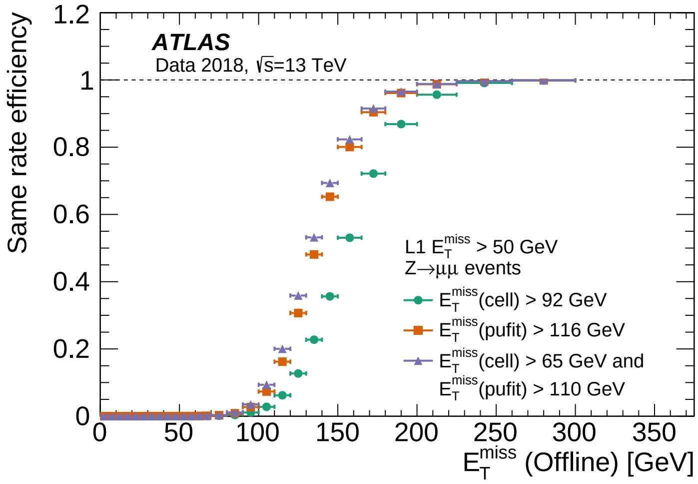

Figure7.3 E_T^{miss} trigger efficiency in Run2 [60]. The efficiency changes with the period, but above 200 GeV, the efficiency is kept above 95% stably.

It can be seen that the trigger efficiency fluctuates with each period. It is because the E_T^{miss} trigger threshold is adjusted for each period to control the increases of the trigger rate due to the increase in the pileup. However, for E_T^{miss} above 200 GeV, The stable trigger efficiency is obtained for all periods.

7.3 Signal Region

In this section, we will discuss the details of SR. First, the variables used in selection are discussed, and then, the analysis flow to SR is explained.

7.3.1 Discrimination variables

In this section, the variables used in the selection are explained. Since the main component of the background is W+jet (the detail is discussed in section 8.1), the distribution of W+jet MC is used as background for comparison with the signal and background.

The distributions of E_T^{miss} and Track E_T^{miss} (see section 5.5) in Higgsino MC, W+jet MC and $t\bar{t}$ MC are shown in Figure7.4. In signal event, higher E_T^{miss} and higher Track E_T^{miss} are observed since the two $\tilde{\chi}_1^0$s carry away the energy.

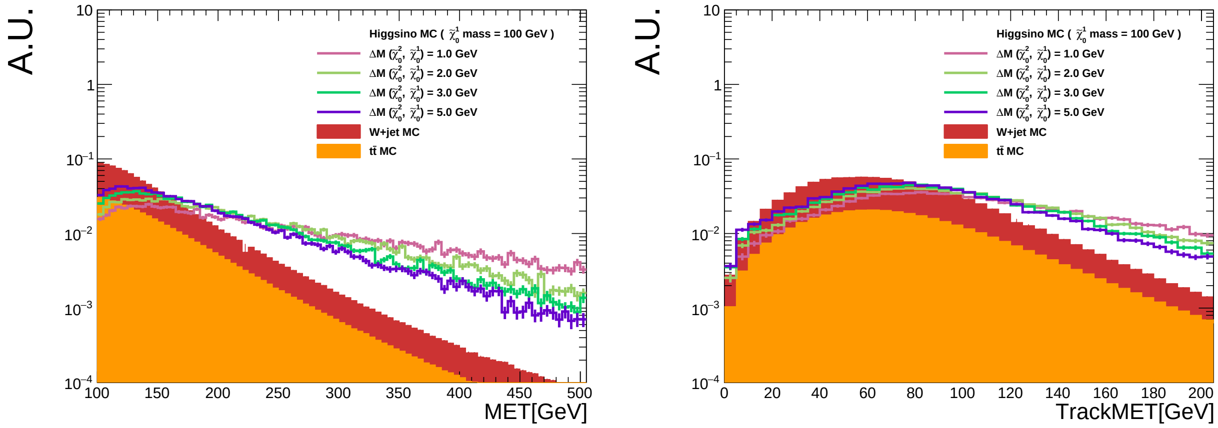

(a) (b)

Figure7.4 distributions of (a) E_T^{miss} and (b) Track E_T^{miss}. In signal, high E_T^{miss} is observed since $\tilde{\chi}_1^0$ carries away the energy.

leading jet p_T

The leading jet is the jet with the highest p_T in a event, and its p_T distribution is shown in Figure 7.5. In order to enforce that the center of mass system of SUSY particles is boosting, leading jet p_T > 100 GeV is required.

The number of b-jet

The distribution of the number of b-jets is shown in Figure 7.6. In this analysis, the number of b-jets is required to be 0 since there is no b-jet in the signal event. The top quark pair production event ($t\bar{t}$ event) can be a background because it can generate a large E_T^{miss}, but $t\bar{t}$ event can be suppressed by requiring the number of b-jet=0 since $t\bar{t}$ event always has two b-jets.

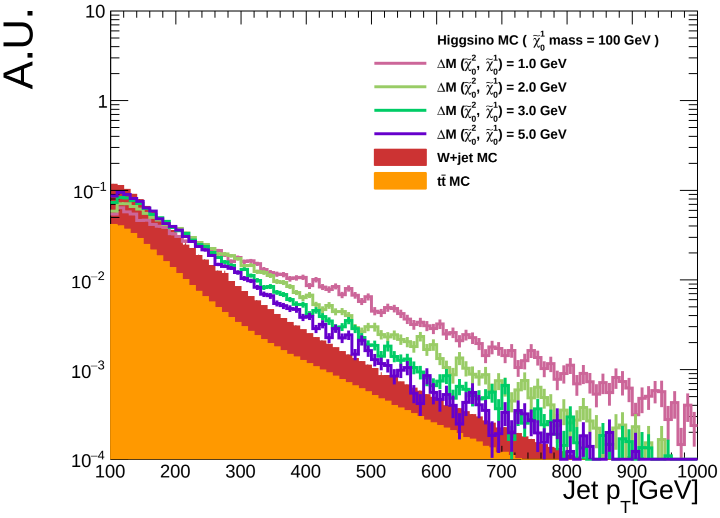

Figure7.5 distribution of leading jet p_T. High p_T of the leading jet is necessary to enforce ISR topology.

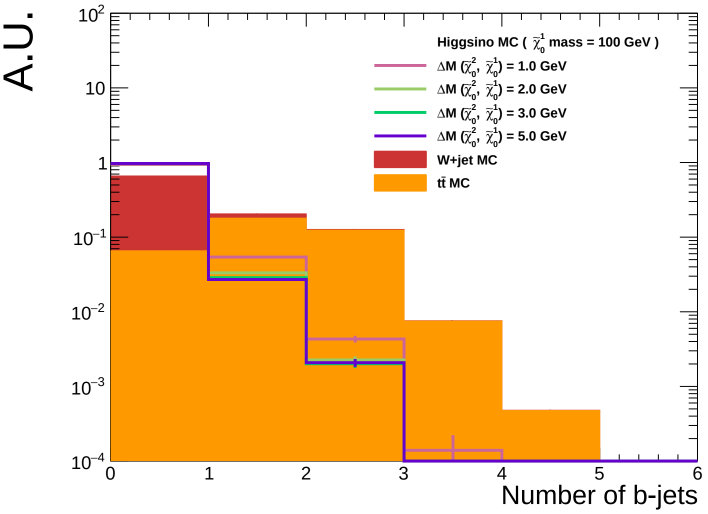

Figure7.6 distribution of the number of b-jets. Since there is no b-jet in the signal, the number is 0 in most of the events.

$\Delta\phi(\boldsymbol{p}_T^{miss}, \mathbf{Z}^*)$

For $\Delta\phi(\boldsymbol{p}_T^{miss}, Z^*) < 0.1$ is required. The definition of $\Delta\phi(\boldsymbol{p}_T^{miss}, Z^*)$ is eq (7.1). where Z^* refer to off-shell Z boson.

$$\Delta\phi(\boldsymbol{p}_T^{miss}, Z^*) = \phi(\boldsymbol{p}_T^{miss}) - \phi(Z^*) \tag{7.1}$$

where $\boldsymbol{p}_T^{miss}$ is the 3-dim. momentum of E_T^{miss} and $\phi(Z^*)$ is the Z^* momentum direction in ϕ.

In signal, $\Delta\phi(\boldsymbol{p}_T^{miss}, Z^*)$ is small since both E_T^{miss} and $\phi(Z^*)$ are originated from SUSY particles boosted by the ISR jet.

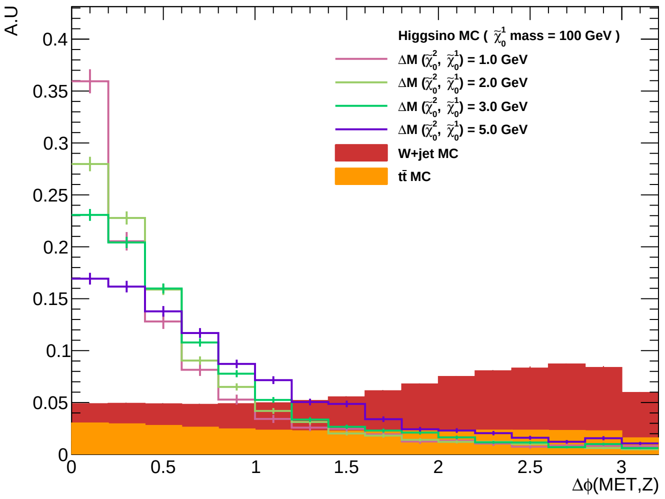

Figure7.7 distribution of $\boldsymbol{\Delta\phi(p_T^{miss}, Z^*)}$. Since the SUSY system is boosting, $\boldsymbol{p}_T^{miss}$ and Z^* are close.

off-shell Z boson mass

off-shell Z boson mass < 5 GeV is required since $\Delta m(\tilde{\chi}_2^0, \tilde{\chi}_1^0)$ of the target scenarios are less than 5 GeV. Figure 7.8 shows the distribution of the off-shell Z boson mass. The value is concentrated at small values since the maximum value of the off-shell Z boson mass is $\Delta m(\tilde{\chi}_2^0, \tilde{\chi}_1^0)$ due to energy conservation. Therefore, the distribution of the off-shell Z boson mass varies greatly in each $\Delta m(\tilde{\chi}_2^0, \tilde{\chi}_1^0)$ scenario.

$\boldsymbol{\Delta R_{muon,trk}}$

$\Delta R_{muon,trk} < 1.5$. is required.The definition of $\Delta R_{muon,trk}$ is eq (7.2). Figure 7.9 shows the distribution of $\Delta R_{muon,trk}$. The value of $\Delta R_{muon,trk}$ concentrates at small values, and the smaller $\Delta m(\tilde{\chi}_2^0, \tilde{\chi}_1^0)$ senario has the smaller the value of $\Delta R_{muon,trk}$. This is because off-shell Z boson with the lighter mass can be strongly boosted, and the distribution of the off-shell Z boson mass depends on $\Delta m(\tilde{\chi}_2^0, \tilde{\chi}_1^0)$. $\Delta R_{muon,trk}$ should be less than 1.5 in the region where $\Delta m(\tilde{\chi}_2^0, \tilde{\chi}_1^0)$ is smaller than 5 GeV.

$$\Delta R_{muon,trk} = \sqrt{(\eta_{muon} - \eta_{trk})^2 + (\phi_{muon} - \phi_{trk})^2} \tag{7.2}$$

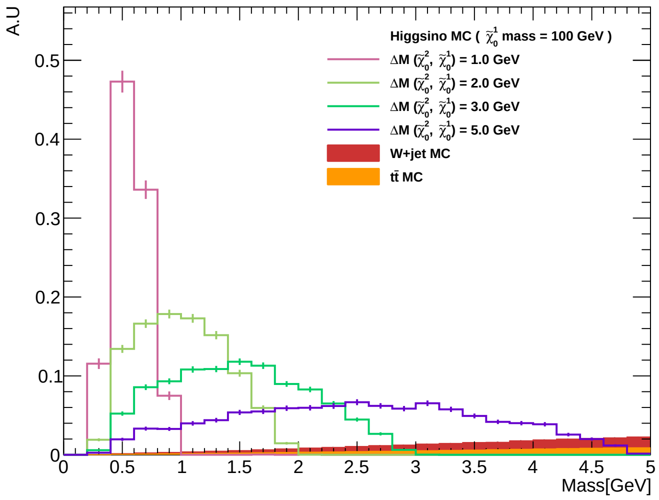

Figure7.8 Since the maximum value of the off-shell z boson mass is limited by the value of $\Delta m(\tilde{\chi}_2^0, \tilde{\chi}_1^0)$, the distribution differs depending on the scenario.

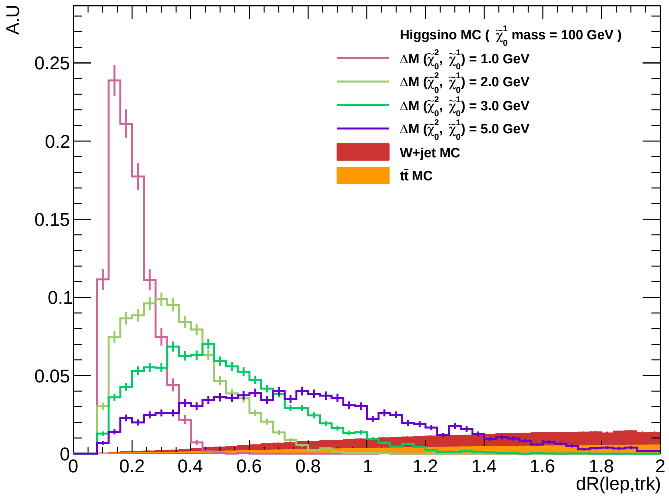

Figure7.9 distribution of $\Delta R_{muon,trk}$. The angle ($\Delta R_{muon,trk}$) between muons is smaller since off-shell z boson are boosted.

$|\Delta z0_{muon,trk}|$ and $|\Delta d0_{muon,trk}|$

For $z0$, $|\Delta z0_{muon,trk}| < 0.26$ is required. For $d0$, $|\Delta d0_{muon,trk}| < 0.10$ is required. The definitions are given in eq. (7.3) and eq. (7.4), respectively. The distributions of $|\Delta z0_{muon,trk}|$ and $|\Delta d0_{muon,trk}|$ are shown in Figure 7.10.

$$|\Delta z0_{muon,trk}| = |z0_{muon} - z0_{trk}| \tag{7.3}$$

$$|\Delta d0_{muon,trk}| = |d0_{muon} - d0_{trk}| \tag{7.4}$$

where z0 and d0 are the values concerning the vertex (defined in section 5.1). The $z0$ and $d0$ values of muon and track should be close since muon and track come from the same off-shell Z boson decay.

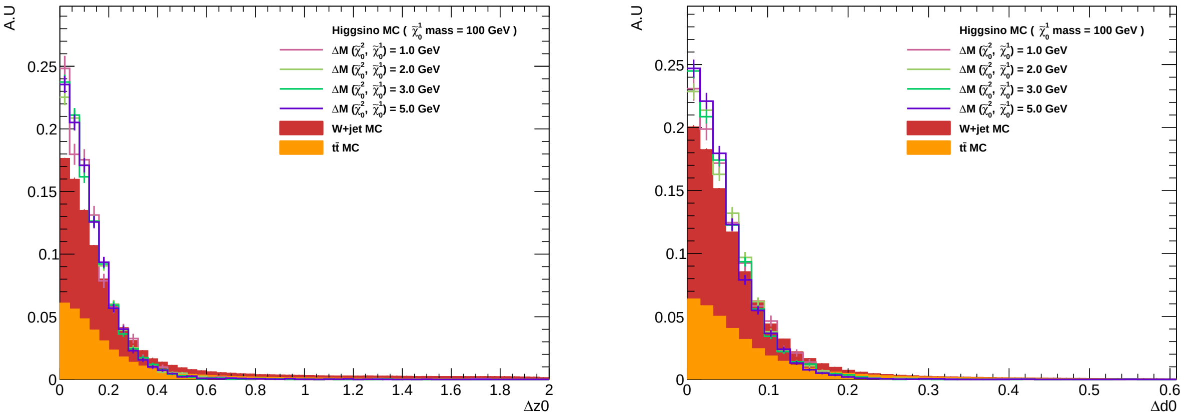

(a) (b)

Figure7.10 distributions of (a) $\Delta z0_{muon,trk}$ and (b) $\Delta d0_{muon,trk}$. Muon and track are originated from the same off-shell z boson. Thus, These vertexes should be close.

7.3.2 parameterized Neural Network

The score of the DNN that trained to efficiently discriminate between signal and background is introduced.

However, there are some variables (e.g. off-shell Z boson mass and $\Delta R_{muon,trk}$) that the distribution greatly depends on the $\Delta m(\tilde{\chi}^0_2, \tilde{\chi}^0_1)$. Therefore, it is difficult to create a DNN with high performance for all scenarios. A possible solution is to prepare one DNN by using MC events for each scenario. But, this requires preparing a large number of MC samples for signal events. However, it is not practical because it uses a large amount of computer resources and CPU time to produce the signal MC sample.

To solve this problem, we use a parameterized neural network referred to as pNN[61]. Figure 7.11 shows schematic diagram of pNN. pNN is one of DNN that use not only the measured variables (x_1, x_2) but also physics parameter (θ). Hereafter, $\Delta m(\tilde{\chi}^0_2, \tilde{\chi}^0_1)$ is chosen as the physics parameter pNN-θ. pNN can smoothly interpolate between the $\Delta m(\tilde{\chi}^0_2, \tilde{\chi}^0_1)$ used for training, allowing us to explore various scenarios with high efficiency using the limited number of samples.

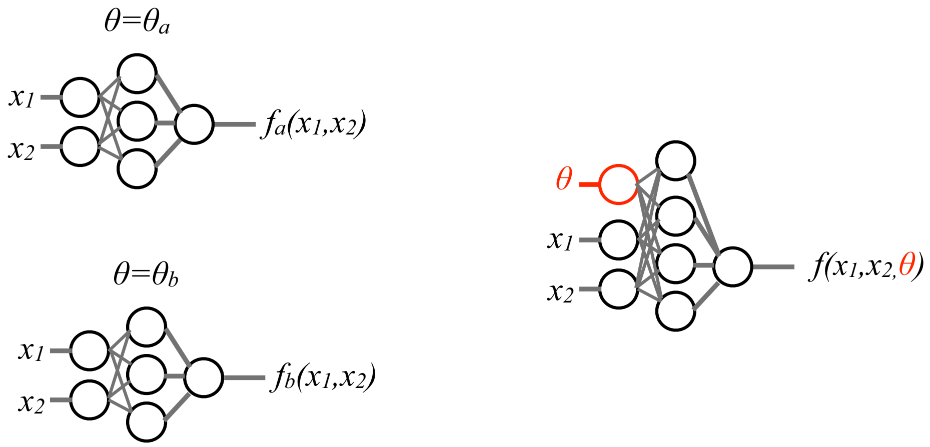

Figure7.11 schematic diagram of pNN. A DNN is needed for each scenario with conventional DNNs, which use only measure variables (left). By adding the physics parameter to the input, all scenarios can be learned simultaneously, and the efficiency is increased.(right)[61]

The input variables are summarized in Table7.1.As signal samples, Higgsino MC with $\Delta m(\tilde{\chi}^0_2, \tilde{\chi}^0_1) = (1, 1.5, 2, 3, 5)$ GeV are used to pNN training and test. In addition, W+jet MC and SS data are used as background sample. Here, SS data means a data sample with a same sign (SS) muon pair instead of an opposite sign (OS) pair for a Z* candidate. SS data has similar distribution to those of background events in OS data (the detail is discussed in 8.1 later). The pNN-θ for the background samples is given randomly so that the distribution is the same as the distribution of the Higgsino MC.In addition, only events that pass baseline selection (described section 7.3.3) are used.

Figure 7.12 shows the distribution of pNN scores for each scenario. We can see that there is no overtraining and good separation between signal and background.

7.3.3 Analysis Flow

Figure 7.13 shows the flow of the analysis. The detail of each section is described below.

Table7.1 Summary of inputs of the pNN.

input variable	description
$\Delta m(\tilde{\chi}_2^0, \tilde{\chi}_1^0)$	pNN-θ, mass difference between $\tilde{\chi}_2^0$ and $\tilde{\chi}_1^0$
muon η	signal muon kinematics
muon ϕ	
muon p_T	
track η	signal track kinematics
track ϕ	
track p_T	
E_T^{miss}	E_T^{miss} kinematics
ϕ of p_T^{miss}	
leading jet p_T	leading jet kinematics
ϕ of leading jet momentum	
$\Delta\phi(\boldsymbol{p_T^{miss}}, Z^*)$	ϕ angle between objects
$\Delta\phi(leading\,jet, Z^*)$	
off-shell z boson mass	off-shell z boson variables
$\Delta R_{muon,trk}$	
scalar sum of muon p_T and track p_T	

Baseline Selection

First, baseline selection is applied to signal region and validation regions for background estimation (discussed in section 8.2 later). In order to select events highly boosted by ISR jet, at leaset one high p_T jet is required and the highest p_T jet is supposed as the ISR jet. The event is required a high p_T jet to enforce ISR topology, and the highestp_T jet is the ISR jet. Also, to enforce the High E_T^{miss} topology, $E_T^{miss} > 200$ GeV is required.

In addition, high E_T^{miss} ($>$ 200 GeV) is required because of production of LSPs. This E_T^{miss} requirement is important to ensure the stable trigger efficiency, too. For the signal muon, p_T $<$ 10 GeV is required since low p_T is dominant. Furthermore, no b-jet is required to suppress backgrounds from top-quark production. Table 7.2 summarizes the baseline selection.

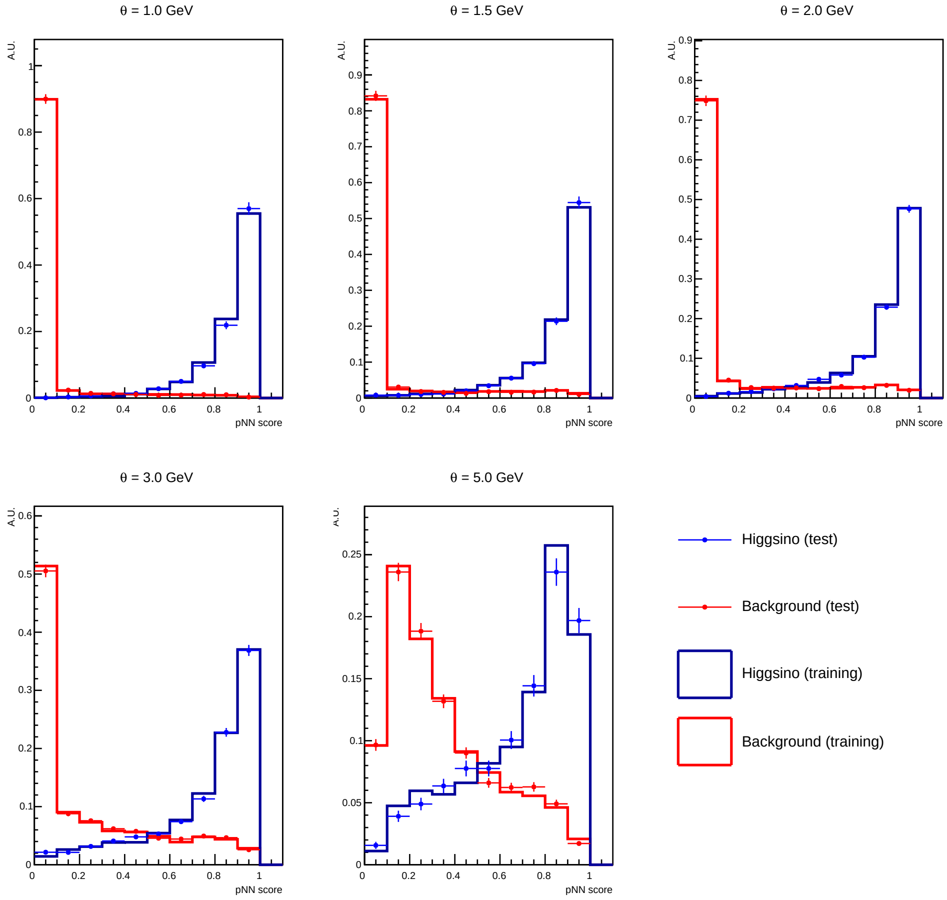

Figure7.12 pNN score distribution in each pNN-θ.The blue dots and the red dots are the distribution of the test sample of Higgsino MC and the background, respectively. Also, The blue histogram and the red histogram are the distribution of the training sample of Higgsino MC and the background, respectively. There are no large differences between the test and the training samples.

Table7.2 Summary of baseline selection

Variable	selection criteria
E_T^{miss}	$\geq$ 100 GeV
Track E_T^{miss}	$\geq$ 50 GeV
Leading jet p_T	$\geq$ 100 GeV
Number of muons with standard muon ID	= 1
p_T of muon with standard muon ID	$\leq$ 10 GeV
Number of b-tagged jets	= 0

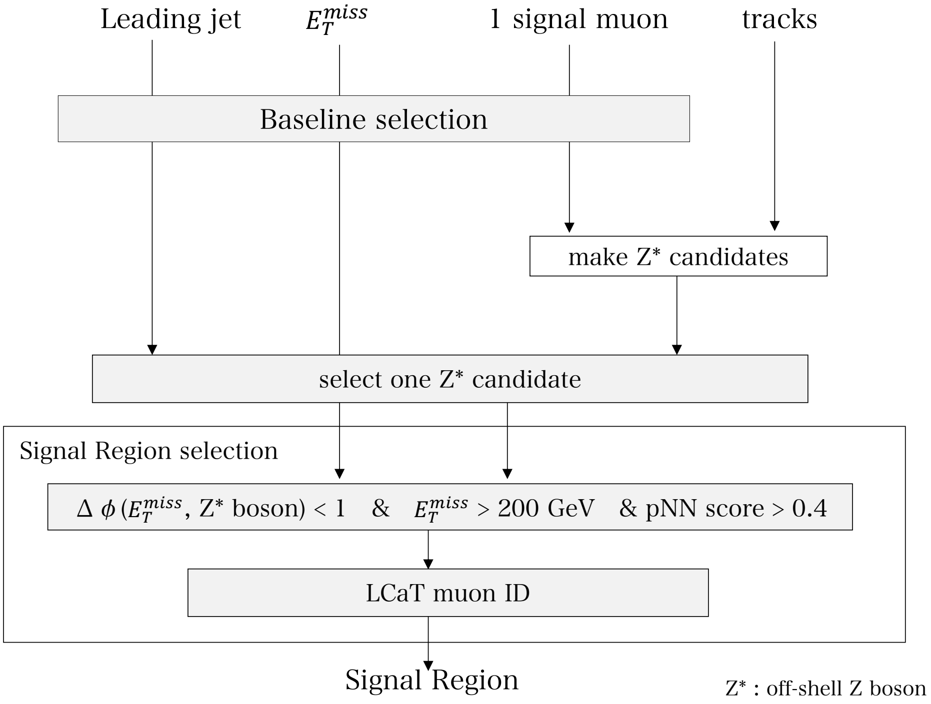

Figure7.13 Diagram of analysis flow

select one Z^* candidate

In '*make* Z^* *boson candidates*' section in figure 7.13, Z^* candidates are reconstructed with all signal muon and track combinations. Then, only one candidate, which is the most signal like Z^* candidate, is selected in '*select one* Z^* *candidate*' section. Table 7.3 shows selection which Z^* candidate should satisfy. If multiple candidates remain, the candidate with the highest pNN score is selected.

Table7.3 Summary of off-shell Z boson selection

Variable	selection criteria
Charge	opposit sign
$\Delta R_{muon,trk}$	[0.1, 1.4]
$m_{lep,trk}$	≤ 5 GeV
$\Delta z0_{muon,trk}$	≤ 0.26
$\Delta d0_{muon,trk}$	≤ 0.10
J/ψ veto	$m_{muon,trk} < 3GeV$ or $m_{muon,trk} > 3.2GeV$

Signal Region selection

Table7.4 shows signal region selection. The selection is applied to the event in which Z^* candidate is chosen.

Table7.4 Summary of signal region selection

Variable	selection criteria
E_T^{miss}	$\geq$ 200 GeV
$\Delta\phi$(Z*, p_T^{miss})	$\leq$ 1 rad
pNN score	$\geq$ 0.4
LCaT muon ID for track	*Higgsino WP*

Check for the presence or absence of a signal using an event that satisfies all of the above selections.

Final discrimination variable

In order to examine the presence of signal, the shape of the distribution of a variable called as final discrimination variable are used. Its distribution should have maximum discrimination power signal from the backgrounds. Therefore, the pNN score is chosen as the final discrimination variable since the pNN is trained to efficiently discriminate between signal and background. In order to evaluate the SUSY scenario using the shape information of the pNN score, we divide the SR by the pNN score. The detail is discussed in 10.2. Table 7.5 shows the list of SR.

Table7.5 List of SR

SR name	pNN score range
`SR-pNNScore-A`	[0.4, 0.5]
`SR-pNNScore-B`	[0.5, 0.6]
`SR-pNNScore-C`	[0.6, 0.7]
`SR-pNNScore-D`	[0.7, 0.8]
`SR-pNNScore-E`	[0.8, 0.9]
`SR-pNNScore-F`	[0.9, 1.0]

8. Background estimation

In this section, the background estimation method and expected amount of background are described. First, sources of background events are explained, second, a new method for estimation of the background contamination is discussed. It is dedicated for this analysis.

8.1 Background component

The main component of the background is a combination of muon and hadron/fake track. Uncorrelated two tracks accidentally imitate muon pairs from off-shell Z boson. The number of background events with two true muons is assumed to be small enough as discussed in section 8.4. In addition, these background events tend to have neutrinos which make the high E_T^{miss}. Thus, an event that has one muon and neutrinos can be the background. For these reasons, the W + jet event in which W boson decays leptonically (Figure 8.1) is the main background. In this case, the hadron track is a particle originated from the same vertex, but is not drawn in the Feynman diagram of Figure 8.1.

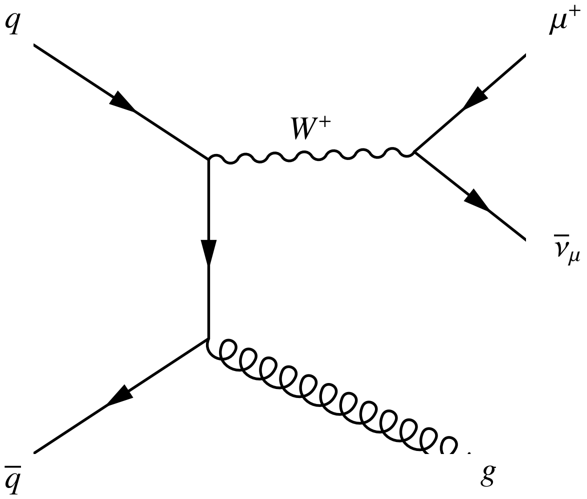

Figure8.1 Feynman diagram of W+jet

For the invariant mass of a lepton and a track,$m_{lep,trk}$, > 2 GeV region, it is expected that distributions in the same sign (SS) data are almost the same with the opposite sign (OS)[9] since muon and hadron/fake track combination is an accidental one. The distribution is similar to part of the background in OS data. Therefore, SS data is useful for training of pNN (section 7.3.2). However, background estimation using SS data is problematic since the OS data has more background than the SS data in $m_{lep,trk} < 2$GeV due to low-mass resonances.

In this study, we have developed a background estimation method that takes advantage that the di-muon background is sufficiently small and the main background track component is hadron and fake track.

8.2 Definition of Validation region

Before explaining the background estimation method, we define the Validation Region to evaluate the method of background estimation. As shown in Figure 8.2, four Validation Regions are defined to surround the SR which is defined in Table 7.4. The three Validation Regions are the Low E_T^{miss} or/and Large $\Delta\phi(Z^*, p_T^{miss})$ regions compared to SR. Low E_T^{miss} and Large $\Delta\phi$ region, Low E_T^{miss} and Small $\Delta\phi$ region, high E_T^{miss} and Large $\Delta\phi$ regions are referred to as `VR_LowLarge`, `VR_LowSmall`, and `VR_HighLarge`, respectively. Also, in the High E_T^{miss} and small $\Delta\phi$ region, the region with Low pNN score is used as a Validation Region because of the small signal contamination. The region is referred to as `VR_LowpNN`.

8.3 LCaT muon weight method

This section describes how to estimate the distribution of the final discrimination variable(pNN score). The general background estimation is done using MC simulations. However, a large difference between data and MC simulation was observed in the region where the track p_T is small. In particular, a large difference was observed in the number of fake tracks, which is difficult to simulate. To avoid this problem, we develop a new method to estimate all backgrounds from the pp collision data. Figure 8.4 shows a schematic diagram of the method.

First, for simplicity, the shape of the pNN score distribution is ignored. Figure 8.3 shows the overview of the background estimation method. It is referred to as *LCaT muon weight method*. In the method, events with Anti-LCaT muon ID are used to estimate the amount of background. Anti-LCaT muon ID means track does not satisfy the LCaT muon ID. The LCaT muon ID efficiency for events that satisfy all selections except the LCaT muon ID is referred to as ε_{LCaT}, and the LCaT muon ID efficiency for the background is referred to as ε_{LCaT}^{bkg}. Thus, $\varepsilon_{LCaT} = \varepsilon_{LCaT}^{bkg}$ if signal

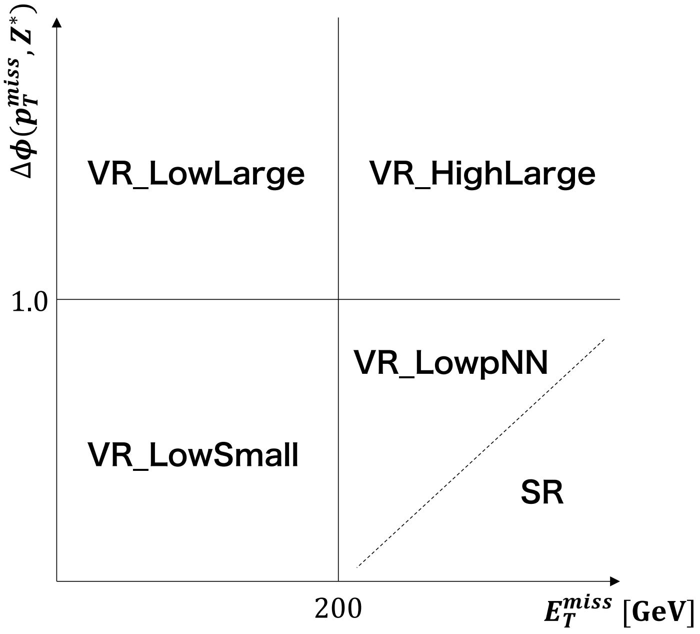

Figure8.2 Definition of Validation Region. Each VR is delimited by E_T^{miss} and $\Delta\phi$. In the region of high E_T^{miss} and small $\Delta\phi$, the region with a small pNN score is defined as VR.

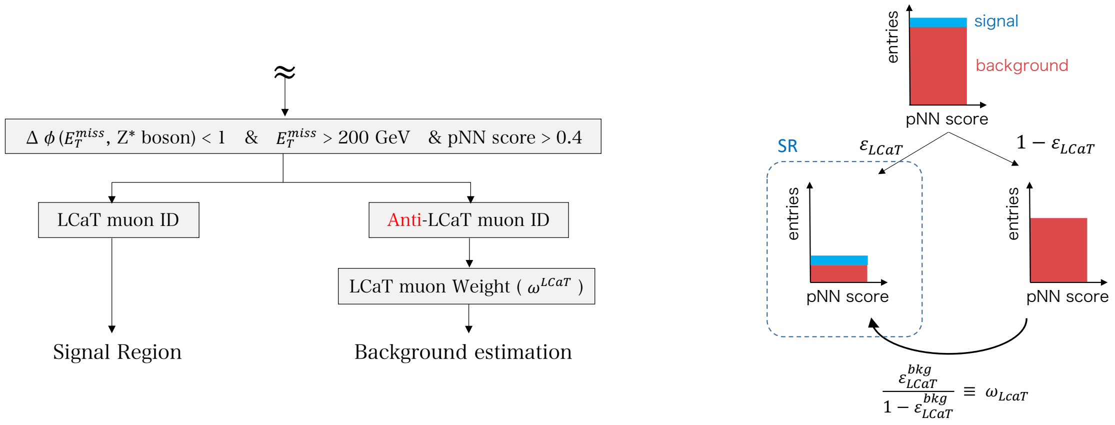

Figure8.3 Overview of the LCaT muon weight method. In the SR, events are cut by requesting the LCaT muon ID. The distribution of the pNN scores is determined by the distribution and correlation of the pNN input variables in the remaining events. In the background estimation, the original input data is normalized to have the same distribution as when LCaT muon ID is applied. By emulating the distribution of input data, it is possible to estimate the distribution of the pNN score.

does not exist. $1 - \varepsilon^{bkg}_{LCaT}$ of background are Anti-LCaT muon ID, therefore, multipled events with Anti-LCaT muon ID by $\varepsilon^{bkg}_{LCaT}/(1 - \varepsilon^{bkg}_{LCaT})$ should be the same with the amount of background in SR. Hereafter, $\varepsilon^{bkg}_{LCaT}/(1 - \varepsilon^{bkg}_{LCaT})$ is referred to as the LCaT muon weight ($\omega_L CaT$).

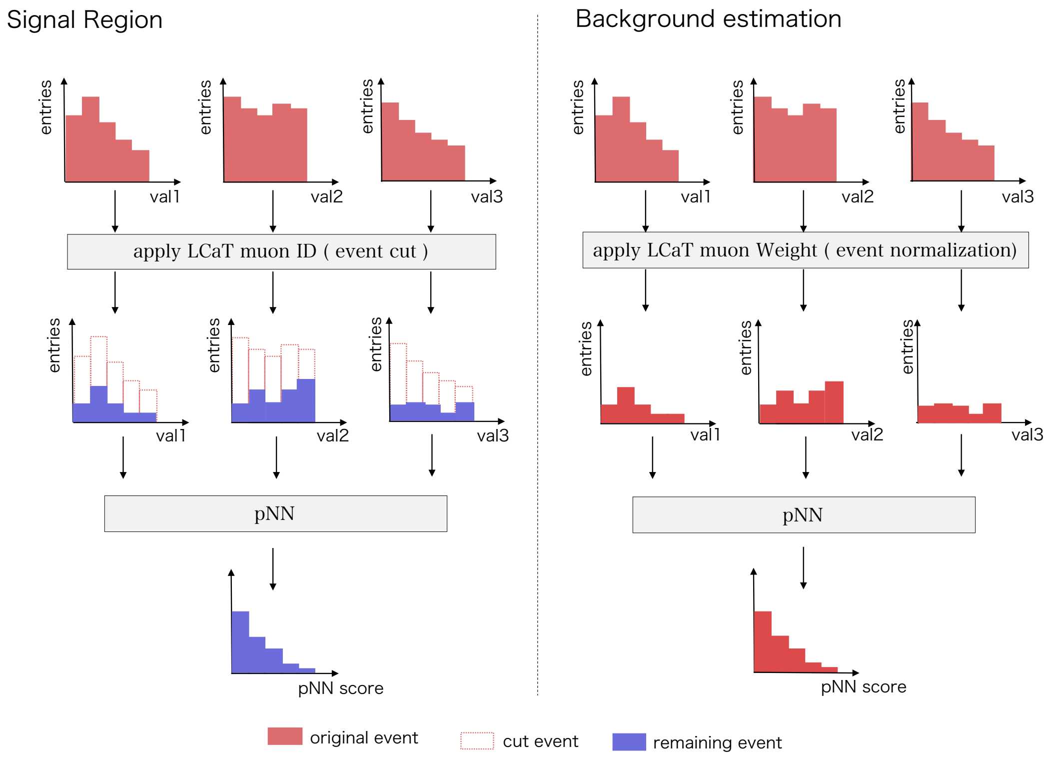

Figure8.4 Schematic diagram of the LCaT muon weight method. In the SR, events are cut by requesting the LCaT muon ID. The distribution of the pNN scores is determined by the distribution and correlation of the pNN input variables in the remaining events. In the background estimation, the original input data is normalized to have the same distribution as when LCaT muon ID is applied. By emulating the distribution of input data, it is possible to estimate the distribution of the pNN score.

Next, shape information of pNN score distribution is discussed. In principle, the shape of the pNN score distribution is determined by the input variables and their correlations. In SR, the distributions of input data changes by requesting the LCaT muon ID(Figure 8.4 left. The red is a distribution before the LCaT muon ID. It changes to blue distributions by requesting the LCaT muon ID. The blue distribution determines the pNN score distribution.). Therefore, estimating the shape of the pNN score distribution is equivalent estimating the shape of the input data distribution. Thus, in *LCaT muon weight method*, LCaT muon weight is defined to model the LCaT Muon ID response and apply the weight event by event. In other words, the LCaT muon weight is defined as a function of variables related to the LCaT muon ID efficiency.

component of the LCaT muon ID efficiency

To emulate the LCaT muon ID efficiency, we summarize its components in eq.(8.1).

$$\begin{aligned} \varepsilon_{LCaT} =& \varepsilon^{other}_{LCaT}(track\,\eta, track\,p_T) \times R^{other}_{LCaT}(\Delta R_{muon,trk}, E_T^{miss}) \\ &+ \varepsilon^{muon}_{LCaT}(track\,\eta, track\,p_T) \times R^{muon}_{LCaT}(\Delta R_{muon,trk}, E_T^{miss}) \end{aligned} \tag{8.1}$$

The efficiency of the LCaT muon ID (ε_{LCaT}) depends on track eta, track pT, $\Delta R_{muon,trk}$, and E_T^{miss}. where R^{muon}_{LCaT} means the ratio of di-muon background, but R^{muon}_{LCaT} is assumed to be small enough (discussed in section 8.4). Also, R^{other}_{LCaT} is ratio of tracks except muon in all background track. $\varepsilon^{muon}_{LCaT}$ and $\varepsilon^{other}_{LCaT}$ is LCaT muon ID efficiency for muon track and background tracks except muon,respectively. From eq.(8.1), the LCaT muon weight (ω_{LCaT}) is needed to be also defined as a function of track eta, track pT, $\Delta R_{muon,trk}$, and E_T^{miss}.

How to make the LCaT muon weight

This paragraph describes how to make the LCaT muon weight. To calculate the LCaT muon weight, it is necessary to predict ε^{bkg}_{LCaT}. Therefore, LCaT muon estimator ($\varepsilon^{emuBkg}_{LCaT}$) ,which is defined as to output the ε^{bkg}_{LCaT}, is needed. To examine the efficiency of LCaT muon ID for the background only in SR, it is necessary to use a region that has the same background component as SR without the signal.

For the SR, muon identified by standard muon ID and track with LCaT muon ID, which refer to as Same Flavor(SF), are required. Against SF, Different Flavor (DF) is used to predict the LCaT muon ID efficiency. DF means electron identified standard electron ID (see section 5.4) and track with LCaT muon ID are required. the LCaT muon ID efficiency for the background only can be observed since DF does not contain the signal. In addition, the component of the track in the background is hadron or fake track. Therefor, the background component is almost the same between DF and SF.

For these reasons, It is assumed that the LCaT muon ID efficiency in SF(ε^{SF}_{LCaT}) and DF(ε^{DF}_{LCaT}) are the same to create the LCaT muon weight.

8.4 $\varepsilon^{SF}_{LCaT} = \varepsilon^{DF}_{LCaT}$ hypothesis test

In this section, the hypothesis that $\varepsilon^{SF}_{LCaT} = \varepsilon^{DF}_{LCaT}$ in SR is confirmed using VR. Figure 8.5 shows the dependence of the LCaT muon ID efficiency on E_T^{miss}, track η, track p_T, and $\Delta R_{muon,trk}$ in SF and DF. The blue and the red lines show the efficiency in SF and DF, respectively. If there is large number of di-muon background, some difference between SF and DF must be found. As a result, there is a good agreement between SF and DF in all regions. We conclude that the LCaT ID efficiency is consistent between SF and DF in SR based on the results, and the di-muon background is sufficiently small. Also, the difference between SF and DF is discussed in section 9.4.

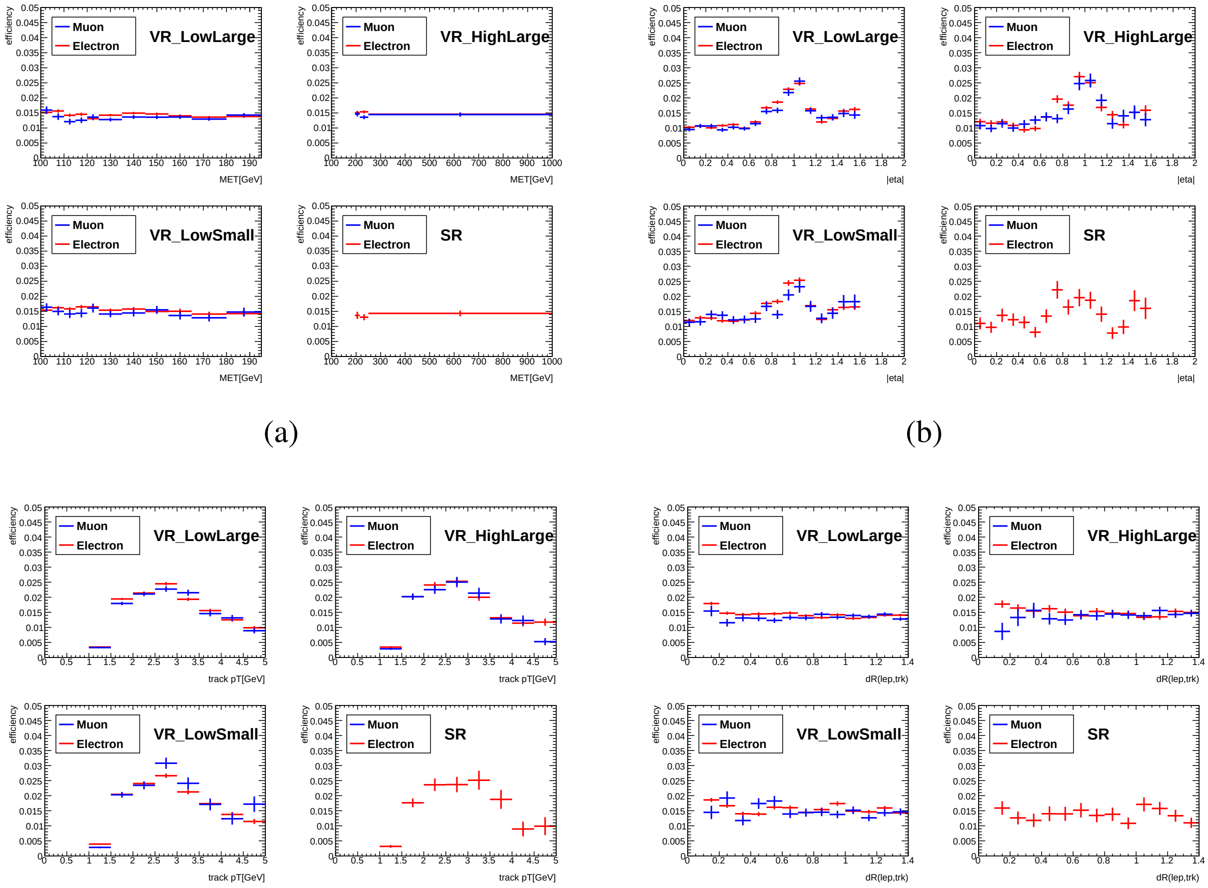

(a) (b)

(c) (d)

Figure8.5 E_T^{miss}, track η, track p_T, and $\Delta R(lep,trk)$ dependence of ε^{SF}_{LCaT} and ε^{DF}_{LCaT}.It can be confirmed that ε^{SF}_{LCaT} and ε^{DF}_{LCaT} are consistent for each variable and each VR. Also, the VR dependence of ε_{LCaT} is small. (a) E_T^{miss} (b) track η (c) track p_T (d) $\Delta R(lep,trk)$

8.5 Definition of the LCaT muon weight and LCaT muon estimator

structure of the LCaT muon weight and LCaT muon estimator

LCaT muon weight is created using the DF region to avoid signal contamination. To accurately estimate the distribution of pNN, it is necessary to emulate the dependence of LCaT muon ID efficiency on each variable, including the correlation between these variables. Figure 8.6 shows the efficiency of LCaT muon ID efficiency in the E_T^{miss}-track η plane and track p_T-ΔR plane. Other planes are shown in Appendix **??**.

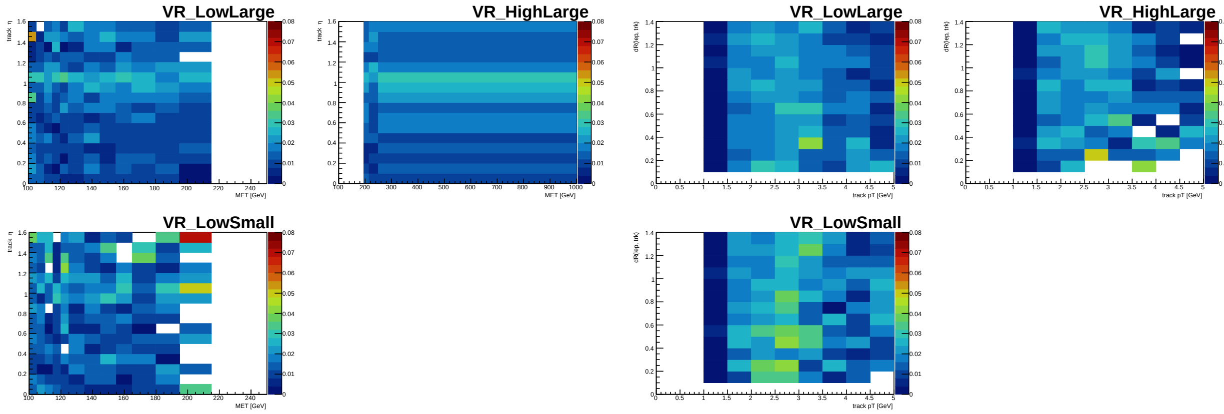

(a) (b)

Figure8.6 the efficiency of LCaT muon ID efficiency in the (a) E_T^{miss}-track η plane and (b) track p_T-ΔR plane.a strong correlation between each variable is not found.

From the results of each plane, no other strong correlation between variables is found in LCaT muon efficiency. Therefore, the dependency of LCaT muon ID efficiency on each variable can be written independently. Therefore, the LCaT muon weight is defined as eq.(8.3) using LCaT muon estimator (eq.(8.2)).

$$\epsilon_{LCaT}^{estiBkg} = \varepsilon_{LCaT}^{DF} \times \omega^{p_T}(track\ p_T) \times \omega^{\Delta R}(\Delta R_{muon,trk}) \times \omega^{\eta}(track\ \eta) \times \omega^{E_T^{miss}}(E_T^{miss}) \tag{8.2}$$

$$\omega_{LCaT} = \frac{\epsilon_{LCaT}^{emuBkg}}{1 - \epsilon_{LCaT}^{emuBkg}} \tag{8.3}$$

$\omega^{variable}$ represents the specific variable dependence in LCaT muon ID efficiency, and it is normalized so that ε_{LCaT}^{DF} is one. It means $\omega^{variable}$ is written as eq.(8.4).

$$\omega^{variable}(variable) = \frac{\varepsilon^{variable}(variable)}{\varepsilon_{LCaT}^{DF}} \tag{8.4}$$

detail of created LCaT muon estimator

The detail of the LCaT muon estimator created using the DF region is described in this section. Since tight selection is applied to SR, the number of events is very small. On the other hand, it can be confirmed that the region dependence of the LCaT muon ID efficiency is small from Figure 8.5. Therefore, the events of VR needed to be included to avoid the effect of statistical fluctuation in creating the LCaT muon estimator. Figure 8.7 shows created $\omega^{p_T,\Delta R}$,$\omega^{\eta}(track\,\eta)$,$\omega^{E_T^{miss}}$. Each weight component of the LCaT muon estimator is smoothing by connecting the values of each bin with a straight line. Also, the ε^{DF}_{LCaT} is 1.48%, and the statistical error is less than 0.02%.

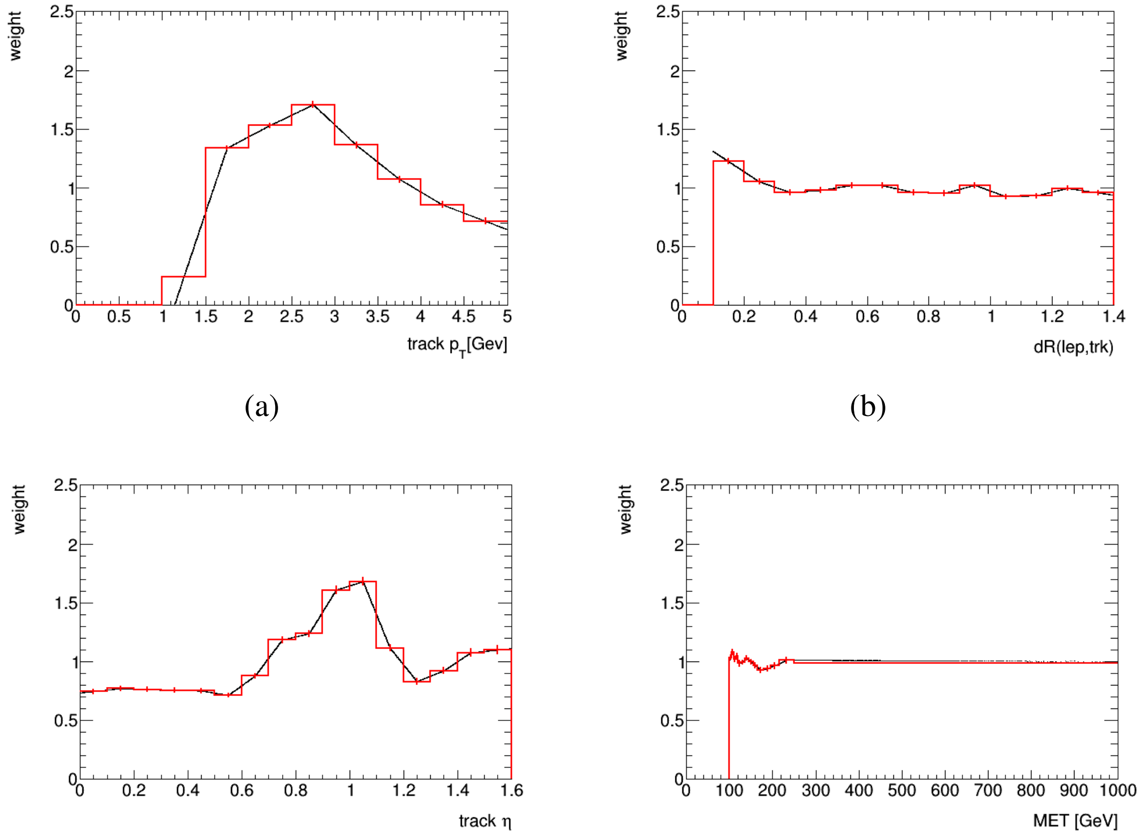

(a) (b)

(c) (d)

Figure8.7 black lines are (a)$\omega^{p_T,\Delta R}$, (b)$\omega^{\Delta R}$,(c) ω^{η},(d)$\omega^{E_T^{miss}}$ defined in eq.(8.3). All VRs and SRs in DF are used to create the weight to avoid statistical fluctuation.

8.6 Comparison between data and background estimation in VRs

In this section, validation of the LCaT muon weight method is discussed. Figure 8.8 shows the background estimation using the LCaT muon weight method and the data using the LCaT muon ID. SR and the regions with large signal contamination to data are blinded. Concretely, the region with pNN score > 0.7 of `VR_LowSmall` and the region with pNN score < 0.2 of `VR_LowpNN` are blinded. Good agreement between the background estimation and data was confirmed in the pNN score distribution for most VRs. The difference is within about 20 %. From these results, we conclude that the LCaT muon weight method can correctly estimate the number and distribution of pNN scores in SR. A detailed discussion of systematic errors is given in the section 9.4.

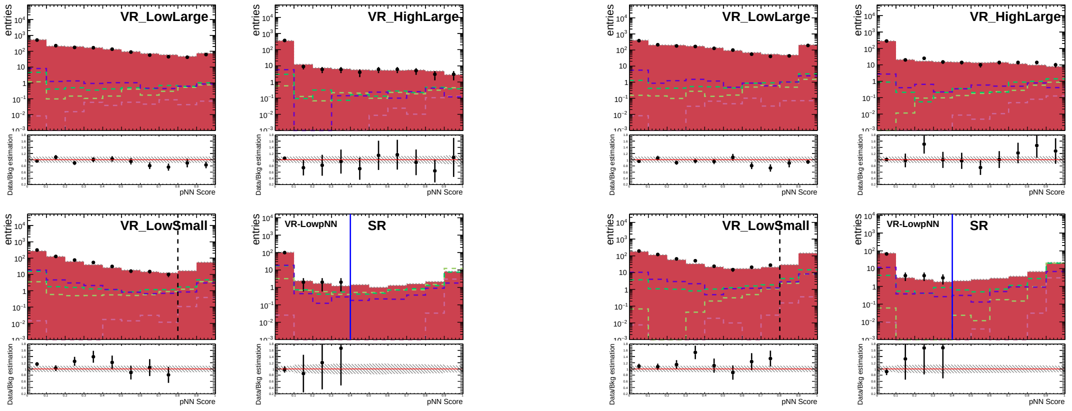

(a) pNN-θ = 1 GeV (b) pNN-θ = 2 GeV

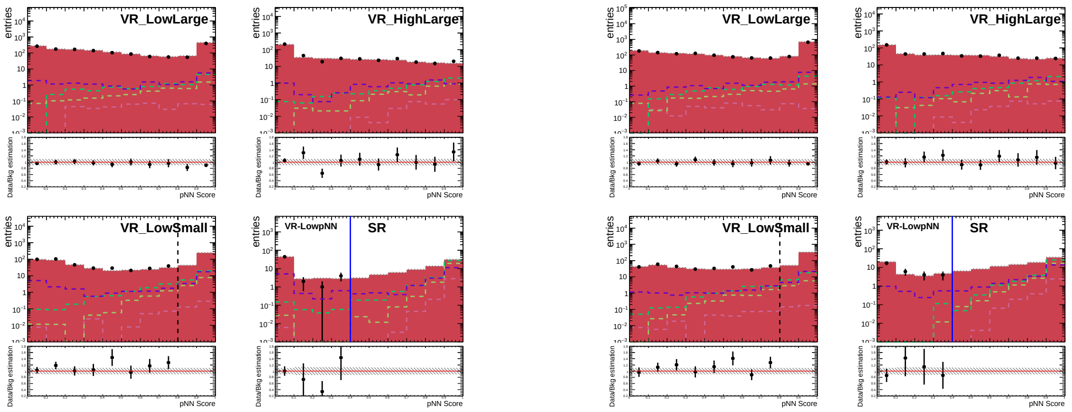

(c) pNN-θ = 3 GeV (d) pNN-θ = 4 GeV

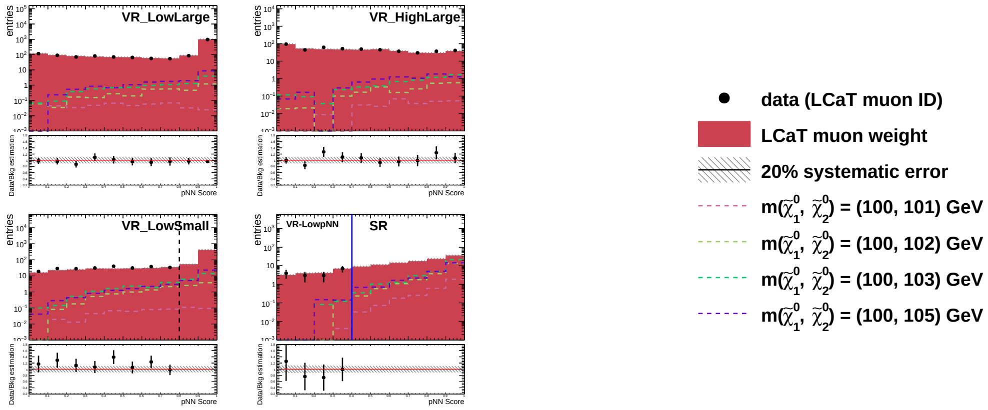

(e) pNN-θ = 5 GeV

Figure8.8 The result of background estimation. The dark red histogram is the distribution of the background estimated by the LCaT muon weight method, and the black dots are the results of the data obtained by applying the LCaT muon ID. Good agreement between background estimation and data is observed, and the difference is within about 20%.

9. Systematic Uncertainties

In this chapter, systematic uncertainties are summarized. In this study, the signal event is evaluated using MC simulation, and the theoretical uncertainty and experimental uncertainty are considered in the event. The former is discussed in section 9.1 and the latter in section 9.2. In addition, efficiency for the newly developed LCaT muon is discussed in section 9.3.2.

Since the background is estimated by a data-driven method, uncertainty about differences between MC simulation and data don't need to be considered. However, since the difference between the LCaT muon ID and the LCaT muon estimator generate the systematic difference, the uncertainty is discussed in section 9.4.

9.1 Theoretical uncertainties

9.1.1 Parton distribution function

The theoretical uncertainty is the factor of the Parton distribution function. In this thesis, MMHT2014[62] and CT14PDF[63] are compared with the NNPDF[36], which is used as the nominal value in this search, and the difference is used as uncertainty. The magnitude is 15%.

9.1.2 ISR modeling

Uncertainty on the ISR modeling is estimated using the Z($\rightarrow \mu\mu$)+jets events generated using the same MG5_aMC@NLO configuration as the Higgsino samples. The muon four momenta are added to the E_T^{miss} to emulate the signal events, and uncertainties are derived from observed differences between data and simulation. As a result, 20% is applied as the ISR modeling uncertainty.

9.2 Experimental uncertainties

9.2.1 Luminosity

Luminosity was measured with the LUCID-2 detector[64], and an uncertainty of 1.7% is applied to the integrated luminosity.

9.2.2 Muons

Uncertainty about muon identification and momentum resolution is estimated by analysis using $Z \to \mu$ and $J/\psi \to \mu\mu$event. The systematic uncertainties are a few % for leptons with $p_T > 10$ GeV, and up to 10 % for lower p_T. (The detail can be found in Ref.[55]).

9.2.3 Jets

Jet uncertainty can be divided into Jet Energy Scale (JES) uncertainty on calibration and Jet Energy Resolution(JER) on energy resolution. The estimation results are briefly summarized below. For details of the evaluation method, see Ref.[52].

JES uncertainty

Figure 9.1 shows the p_T and η dependence of JES uncertainty. the uncertainty is large at low-p_T, about 5%, and becomes smaller as p_T increases. However, above 200 GeV, the uncertainty is largely due to poor statistics. For the η direction, the uncertainty is almost flat, and the average is 2%.

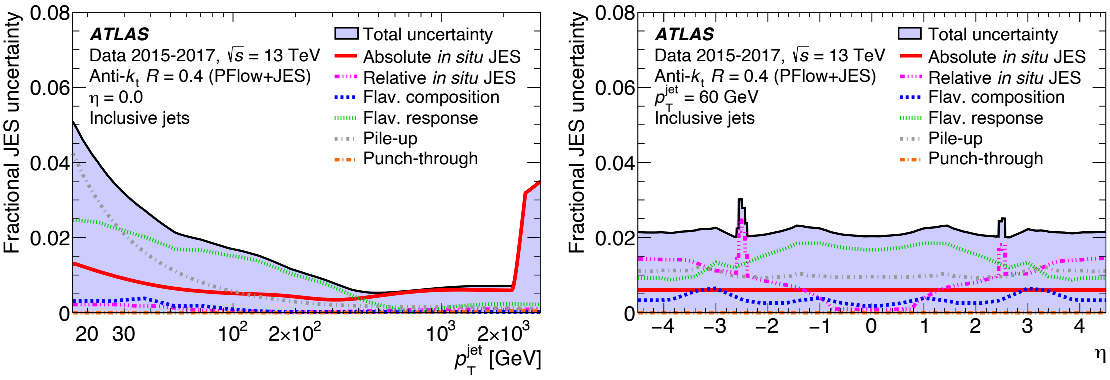

Figure9.1 Combined uncertainty in the JES of fully calibrated jets as a function of jet p_T at $\eta = 0$ (left), and η at $p_T = 60$ GeV (right)[52].

JER uncertainty

Fig.9.2 shows the total uncertainty on the relative JER as a function of jet p_T. The uncertainty takes maximum value at low-p_T, which is 1.5%.

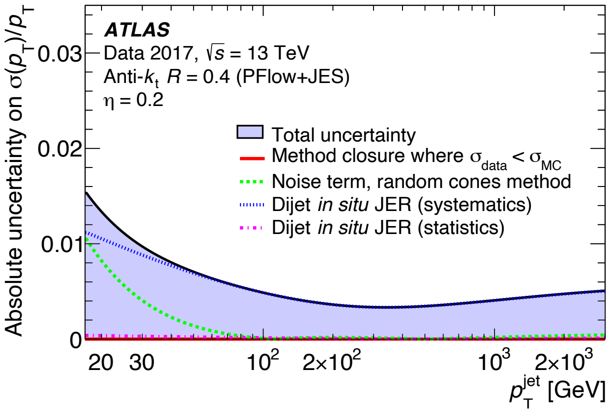

Figure9.2 Total uncertainty on the relative JER as a function of jet p_T[52].

9.2.4 missing E_T

The systematic uncertainty associated with modeling E_T^{miss} in the simulation is estimated by propagating the uncertainty at the energy and momentum scales of each object used in the calculation. Uncertainties in the resolution and scale of the soft term are modeled separately(the details is discussed in Ref[58]).

9.3 LCaT muon ID systematic uncertainty

This section describes the difference in the LCaT muon ID efficiency between data and MC. The tag and probe method using J/ψ decay is used for the evaluation. Also, we use the pp collision data obtained by the single muon trigger and the J/ψ MC sample. First, we describe the details of the tag and probe method and then summarize the results.

9.3.1 Tag and probe method

The acquired data is collected using triggers, in other words, event selection has already been applied by the trigger. It is obvious that the identification efficiency for the muon is high in offline analysis for events with the single muon trigger. The efficiency is overestimated for such muons. The tag and probe method prevents from such bias.

Figure 9.3 shows the analysis flow of the tag and probe method. First, a tag muon which is matched with the trigger is found. Next, The tag muon and one of other tracks with LCaT muon ID are combined, and the invariant mass is calculated. Resonance with a peak at 3.1 GeV can be seen in the invariant mass distribution. This resonance is originated from the J/ψ decayed into di-muon, therefore the track is considered as a muon. However, it is impossible to conclude because backgrounds remain around the peak. So, the probability of the muon from J/ψ decay is calculated by fitting the distribution. The invariant mass distribution is fitted using the gauss function as the J/ψ decay component and using the quadratic function as the background component. The number of J/ψ decay events is estimated by the integration of the gauss function. The same calculation is performed for the track with Anti-LCaT muon ID. Finally, the efficiency of the LCaT muon ID is calculated from the number of J/ψ decay events with LCaT muon ID and Anti-LCaT muon ID.

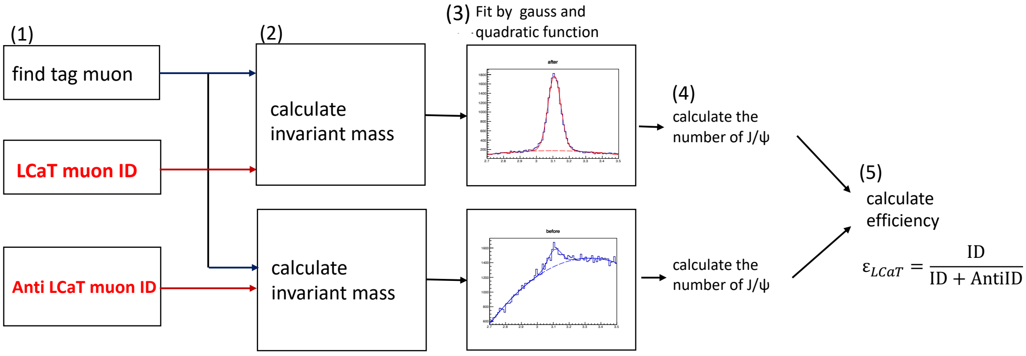

Figure9.3 Analysis flow of the tag and probe method. (1) find the tag muon matching the reconstructed muon in the trigger. (2) calculate the invariant mass using the tag muon and the track with LCaT muon ID/Anti-LCaT muon ID. (3)(4) estimate the number of J/ψ by fitting the invariant mass distribution. (5) calculate the efficiency from the number of J/ψ before and after applying the LCaT muon ID.

9.3.2 Evaluation of the LCaT muon efficiency

In each p_T and η region, this tag and probe method is performed to data and MC to compare the LCaT muon ID efficiency. Figure 9.4 and Figure 9.5 show the η dependence of the efficiency calculated by the tag and probe method. The track p_T is divided by 0.5 GeV steps except in 1 ~2 GeV region. For invariant mass fitting results, see appendix **??**. The difference between the data and J/ψ MC is about 10 ~20%. The systematic uncertainty of the LCaT muon ID efficiency is obtained by the direct sum of the statistical uncertainty of the efficiency calculated using data and the difference between data and J/ψ MC. In the range where the track pT is between 1 and 2 GeV, the small signal to background ratio results in relatively large statistical uncertainties.

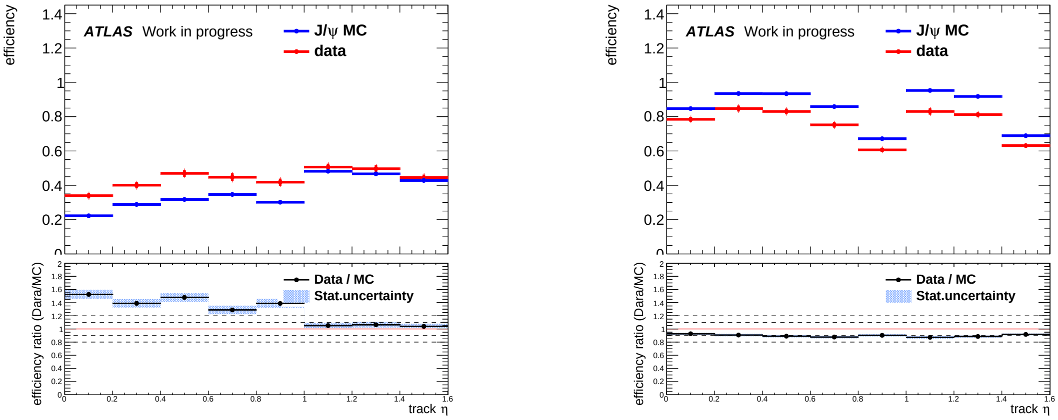

(a) 1.0 GeV < track p_T < 2.0 GeV

(b) 2.0 GeV < track p_T < 2.5 GeV

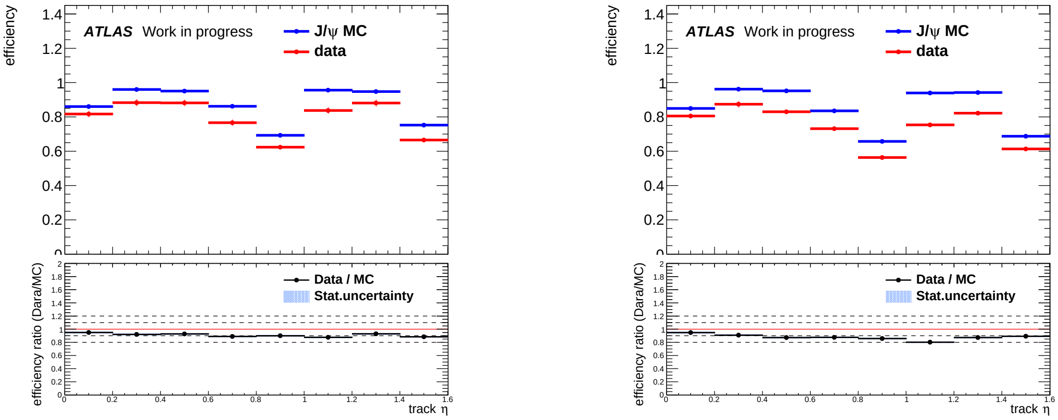

(c) 2.5 GeV < track p_T < 3.0 GeV

(d) 3.0 GeV < track p_T < 3.5 GeV

Figure9.4 The result of efficiency measurement using tag and probe method. (1.0 GeV < p_T < 3.5 GeV). The red and blue lines in the upper figure show the LCaT muon ID efficiency in J/ψ MC and data, respectively. The bottom figure shows the ratio of the efficiencies. The differences in the ratio from 1 are applied as systematic uncertainties.

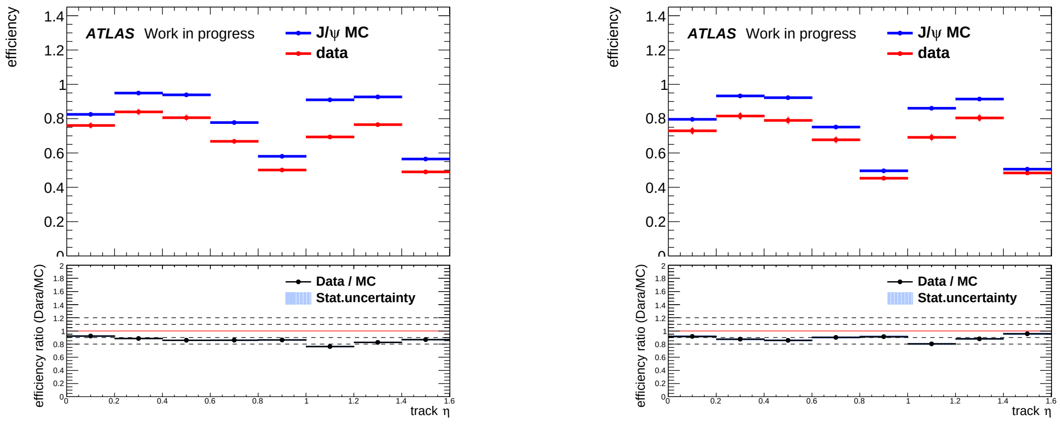

(a) 3.5 GeV < track p_T < 4.0 GeV

(b) 4.0 GeV < track p_T < 4.5 GeV

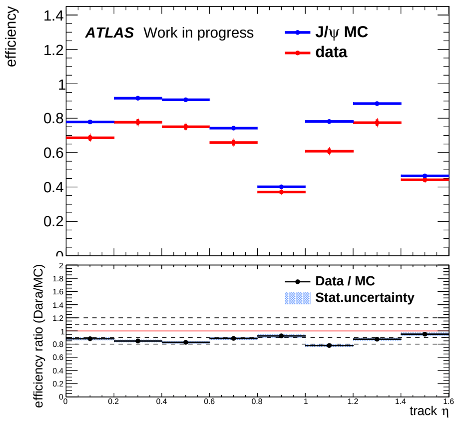

(c) 4.5 GeV < track p_T < 5.0 GeV

Figure9.5 The result of efficiency measurement using tag and probe method. (3.5 GeV < p_T < 5.0 GeV). The red and blue lines in the upper figure show the LCaT muon ID efficiency in J/ψ MC and data, respectively. The bottom figure shows the ratio of the efficiencies. The differences in the ratio from 1 are applied as systematic uncertainties.

9.4 Uncertainty of the difference between LCaT muon ID and LCaT muon estimator

In this section, uncertainties in the pNN score distribution caused by differences between LCat muon ID and LCaT are discussed. Hereafter, these uncertainties are referred as *uncertainty of the difference between LCaT muon ID and LCaT muon weight*. These uncertainties come from two components. Normalization of number of events, called as LCaT muon weight normalization uncertainty, and the distribution shape of the pNN score, as LCaT muon weight shape uncertainty. Here, LCaT muon weight shape uncertainty is classified into the statistical uncertainty part and systematic uncertainty part. The structure of the uncertainty of the difference LCaT muon ID and

LCaT muon weight is shown in figure 9.6. The detail of the LCaT muon weight normalization uncertainty is discussed in section 9.4.1, and the detail of the LCaT muon weight shape uncertainty is discussed in Section 9.4.2.

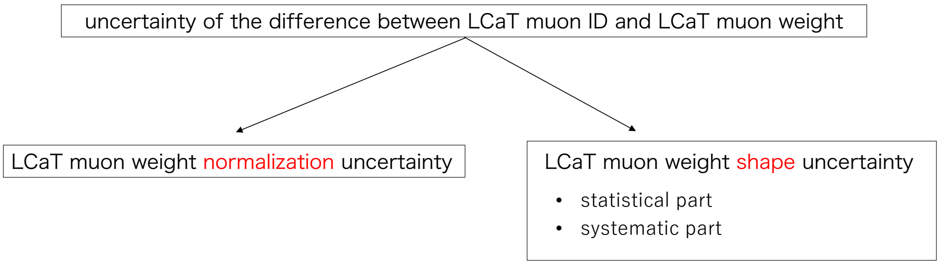

Figure9.6 structure of the uncertainty of the difference between LCaT muon ID and LCaT muon weight. the uncertainty of the difference between LCaT muon ID and LCaT muon weight can be separate into the LCaT muon weight normalization uncertainty and the LCaT muon weight shape uncertainty. Also, he LCaT muon weight shape uncertainty can be separate into statistical part and systematic part.

9.4.1 LCaT muon weight normalization uncertainty

In this section, the LCaT muon weight normalization uncertainty is estimated by using the VRs defined in Figure 8.2. In addition, a new VR ,that is close to SR, is defined in figure 9.7 (`VR_CloseSR`). On the other hand, `VR_LowpNN` is not used for the estimation of the LCaT muon weight normalization uncertainty since the expected total number of the background in `VR_LowpNN` is strongly affected by the LCaT muon weight shape uncertainty.

Figure 9.8 shows the total number of events using the LCaT muon ID and the expected total number of events using the LCaT muon weight in each region. In all VRs, the difference between the LCaT muon ID and the LCaT muon weight is within 10%. Therefore, we apply 10% as the LCaT muon weight normalization uncertainty.

Definition of CR for normalization factor

As described in Chapter 10 later, in final step, the number of backgrounds are estimated by fitting. In this case, the LCaT muon weight normalization factor is given in order to rescale number of background events. A control region (`CR_LCaTmuonWeight_Norm`) is defined to cal-

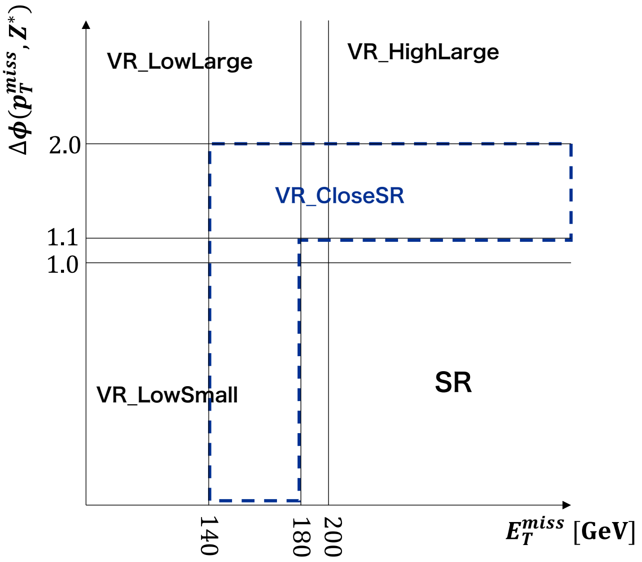

Figure9.7 Definition of VR_ClosSR. To avoid the signal contamination, low E_T^{miss} cut and large $\Delta\phi$ cut than SR are applied.

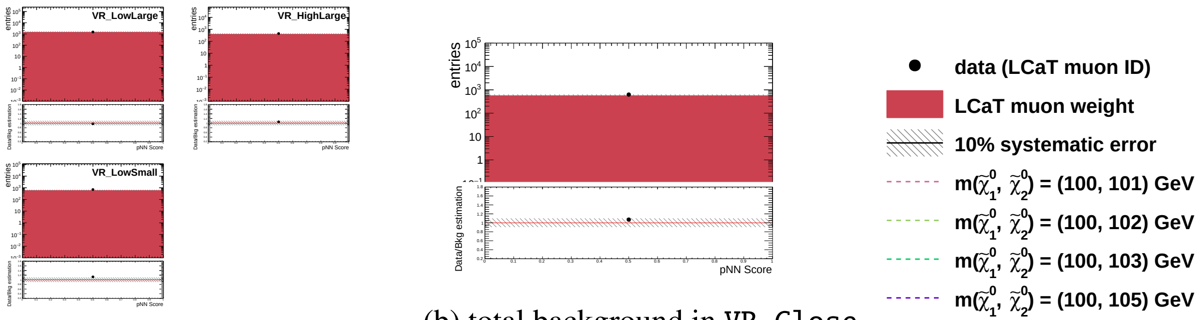

(b) total background in `VR_Close`

(a) total background in each VR

Figure9.8 Comparison between the estimated total background,which using the LCaT muon weight, and the total background, which using the LCaT muon ID, in each VR. The error is within 10% for all VRs. Therefore, 10% is applied as the LCaT muon weight normalization uncertainty.

culate the factor. As shown in Figure 9.9, the efficiency of LCaT muon ID does not depend on $\phi(E_T^{miss}, Z^*)$. It implies that the same factor can be used in SR. Therefore, we can define `CR_LCaTmuonWeight_Norm` and `VR_LCaTmuonWeight_Norm` by separating region in ϕ as shown in Figure 9.10. Also, `VR_LCaTmuonWeight_Norm` is used as a region for validation of the fitting.

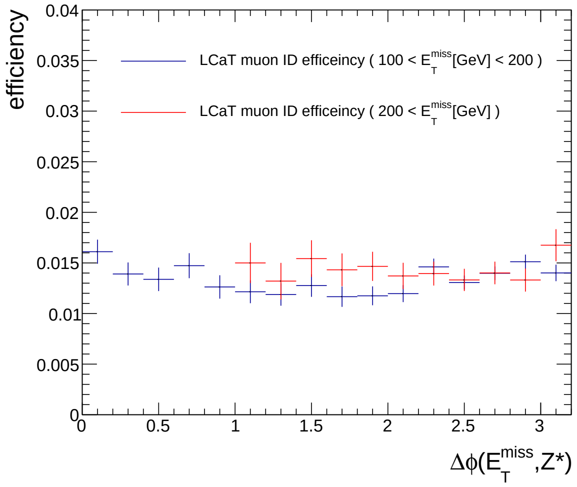

Figure9.9 $\Delta\phi(E_T^{miss}, Z^*)$ dependence of LCaT muon ID efficiency. The blue and red line shows LCaT muon ID efficiency in low E_T^{miss} region and high E_T^{miss} region, respectively. The efficiency is independent of $\Delta\phi$. Thus, it is possible to estimate the LCaT muon weight normalization factor in SR by using the large ϕ region.

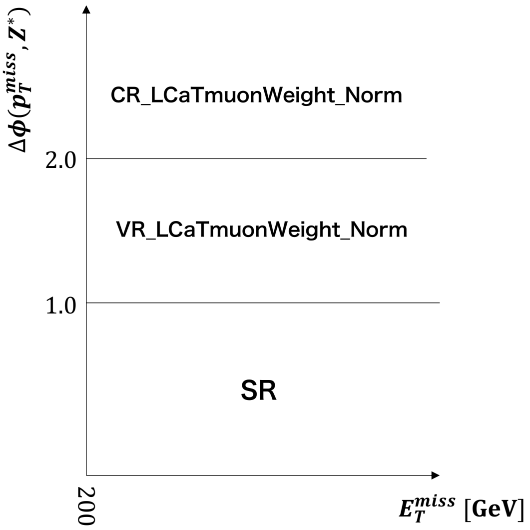

Figure9.10 Definition of `CR_LCaTmuonWeight_Norm` and `VR_LCaTmuonWeight_Norm`.

9.4.2 LCaT muon weight shape uncertainty

In this section, the LCaT muon weight shape uncertainty is estimated. The shape of the pNN score depends on the weight function for each variable in eq. (8.3). Figure 9.11 shows the overview of the estimation method of the uncertainty. The procedure is described below.

(1) Calculate the pNN score distribution using the LCaT muon weight($\omega_{LCaT,nomi}$) defined in section 8.5.

(2) Fluctuate the value of each weight function in the LCaT muon weight by using error (ε) and according to eq. 9.1.

(3) Calculate the pNN score using the fluctuated LCaT muon weight ($\omega_{LCaT,flac}$).

(4) To check only the fluctuation in the shape of the pNN score distribution, normalize pNN score distribution by the expected number of events when using $\omega_{LCaT,nomi}$.

(5) Evaluate the difference in each bin between the distribution when $\omega_{LCaT,nomi}$ is used (nominal distribution) and the distribution when $\omega_{LCaT,flac}$ is used (toy distribution).

(6) Perform (1) to (5) 1000 times while changing ε, and fit the distribution of the ratio between nominal and toy by Gauss function in each bin.

(7) The standard deviation of each Gauss function is used as the LCaT muon weight shape uncertainty.

$$\omega_{fract}^{variable}(variable) = \omega_{norm}^{variable}(variable) + \varepsilon^{variable}(variable) \tag{9.1}$$

The uncertainties estimated in this method depend on the choice of error (ε), which is added to the LCaT muon weight. The following equations give the ε.

$$\begin{aligned} \varepsilon^{variable}(variable) &\sim \mathcal{N}(0, \sigma^{variable}(variable)) \\ \sigma^{variable}(variable) &= \sqrt{(\sigma_{stat}^{variable}(variable))^2 + (\sigma_{syst}^{variable}(variable)^2} \end{aligned} \tag{9.2}$$

$\mathcal{N}(\mu, \sigma)$ means gauss distribution with mean μ and standard deviation σ, and ε is the value sampled from $\mathcal{N}(\mu, \sigma)$. The $\sigma_{stat}^{variable}$ is the statistical uncertainty limited by the amount of data used to create the LCaT muon weight. The $\sigma_{syst}^{variable}$ is the systematic error between LCaT muon ID and LCaT muon weight. In other words, since the LCaT muon weights are created using all regions of DF, the $\sigma_{syst}^{variable}$ is the difference between LCaT muon ID efficiencies in all regions of DF and SR of SF. To estimate the difference approximately, the difference between the LCaT muon ID weight created by using all VRs of SF and the LCaT muon weight defined in section 8 (using all regions of DF) is applied as $\sigma_{syst}^{variable}$. The details of $\sigma_{stat}^{variable}$ and $\sigma_{syst}^{variable}$ are described in the below paragraph.

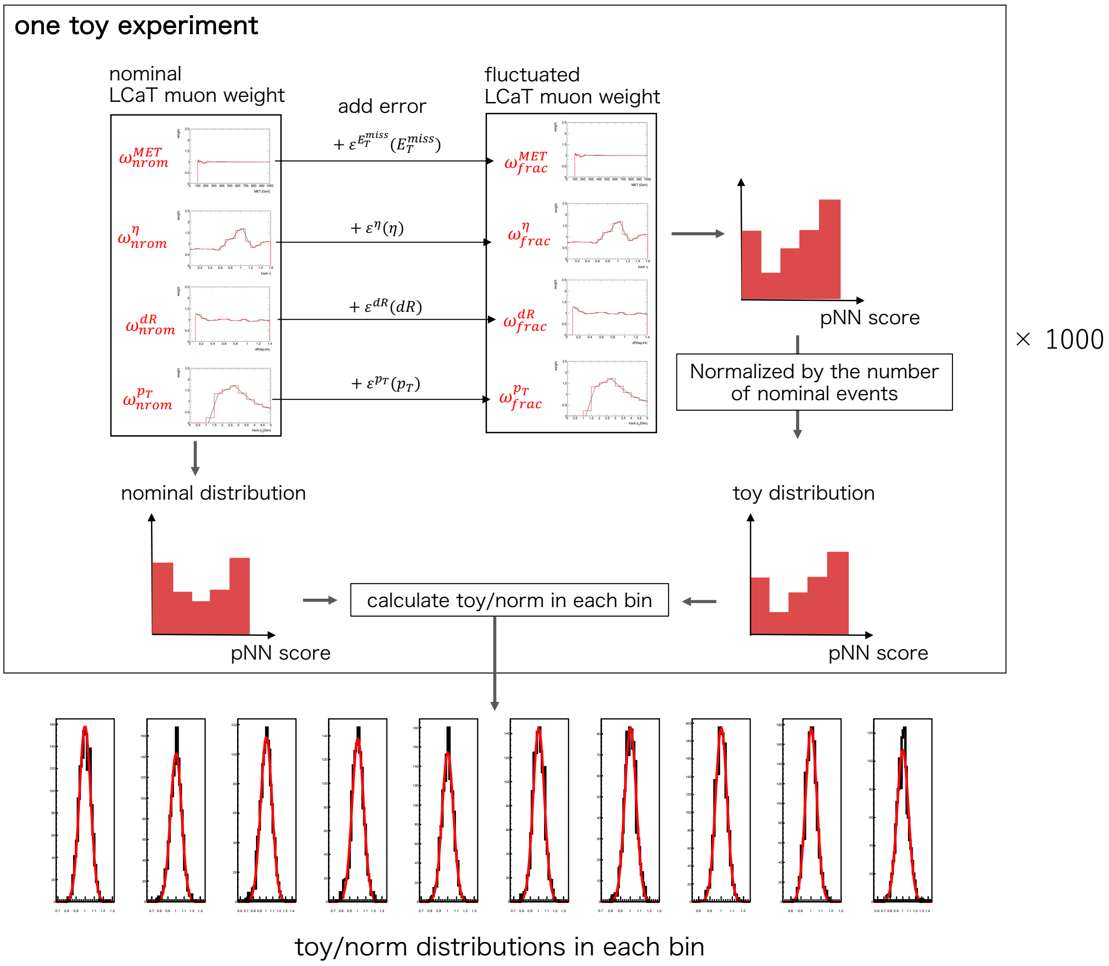

Figure9.11 overview of the estimation method of LCaT muon weight shape uncertainty. The fluctuation of pNN score distribution due to fluctuating the LCaT muon weight is examined by the toy experiment. Fit the distribution of ratio between toy and nominal by the Gauss function and apply its standard deviation as uncertainty.

Statistical part of the LCaT muon weight shape uncertainty

To estimate $\sigma_{stat}^{variable}$, the statistical error in each weight function of the LCaT muon weight is used. However, errors may be correlated to each other since each weight function is created from the same data. Therefore, it is examined whether there is a correlation in the distribution of data. The eq.(9.3) and eq.(9.4) are the Correlation Matrix with vector of $(p_T, \Delta R, E_T^{miss}, \eta)$. $Correlation\ Matrix(Before\ LCaTmuonID)$ and $Correlation\ Matrix(After\ LCaTmuonID)$ are the Correlation Matrix before and after applying the LCaT muon ID, respectively.

$$Correlation\ Matrix(Before\ LCaTmuonID) = \begin{pmatrix} 1 & -0.073 & 0.001 & 0.001 \\ -0.073 & 1 & 0.039 & -0.004 \\ 0.001 & 0.039 & 1 & 0.001 \\ 0.001 & -0.004 & 0.001 & 1 \end{pmatrix} \tag{9.3}$$

$$Correlation\ Matrix(After\ LCaTmuonID) = \begin{pmatrix} 1 & -0.032 & -0.002 & -0.017 \\ -0.032 & 1 & 0.042 & -0.0028 \\ -0.002 & 0.042 & 1 & 0.0058 \\ -0.017 & -0.0028 & 0.0058 & 1 \end{pmatrix} \tag{9.4}$$

Non diagonal terms of the matrix are much smaller than 1 and correlations are found to be small enough. It means there is no correlation in data distribution. Therefore, It is concluded that error(ε) can be given to each weight fluctuation independently.

difference between SF and DF as systematic part of the LCaT muon weight shape uncertainty

Next, $\sigma_{syst}^{variable}$ is estimated. As mentioned above, The difference between the LCaT muon weight created using all the VRs of SF and the LCaT muon weight created using all regions of DF is used as $\sigma_{syst}^{variable}$. Figure 9.12 shows the ratio between the two LCaT muon weights.

Large differences can be found in the region where p_T is above 4 GeV, but basically, the ratio is within ±20%. We apply the difference of the ratio from 1 as $\sigma_{syst}^{variable}$.

result of toy experiment

The $\sigma_{stat}^{variable}$ and $\sigma_{syst}^{variable}$ defined above were used to run the toy experiment 1000 times. Figure 9.13 shows the uncertainties for each pNN score in SR. approximately 1 to 20 % total uncertainties are applied as the LCaT muon weight shape uncertainty.

9.4.3 evaluation of the uncertainty

In this section, the estimated the uncertainty of the difference between LCaT muon ID and LCaT muon weight is evaluated. Figure 9.14 and Figure 9.15 show the background estimation, its uncertainty and data using LCaT muon ID. Most of the data points are consistent with the estimation within the range of uncertainty. Therefore, we conclude that the estimation of the uncertainty is correct.

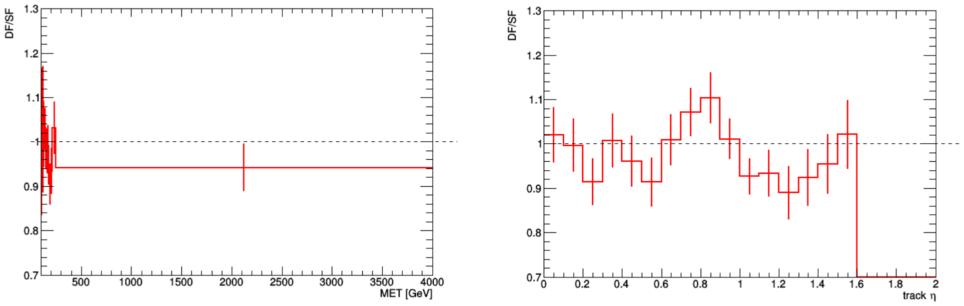

(a) E_T^{miss} (b) η

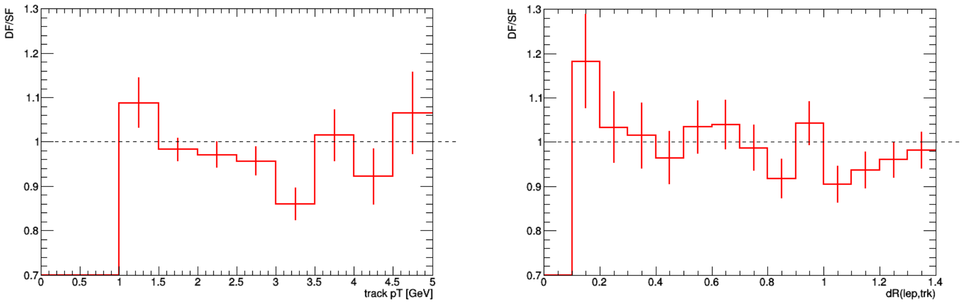

(c) p_T (d) ΔR

Figure9.12 The Ratio between the weights in which LCaT muon estimator created using all the VRs in SF and the LCaT muon weight created using all regions in DF. The difference of the ratio from 1 is applied as $\sigma_{syst}^{variable}$.

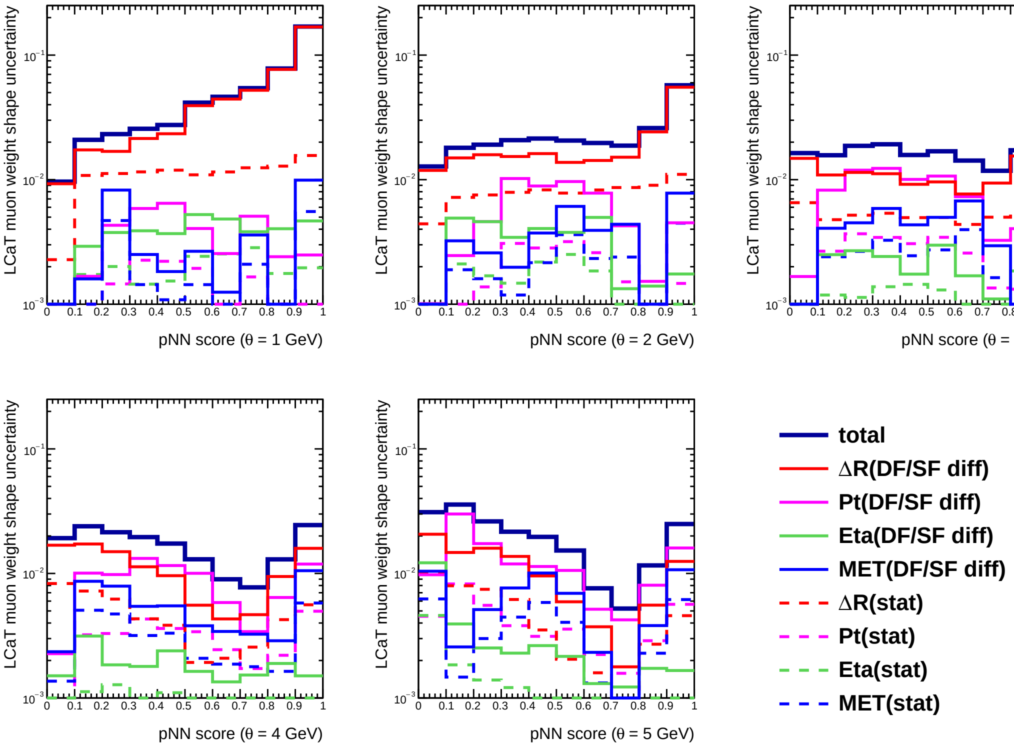

Figure9.13 The uncertainties from each component for each pNN score in SR. The solid and dotted lines represent the effect of the systematic part estimated from the difference between SF and DF, and the statistical part associated with the bin used for creation of the LCaT muon estimator, respectively.

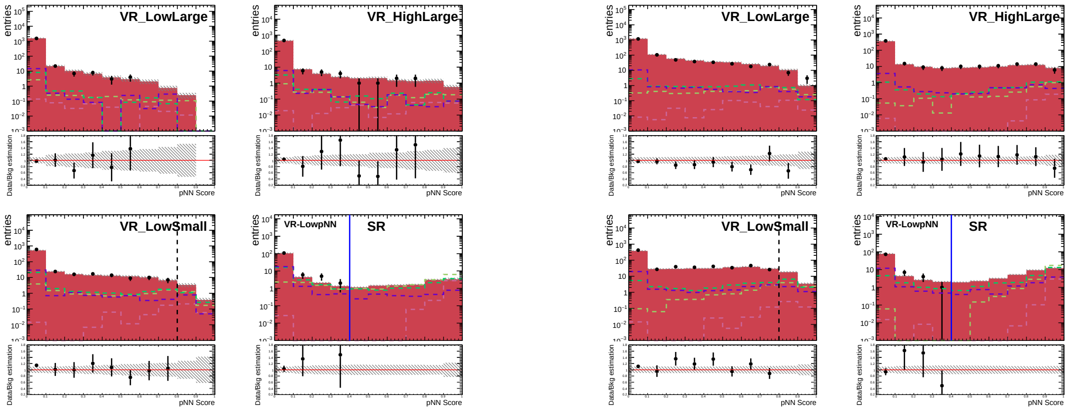

(a) pNN-θ = 1 GeV (b) pNN-θ = 2 GeV

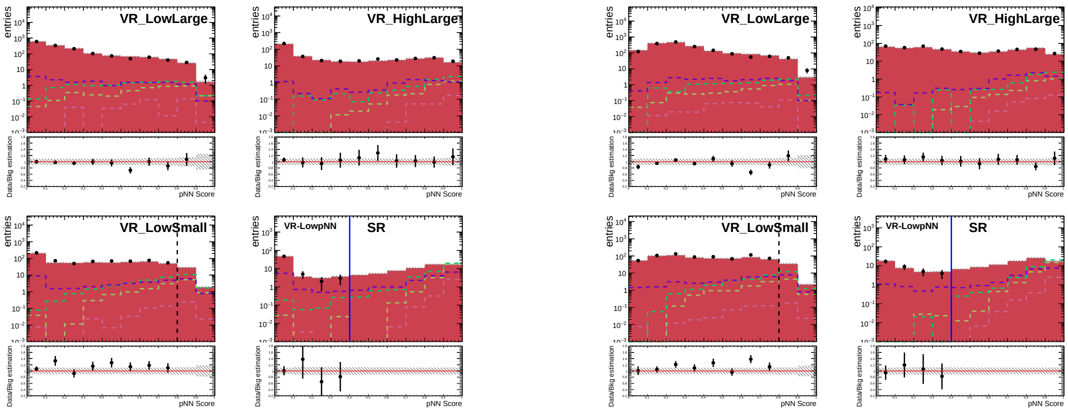

(c) pNN-θ = 3 GeV (d) pNN-θ = 4 GeV

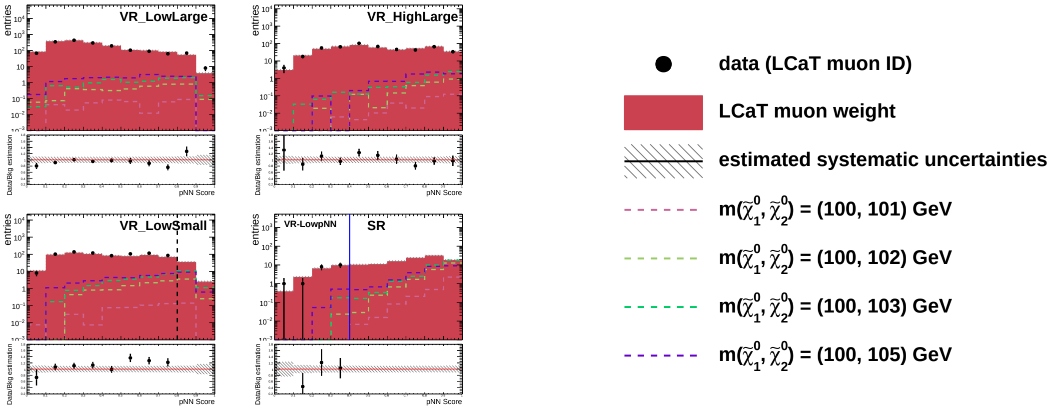

(e) pNN-θ = 5 GeV

Figure9.14 The result of background estimation. The dark red histogram is the distribution of the background estimated by the LCaT muon weight method, and the black dots are the results of the data obtained by applying the LCaT muon ID. Good agreement between background estimation and data is observed, and the most of difference is within systematic uncertainties.

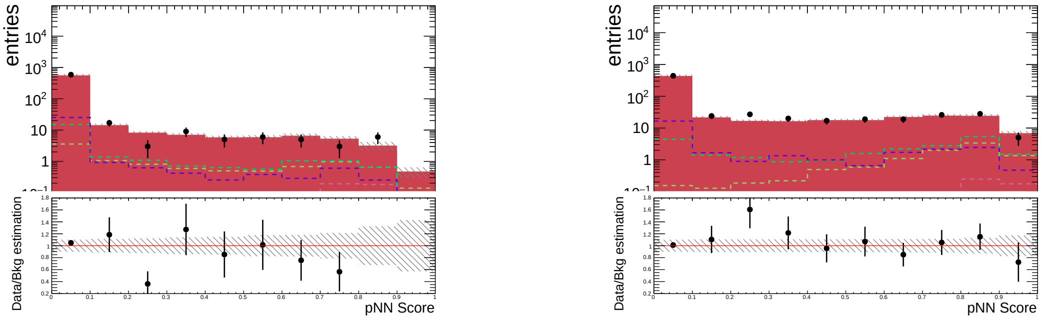

(a) pNN-θ = 1 GeV (b) pNN-θ = 2 GeV

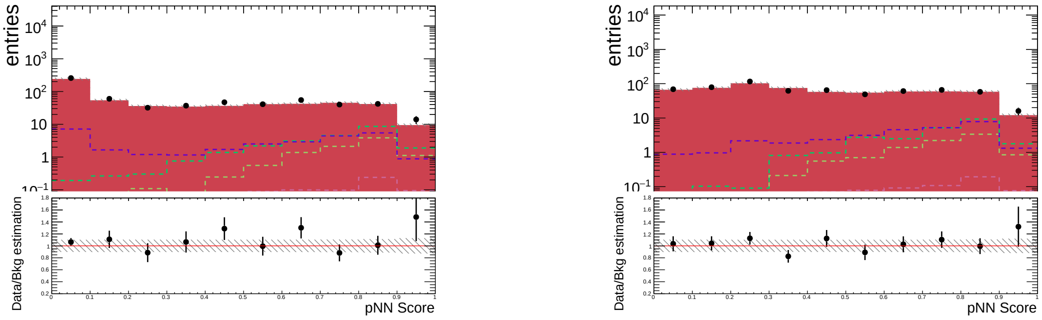

(c) pNN-θ = 3 GeV (d) pNN-θ = 4 GeV

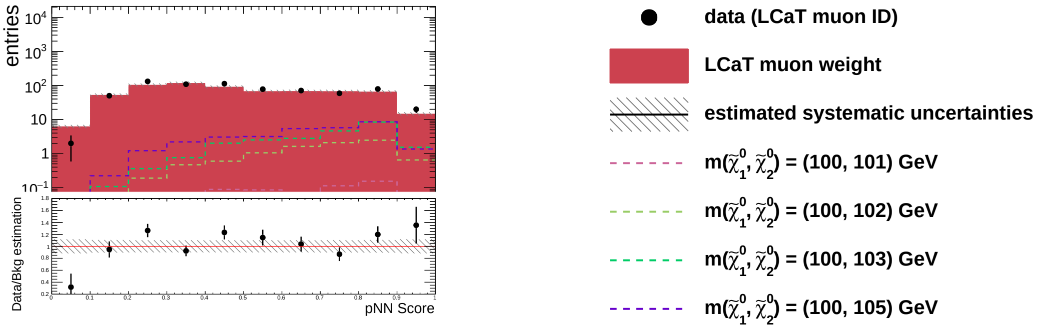

(e) pNN-θ = 5 GeV

Figure9.15 The result of background estimation in `VR_CloseSR`. The dark red histogram is the distribution of the background estimated by the LCaT muon weight method, and the black dots are the results of the data obtained by applying the LCaT muon ID. Good agreement between background estimation and data is observed, and the most of difference is within systematic uncertainties.

10. Statistical treatment

There are several interpretations for the obtained measurement results. For example, when the observed result is more than the background estimation, it can be interpreted either because there is a signal or because there is an error in the background estimation. In order to determine the interpretation, we have to determine the unknowns parameters. One of the unknown parameters is signal strength. Also, the LCaT muon weight normalization factor, which determines the number of backgrounds, can change its value within its uncertainty. Section 10.1 describes how to find the values of these unknown parameters that best explain the obtained observed results. The strength of the signal is denoted as μ, and the other unknown parameters are denoted as the nuisance parameter (θ). Also, The initial value of the θ and its uncertainty are denoted as $\tilde{\theta}$ and σ, respectively. In addition, Section 10.2 describes how to evaluate the obtained results.

10.1 Profile Likelihood

To determine the nuisance parameter(θ), we define likelihood($L(\mathbf{x}, \theta)$) and find θ such that $L(\mathbf{x}, \theta)$ is maximized. The definition of $L(\mathbf{x}, \theta)$ is as follows.

$$L(\mathbf{x}, \theta) = \prod_{region}^{N} \frac{(E_{region}(\theta))^{x_{region}}}{x_{region}} e^{-E_{region}(\theta)} \cdot p(\theta|\tilde{\theta}) \tag{10.1}$$

Where $\mathbf{x}$ is the number of observed events, and $E_{region}(\theta)$ is the number of estimated backgrounds. $p(\theta|\tilde{\theta})$ is a term that penalizes θ when its value is differ significantly from the initial predicted value($\tilde{\theta}$). The detail is described in 10.1.1. The first part of eq.(10.1) is a Poisson distribution function, which expresses the probability of observing x_{region} when the expected value of background is $E_{region}(\theta)$. Therefore, maximizing the $L(\mathbf{x}, \theta)$ means that the θ with the highest probability of observing x_{region} is given while keeping the low penalty from $p(\theta|\tilde{\theta})$. Such θ is denoted as $\hat{\theta}$ and is defined by the following equation.

$$\hat{\theta} = \arg\max_{\theta} L(\mathbf{x}, \theta) \tag{10.2}$$

When considering signal, $E_{region}(\mu, \theta)$ defined in eq.(10.3) is used instead of $E_{region}(\theta)$.

$$E_{region}(\mu, \theta) = \mu s_{region}(\theta) + b_{region}(\theta) \tag{10.3}$$

μ is the signal strength and is introduced as a free parameter. In other words, no penalty is applied to μ. The likelihood with μ is also defined as eq.(10.4)

$$L(\mathbf{x},\mu,\theta) = \prod_{region}^{N} \frac{(E_{region}(\mu,\theta))^{x_{region}}}{x_{region}} e^{-E_{region}(\mu,\theta)} \cdot p(\theta|\tilde{\theta}) \tag{10.4}$$

μ and θ that maximize L are also denoted as $\hat{\mu}$ and $\hat{\theta}$. The following equation defines these.

$$(\hat{\mu},\hat{\theta}) = \arg\max_{\theta} L(\mathbf{x},\theta,\mu) \tag{10.5}$$

The profile likelihood method[65] is used to evaluate the significance and calculate the upper limit for the signal strength(μ). Initially, this method maximizes $L(\mathbf{x},\theta,\mu)$ with certain value of the signal strength. θ that maximize L with specific μ is denoted as $\hat{\hat{\theta}}$. Also, we define the profile likelihood ratio in eq.(10.12).

$$\lambda(\mu) = \frac{L(\mathbf{x},\mu,\hat{\hat{\theta}})}{L(\mathbf{x},\hat{\mu},\hat{\theta})} \tag{10.6}$$

The $\lambda(\mu)$ takes values from 0 to 1, and $\lambda(\mu) = 1$ means a good agreement between the data and the hypothesized μ.

10.1.1 Treatment of systematic uncertainties

In this section, we define $p(\theta|\tilde{\theta})$ as the penalty for θ. The measurement of θ given before fitting with likelihood is denoted as $\tilde{\theta}$, and its uncertainty is denoted as σ. Also, the conditional probability density function as a function of θ_{truth} under the $\tilde{\theta}$ is denoted as $\rho(\theta_{truth}|\tilde{\theta})$. We consider $\rho(\theta_{truth}|\tilde{\theta})$ as the posterior distribution in Bayse' theorem, and the Bayse' theorem is expressed by eq. (10.7).

$$\rho(\theta_{truth}|\tilde{\theta}) = p(\tilde{\theta}|\theta_{truth}) \times \pi(\theta_{truth}) \tag{10.7}$$

where $p(\tilde{\theta}|\theta_{truth})$ is called the likelihood function and $\pi(\theta_{truth})$ is called the prior distribution. We assume that $\pi(\theta_{truth})$ has a flat distribution. It means that we don't make any assumptions about the values that θ_{truth} should take. Therefore, eq.(10.7) can be expressed as $\rho(\theta_{truth}|\tilde{\theta}) = p(\tilde{\theta}|\theta_{truth})$. $p(\tilde{\theta}|\theta_{truth})$ expresses the conditional probability density function as a function of $\tilde{\theta}$ under the θ_{truth}. Gauss function and Gamma function is used as the probability density function. Thus, $\rho(\theta_{truth}|\tilde{\theta})$ can be expressed as eq.(10.8) or eq.(10.9). For systematic uncertainties, the Gauss function is assumed. On the other hand, It is known that the Gamma function is more proper for statistical uncertainties [66].

$$\rho(\theta_{truth}|\tilde{\theta}) = p(\tilde{\theta}|\theta_{truth}) = \frac{1}{\sqrt{2\pi}} \exp\,(-\frac{(\theta_{truth}-\tilde{\theta})^2}{2\sigma^2}) \tag{10.8}$$

$$\rho(\theta_{truth}|N) = p(N|\theta_{truth}) = \frac{\theta_{truth}^{N}}{N!} \exp \theta_{truth} \tag{10.9}$$

From the above, when $\tilde{\theta}$ is measured, the probability that θ_{truth} is θ can be calculated by the following equation.

$$p(\theta|\tilde{\theta}) = \prod_{i} p(\theta_i|\tilde{\theta}) \tag{10.10}$$

eq.(10.10) works as a penalty term in the likelihood(eq.(10.1)).

10.2 Hypothesis testing

This section describes how to evaluate the obtained observed data. For convenience, the profile likelihood ratio is converted by the following equation.

$$t_{\mu} = -2 \ln \lambda(\mu) \tag{10.11}$$

The t_{μ} is called *test statistics* and used for the statistical test. $t_{\mu} = 0$ means a good agreement between the data and the hypothesized μ, and the larger t_{μ} means a worse agreement. As a test of the hypothesized μ, we define the p-value as follows.

$$p_{\mu} = \int_{t_{\mu_{obs}}}^{\infty} f(t_{\mu}|\mu) dt_{\mu} \tag{10.12}$$

where $f(t_{\mu}|\mu)$ is the probability density function of t_{μ}, Also, by definition, $p_{\mu_{obs}} = 0.5$ means that the data and hypothesis μ are in good agreement. $f(t_{\mu}|\mu)$ is obtained by the asymptotic formula based on the Asimov dataset[65]. Schematic diagrams of $f(t_{\mu}|\mu)$ and $p_{\mu_{obs}}$ are shown in Figure 10.1.

In this thesis, we will perform the following test.

Discovery test

In the discovery test, the p-value (p_0) with $f(t_{\mu}|\mu = 0)$ is used to claim discovery when significant excess is observed against background estimation. When there is significant excess, p_0 takes a small value. $p_0 < 0.0027$ and $p_0 < 6 \times 10^{-7}$ correspond to 3σ and 5σ, respectively.

Upper limit test

In the upper limit test, the exclusion of the signal hypothesis is claimed when the results of data and background estimation are consistent. To claim the exclusion, we define the confidence level in eq.(10.15).

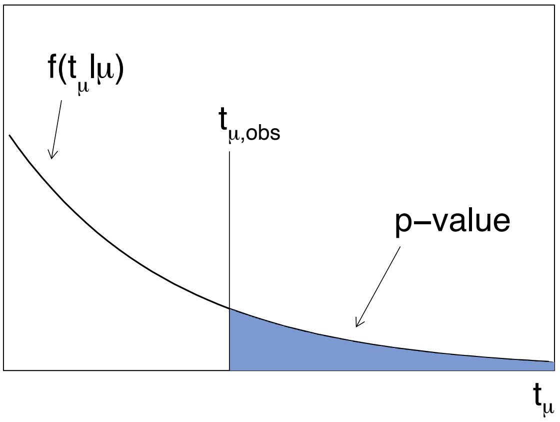

Figure10.1 An example of the t_μ distribution and $p_{\mu_{obs}}$

$$CL_b = \int_{t_{\mu_{obs}}}^{\infty} f(t_\mu|\mu)dt_\mu = p_\mu \tag{10.13}$$

$$CL_b = \int_{t_{\mu_{obs}}}^{\infty} f(t_\mu|\mu = 0)dt_\mu = p_0 \tag{10.14}$$

$$CL_s = \frac{CL_{s+b}}{CL_b} = \frac{p_\mu}{p_0} \tag{10.15}$$

When a CLs value is less than 0.05, its signal hypothesis is excluded at the 95% confidence level.

In this test, we select one SR out of the SRs listed in Table7.5 and fit it simultaneously with CR. S^{95}_{exp} and S^{95}_{obs} are denoted as the expected and observed excluded number of signal events in selected SR. In other words, the number of signal events in the hypothesized signal for which the p-value is 0.05. Also, ε is denoted as the efficiency of signal event entering the SR, and the visible cross section is defined as the cross section that includes the efficiency by the following equation.

$$< \varepsilon\sigma >^{95}_{obs} = \frac{S^{95}_{obs}}{\int Ldt} \tag{10.16}$$

where $\int Ldt$ is integrated luminosity. This visible cross section is a restriction that does not strongly depend on the scenario of the Beyond Standard Model(BSM).

Exclusion test

In this test, we assume a SUSY scenario and use the shape information of the pNN score. In other words, all SRs and CRs are fit simultaneously to evaluate the limit. Unlike the Upper limit test, it strongly depends on the model of BSM, but it can calculate a more tight limit. As same with the Upper limit test, we exclude the scenarios at the 95% confidence level.

11. Result

This chapter describes the result of unblinding Signal Regions and its interpretation. The definition of each SR are listed in Table 7.5. Here, we have tested various hypothesis (see 10.2) using these results. The results of each test is described in sections from 11.1 to 11.3, and the interpretations for pMSSM is discussed in section 11.4.

11.1 Background only fit

In this section, the results of the background only fit are discussed. In this fit, the value of the nuisance parameter is determined using Control Region （CR) only. The number of background events is estimated by extrapolated the fitted shape to the SR. Then it is compared to the observed number of events.

Fig.11.1 shows the number of observed events with estimated backgrounds. The dark red histogram in the upper figure is the estimated background, and the black dots with error bars are observed data. The lower figure shows the significance of the difference between observed data and estimated background, which is calculated using the formula in Ref.[67]. All pNN-θ results show good agreement between background and data. It means that background estimation is done well. The largest excess is 1.98σ at `SR-pNNScore-F`(0.9< pNNscore < 1.0) with pNN-θ=3 GeV, and the largest deficit is 1.71σ at `SR-pNNScore-C`(0.6< pNNscore < 0.7) with pNN-θ=1 GeV . Large excesses are re-evaluated in the Discovery test (section 11.2).

11.2 Discovery test and Upper limit test

This section describes the Discovery test and Upper limit test. In the Discovery test, the the p-value in the null hypothesis is evaluated by simultaneously fitting with CR and one SR. If small p-value is obtained, the null hypothesis is rejected and the existence of a new particle is suggested. Conventionally, we may declare "discovery" with $p_0 < 6 \times 10^{-7}$. In case of no discovery, the 95% CL upper limit of the visible cross section (eq. 10.16) can be estimated in the Upper limit test.

Table11.1-11.5 shows the results of Discovery test and Upper limit test. The p-values are shown in the last column of the tables. The smallest p-value is 0.024 at `SR-pNNScore-F` with pNN-θ=3 GeV. The p-value corresponds to 1.97σ, which dose not reach to claim existence of a new particle. In addition, an upper limit to the visible cross section is given. The 95 % CL upper limit of cross section at `SR-pNNScore-F` with pNN-θ=3 GeV is 0.136fb.

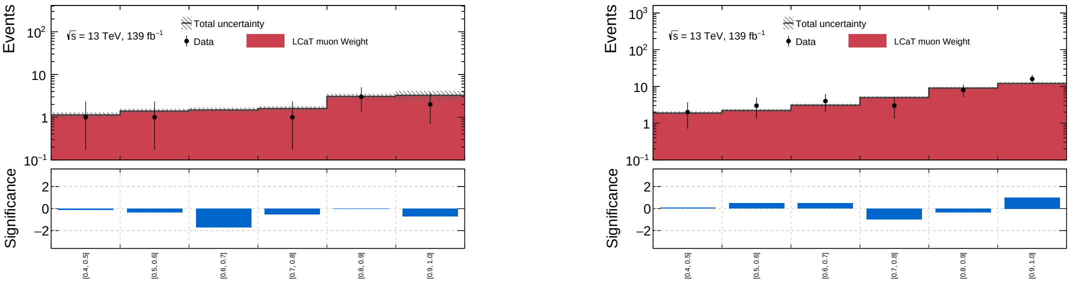

(a) pNN-θ = 1 GeV (b) pNN-θ = 2 GeV

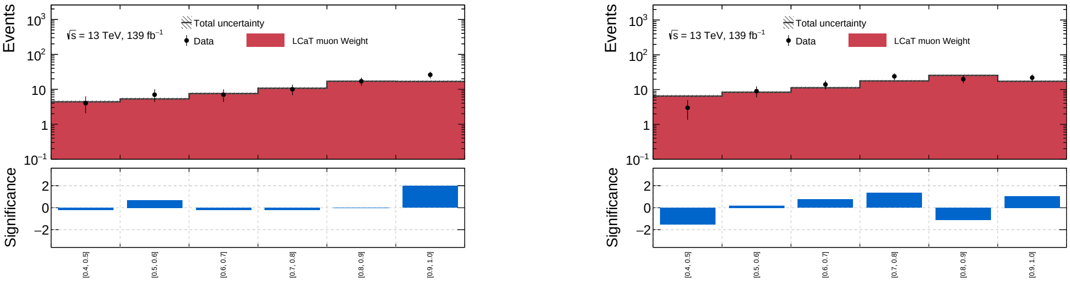

(c) pNN-θ = 3 GeV (d) pNN-θ = 4 GeV

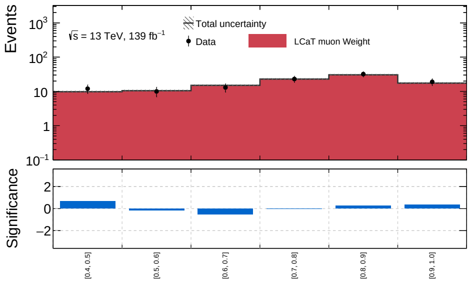

(e) pNN-θ = 5 GeV

Figure11.1 The result of background estimation in each SRs and each pNN-θ as a function of the pNN score. The dark red histogram is the distribution of the background estimated by the LCaT muon weight method, and the black dots are observed events in the *pp* collision data. The lower plot shows significance between data and estimated background. Good agreement is observed, and the largest excess is 1.98σ at `SR-pNNScore-F`(0.9< pNNscore < 1.0) with pNN-θ = 3 GeV

Table11.1 The results of upper limit and discovery test with pNN $\theta = 1$ GeV. Left to right: The observed number of events(N_{obs}), the expected number of events(N_{exp}), 95% CL upper limits on the visible cross section $\left(\langle\epsilon\sigma\rangle^{95}_{\mathrm{obs}}\right)$ and on the number of signal events $\left(S^{95}_{\mathrm{obs}}\right)$, the 95% CL upper limit on the number of signal events$\left(S^{95}_{\mathrm{exp}}\right)$, given the expected number (and $\pm 1\sigma$ deviations from the expectation) of background events. The last column calculated for SR with $N_{obs} > N_{exp}$. It indicates the discovery p-value ($p(s = 0)$) and significance.

Signal Region (pNN-θ = 1 GeV)	N_{obs}	N_{exp}	$\langle\epsilon\sigma\rangle^{95}_{\mathrm{obs}}$ [fb]	S^{95}_{obs}	S^{95}_{exp}	p_0
`SR-pNNScore-F`	2	3.007 ± 0.759	0.029	4.0	$5.0^{+2.7}_{-1.7}$	-
`SR-pNNScore-E`	3	3.072 ± 0.438	0.035	4.8	$4.9^{+2.7}_{-1.6}$	-
`SR-pNNScore-D`	1	1.584 ± 0.208	0.024	3.3	$3.9^{+2.4}_{-1.4}$	-
`SR-pNNScore-C`	0	1.442 ± 0.195	0.017	2.4	$3.8^{+2.3}_{-1.4}$	-
`SR-pNNScore-B`	1	1.386 ± 0.184	0.024	3.3	$3.7^{+2.3}_{-1.3}$	-
`SR-pNNScore-A`	1	1.130 ± 0.161	0.024	3.4	$3.5^{+2.2}_{-1.3}$	-

Table11.2 The results of upper limit and discovery test with pNN $\theta = 2$ GeV.

Signal Region (pNN-θ = 2 GeV)	N_{obs}	N_{exp}	$\langle\epsilon\sigma\rangle^{95}_{\mathrm{obs}}$ [fb]	S^{95}_{obs}	S^{95}_{exp}	p_0
`SR-pNNScore-F`	16	12.093 ± 1.084	0.087	12	$8^{+4}_{-2.6}$	0.15 (1.02σ)
`SR-pNNScore-E`	8	9.002 ± 0.671	0.047	6	$7^{+4}_{-2.3}$	-
`SR-pNNScore-D`	3	4.938 ± 0.418	0.030	4.2	$5.8^{+3.0}_{-1.9}$	-
`SR-pNNScore-C`	4	3.103 ± 0.306	0.042	5.8	$4.9^{+2.7}_{-1.7}$	0.31 (0.48σ)
`SR-pNNScore-B`	3	2.219 ± 0.227	0.037	5.2	$4.3^{+2.5}_{-1.5}$	0.31 (0.49σ)
`SR-pNNScore-A`	2	1.894 ± 0.213	0.030	4.2	$4.1^{+2.4}_{-1.4}$	0.47 (0.07σ)

Table11.3 The results of upper limit and discovery test with pNN $\theta = 3$ GeV.

Signal Region (pNN-θ = 3 GeV)	N_{obs}	N_{exp}	$\langle\epsilon\sigma\rangle^{95}_{\mathrm{obs}}$ [fb]	S^{95}_{obs}	S^{95}_{exp}	p_0
`SR-pNNScore-F`	26	16.814 ± 1.237	0.136	19	$10^{+5}_{-3.0}$	0.02 (1.97σ)
`SR-pNNScore-E`	17	17.025 ± 1.144	0.069	10	$10^{+5}_{-3.0}$	-
`SR-pNNScore-D`	10	10.683 ± 0.797	0.053	7	$8^{+4}_{-2.5}$	-
`SR-pNNScore-C`	7	7.536 ± 0.571	0.046	6.3	$6.8^{+3.4}_{-2.2}$	-
`SR-pNNScore-B`	7	5.325 ± 0.445	0.055	7.6	$6.0^{+3.1}_{-1.9}$	0.25 (0.68σ)
`SR-pNNScore-A`	4	4.380 ± 0.376	0.037	5.1	$5.5^{+3.0}_{-1.8}$	-

Table11.4 The results of upper limit and discovery test with pNN $\theta = 4$ GeV.

Signal Region (pNN-θ = 4 GeV)	N_{obs}	N_{exp}	$\langle\epsilon\sigma\rangle^{95}_{\rm obs}$ [fb]	$S^{95}_{\rm obs}$	$S^{95}_{\rm exp}$	p_0
`SR-pNNScore-F`	22	17.311 ± 1.233	0.101	14	$10^{+5}_{-3.0}$	0.15 (1.03σ)
`SR-pNNScore-E`	20	25.142 ± 1.499	0.06	8	$12^{+5}_{-3.5}$	-
`SR-pNNScore-D`	24	17.777 ± 1.202	0.113	16	$10^{+5}_{-3.0}$	0.09 (1.34σ)
`SR-pNNScore-C`	14	11.303 ± 0.824	0.076	11	$8^{+4}_{-2.5}$	0.22 (0.75σ)
`SR-pNNScore-B`	9	8.405 ± 0.630	0.055	7.7	$7.1^{+3.6}_{-2.3}$	0.42 (0.20σ)
`SR-pNNScore-A`	3	6.370 ± 0.504	0.028	3.9	$6.4^{+3.3}_{-2.1}$	-

Table11.5 The results of upper limit and discovery test with pNN $\theta = 5$ GeV.

Signal Region (pNN-θ = 5 GeV)	N_{obs}	N_{exp}	$\langle\epsilon\sigma\rangle^{95}_{\rm obs}$ [fb]	$S^{95}_{\rm obs}$	$S^{95}_{\rm exp}$	p_0
`SR-pNNScore-F`	19	17.474 ± 1.220	0.080	11	$10^{+5}_{-3.0}$	0.37 (0.35σ)
`SR-pNNScore-E`	32	30.515 ± 1.831	0.10	14	13^{+6}_{-4}	0.40 (0.25σ)
`SR-pNNScore-D`	23	22.925 ± 1.390	0.08	11	$11^{+5}_{-3.3}$	0.50 (0.01σ)
`SR-pNNScore-C`	13	14.901 ± 0.958	0.055	8	$9^{+4}_{-2.8}$	-
`SR-pNNScore-B`	10	10.461 ± 0.738	0.053	7	$8^{+4}_{-2.5}$	-
`SR-pNNScore-A`	12	9.800 ± 0.712	0.069	10	$8^{+4}_{-2.4}$	0.25 (0.66σ)

11.3 Exclusion test for Higgsino like LSP scenario

This section describes the result of the exclusion test. Figure 11.2 shows the expected exclusion contour in the mass of $\tilde{\chi}^0_2$ and $\Delta m(\tilde{\chi}^0_1,\tilde{\chi}^0_2)$ plane in Higgsino like LSP scenario. Pink, orange, green, blue, and purple are the results when pNN-θ is 1 GeV, 2 GeV, 3 GeV, 4 GeV, and 5 GeV, respectively. It can be seen that the smaller pNN-θ has high sensitivity for smaller $\Delta m(\tilde{\chi}^0_1,\tilde{\chi}^0_2)$, and the larger pNN-$\theta$ has high sensitivity for larger $\Delta m(\tilde{\chi}^0_1,\tilde{\chi}^0_2)$. The contour that excludes the highest $\tilde{\chi}^0_2$ mass is one with pNN-θ = 3 GeV, where $\tilde{\chi}^0_2$ mass below 137 GeV is excluded for Δm = 3 GeV.

Figure 11.3 shows the observed and expected exclusion limit in each pNN-θ. (Note : some of the contours are broken due to lack of signal MC samples.) All pNN-θ results ,except for the pNN-θ =3 GeV, are within $\pm 1\sigma$ from the expected values. The pNN-θ =3 GeV result has a smaller excluded region due to the 1.9σ excess in `SR-pNNScore-F`, but the region between observed limit and -1 σ with pNN-θ =3 GeV is excluded by other pNN-θ results. Therefore, the

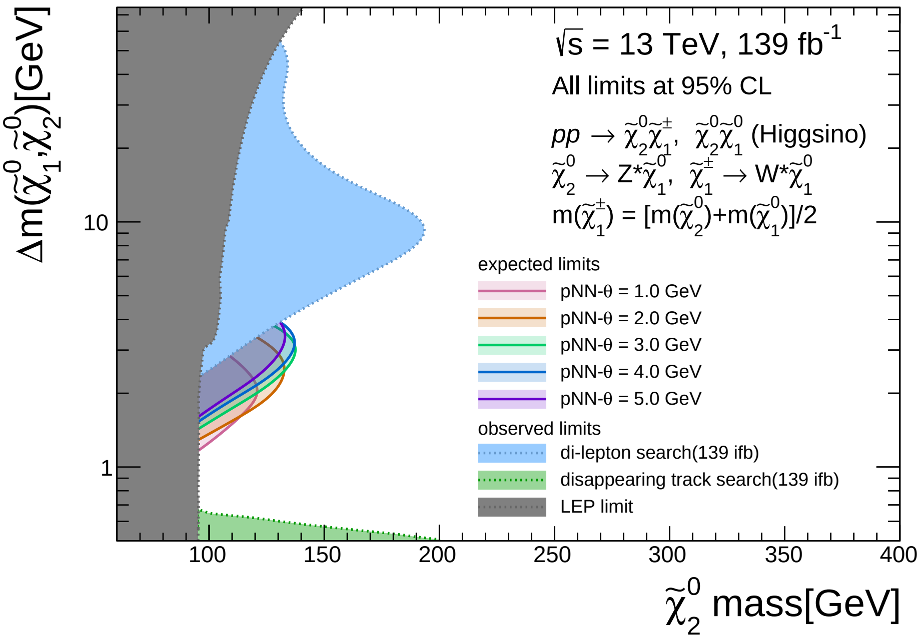

Figure11.2 exclusion contours in each pNN-θ (Higgsino like LSP scenario). Pink, orange, green, blue, and purple are the results when pNN-θ is 1 GeV, 2 GeV, 3 GeV, 4 GeV, and 5 GeV, respectively.

excess in textttSR-pNNScore-F is unlikely caused by production of Higgsino like LSP.

Figure 11.4 shows the observed and expected contour that connects the highest sensitivity results in each Δm from results with pNN-θ = 2,3,4,5 GeV.with the band of $1\ \sigma$

As the result, the observed exclusion limit reaches to down to Δm = 1.4 GeV and up to $m(\tilde{\chi}_2^0)$ = 125 GeV against expected exclusion limit down to Δm = 1.2 GeV and up to $m(\tilde{\chi}_2^0)$ = 137 GeV. Both observed and expected are most sensitive for Δm is around 3 GeV. The reason is the balance of the following three factors.

The first is the number of backgrounds. As discussed in section 7.3.1, the mass distribution of the off-shell Z boson is strongly dependent on Δm. It implies that events with an off-shell Z boson, with smaller mass than Δm, are the background. Therefore, if Δm is smaller, the mass range for off-shell Z boson is severely limited, and the number of backgrounds is reduced. As a result, a higher sensitivity can be obtained in smaller Δm.

The second is the efficiency of the standard muon ID. In our analysis called as '1 standard muon + 1 LCaT muon search', one muon from Z* is identified as the signal muon and another is identifed by LCaT muon ID. In other words, the lower p_T muon does not satisfy the standard

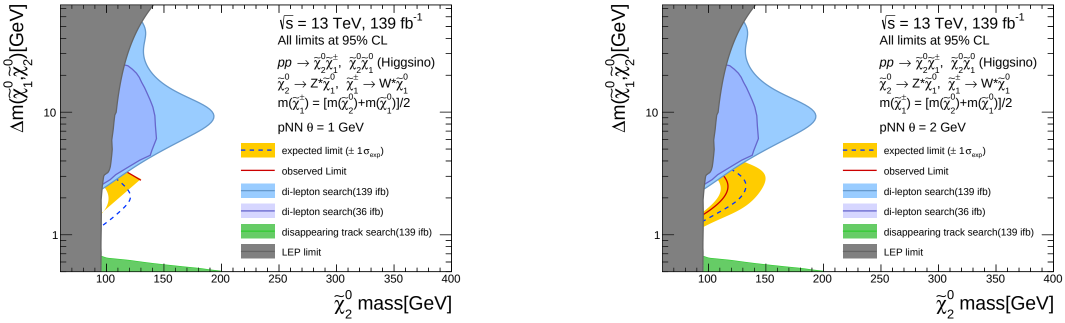

(a) pNN-θ = 1 GeV (b) pNN-θ = 2 GeV

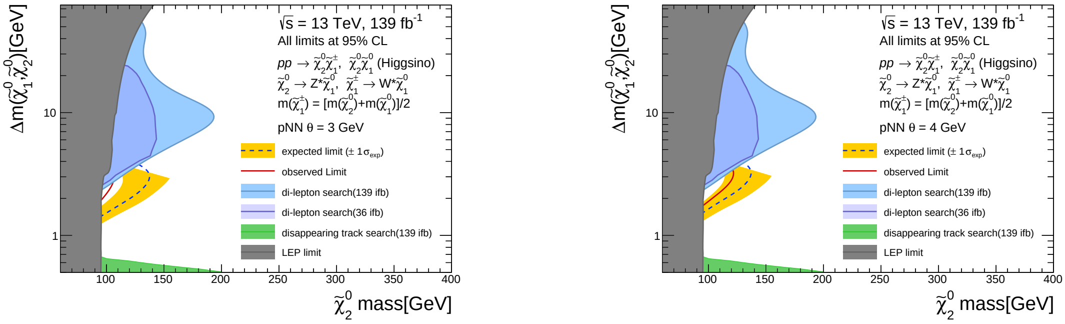

(c) pNN-θ = 3 GeV (d) pNN-θ = 4 GeV

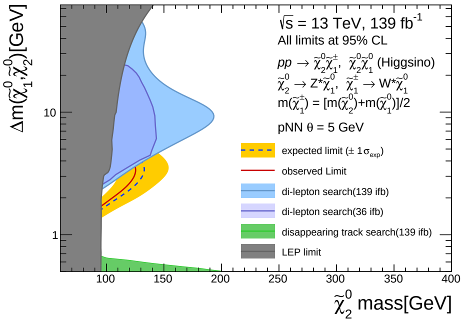

(e) pNN-θ = 5 GeV

Figure11.3 exclusion contours in each pNN-θ for the Higgsino like LSP scenario. The red line is observed limit, and the blue dashed line shows the nominal value of the expected exclusion contour. The yellow band represents the uncertainty of ± 1 σ. (Note : some of the contours are broken due to lack of signal MC samples.)

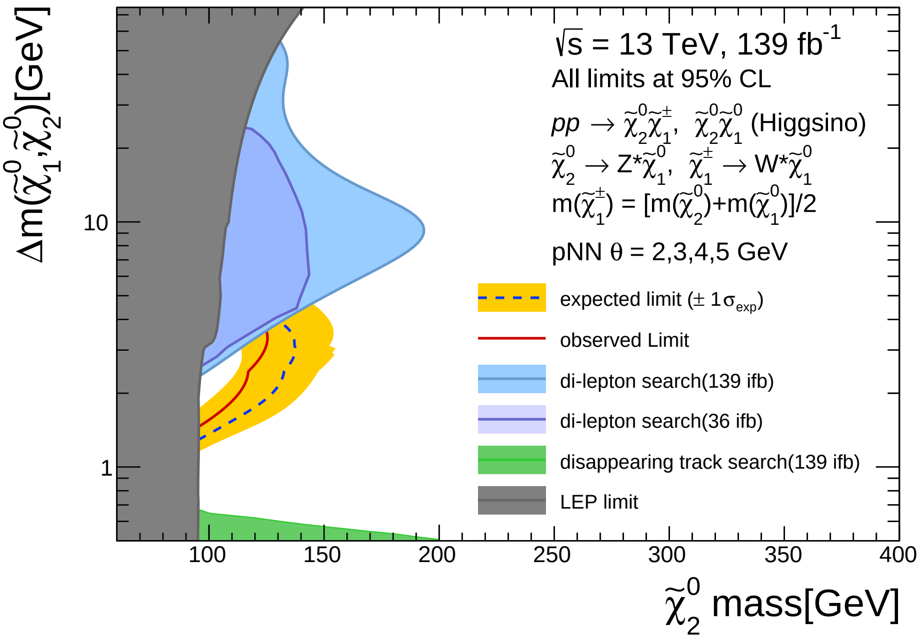

Figure11.4 exclusion contours in highest sensitivity for the Higgsino like LSP scenario. The red line is observed limit, and the blue dashed line shows the nominal value of the expected exclusion contour. The yellow band represents the uncertainty of ± 1 σ. The Higgsino scenario is excluded up to 125 GeV in $\tilde{\chi}_2^0$ and down to 1.4 GeV in Δm.

muon ID, but only the higher p_T muon does. The efficiency for the lower p_T muon for the standard muon ID becomes higher in the larger Δm region. It means that events may not be classified as 1 standard muon and 1 LCaT muon. This is why the sensitivity decrease for larger Δm. On the other hand, in the smaller Δm region, the higher p_T muon cannot be identified as a standard muon because its p_T is low. As a result, the sensitivity decreases also for smaller Δm region.

The third is the efficiency of the LCaT muon ID. As seen in Figure 6.14, the efficiency of LCaT muon ID has a peak around 3 GeV. Therefore, when Δm is small, the lower p_T muon with p_T less than 2 GeV becomes dominant, and the sensitivity decreases. Similarly, when Δm is large, the lower p_T muon with p_T higher than 2 GeV increases, and sensitivity decreases.

Due to the balance of the above three factors, the highest sensitivity is given at 3 GeV.

11.4 Impact on pMSSM

This section describes the scenario of pMSSM when neutralino is present in the expected exclusion contour discussed in section 11.3. For the evaluation of dark matter, `MiscOMEGAs`[68] is used, and `FeynHiggs`[69] is used for the evaluation of the mass of SM higgs boson. In addition, muon magnetic anomaly is evaluated using `GM2Calc`[70].

11.4.1 Higgsino like LSP scenario

To evaluate the Higgsino like LSP scenario, we have scanned parameters of the model for ranges are summarized in table 11.6. The relic density of the dark matter ($\Omega_{DM}h^2$) is known to be 0.12, and the mass of the SM higgs boson is 124.97 ± 0.24 GeV[71]. The entries, which $\Omega_{\tilde{\chi}_1^0}h^2$ is less than 0.12 and the mass of the SM Higgs is in agreement with the measurement in LHC experiments within the error, are shown as black dots in Figure 11.5. The muon magnetic anomaly observed in the Fermilab Muon g-2 Experiment is a_μ(Exp) - a_μ(SM) = $(251 \pm 59)\times 10^{-11}$ ($a_\mu \equiv (g_\mu - 2)/2$) [7]. The entries that can explain the muon magnetic anomaly within the error are shown as blue dots in Figure 11.5. In addition, the entries that satisfy the above three conditions and are excluded by the 1 standard muon + 1 LCaT muon search are shown as red dots.

Table11.6 Range of the pMSSM parameter for Higgsino like LSP scenario

parameter	range	parameter	range
$\tan\beta$	[1, 200]	$m_{\tilde{l}R}$	[0, 1000]
M_A	[0, 5000]	$m_{\tilde{Q}L}$	[0, 2000]
μ	[100, 500]	$m_{\tilde{t}R}$	[0, 2000]
M_1	[100, 5000]	$m_{\tilde{b}R}$	[0, 2000]
M_2	[100, 5000]	$m_{\tilde{\tau}L}$	[0, 2000]
M_3	[1000, 10000]	$m_{\tilde{\tau}R}$	[0, 2000]
$m_{\tilde{q}L}$	[1000, 5000]	A_t	[-8000, 8000]
$m_{\tilde{u}R}$	[1000, 5000]	A_b	[-2000, 2000]
$m_{\tilde{d}R}$	[1000, 5000]	A_τ	[-2000, 2000]
$m_{\tilde{l}L}$	[0, 1000]		

Under the same conditions as in Figure 11.5, the distribution in μ - $\tilde{\chi}_1^0$ mass plane is shown in (a) of Figure 11.6. Also, the distributions in μ - $\Omega_{\tilde{\chi}_1^0}h^2$ planes are shown in (b) of figure 11.6. In the small Δm region, the $\tilde{\chi}_1^0$ mass is strongly dependent on μ. As shown in (a) of figure 11.6, exclusion of the Higgsino like LSP in the region from 90 GeV to 125 GeV in $\tilde{\chi}_1^0$ mass is equivalent to exclude the Higgsino like LSP in the region from 90 to 125 GeV in μ. Additionally, Dark matter is also evaluated ((b) of figure 11.6). $\Omega_{\tilde{\chi}_1^0}h^2$ is also strongly depend on μ.

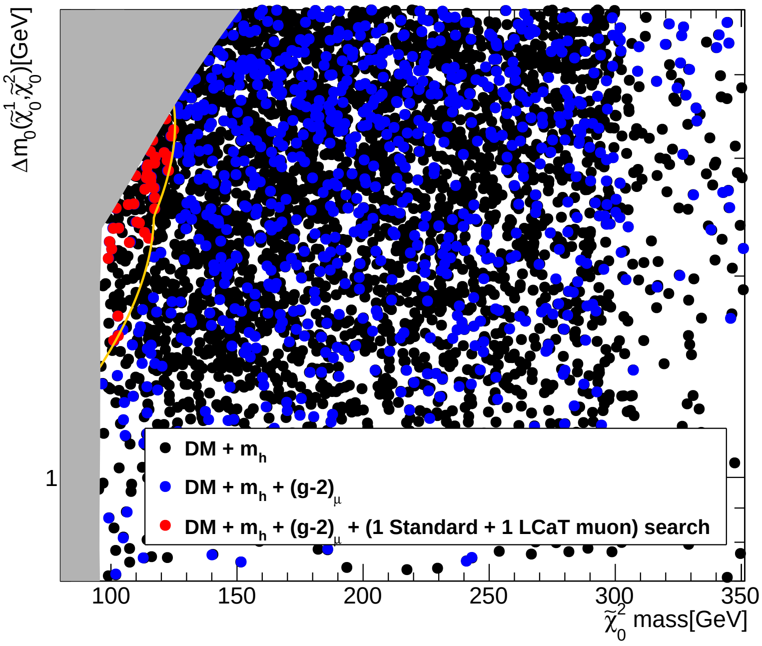

Figure11.5 The result of the parameter scan in the Higgsino like LSP scenario. The black dots are entries that satisfy the conditions of dark matter and SM higgs mass. The blue dots are the entries that can additionally explain the muon magnetic anomaly out of the black dots. The red dots are the entries out of the blue dots and excluded contour by 1 standard muon + 1 LCaT muon search. The gray area indicates the area that has already been excluded, and the orange line shows the exclusion contour of the SL search.

The excluded region by the 1 standard muon + 1 LCaT muon search corresponds to the region where two % of DM is $\tilde{\chi}_1^0$ and the remaining 98% consists of other particles. Therefore, It is suggested that the scenario in which DM is consisted by Higgsino like LSP and another particle such as SUSY axion [72] should contain $\tilde{\chi}_1^0$ at least 2%.

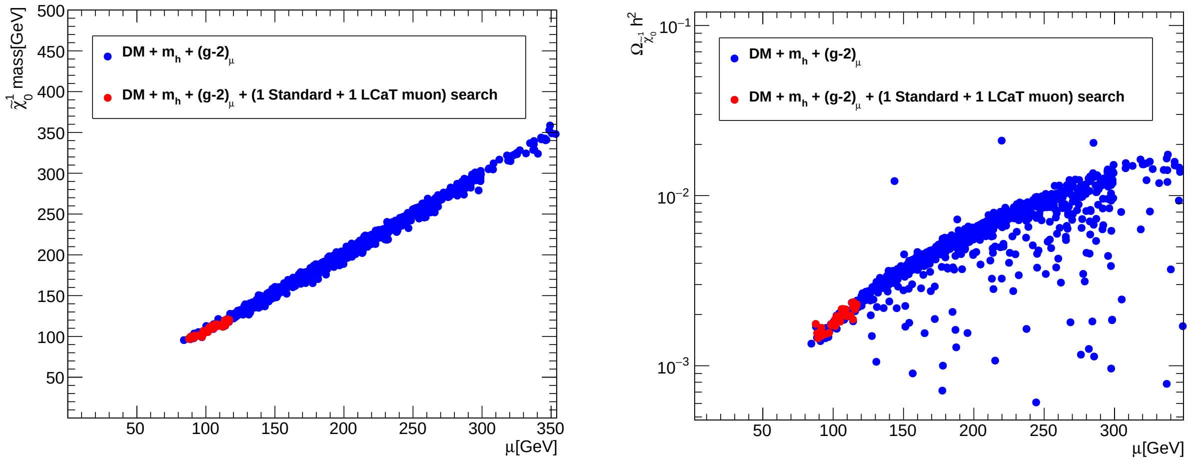

(a) μ - $\tilde{\chi}_1^0 mass$ plane

(b) μ - Ωh^2 plane

Figure11.6 The result of Higgsino like LSP scenario in μ -$\tilde{\chi}_1^0 mass$ plane (left) and μ - Ωh^2(right). The color coding is same as figure11.5.

12. Conclusion

A search for neutralinos using 139 fb^{-1} of pp collision data at $\sqrt{s}$ = 13TeV collected in the LHC-ATLAS experiment is presented in this thesis. Production of neutralinos where a $\tilde{\chi}_2^0$ decays into a $\tilde{\chi}_1^0$ and two muons are searched. Especially, we have focused a unexplored scenario where $\Delta m(\tilde{\chi}_2^0, \tilde{\chi}_1^0)$ is between 1 and 5 GeV.

The search neutralinos with small Δm regions was a very challenging analysis for the following three reasons. First, low-p_T muons is dominant and the muon identification efficiency is low in the low-p_T region. Second, it is not easy to develop an analysis method that is optimized for all the Δm regions from 1 to 5 GeV since the kinematics of the signal varies greatly depending on Δm. Third, the difference between MC simulation and data is large in the low-p_T region. It makes it difficult to use MC simulation for background estimation.

In order to solve these difficulties, a new DNN-based low-p_T muon dedicated algorithm using the calorimeter information has been developed to improve the poor identification efficiency for the low-p_T muons. Its efficiency is 2 to 10 times of conventional methods. Additionally, high sensitivity for a wide Δm region can be accomplished by using pNN with Δm as input. Furthermore, an all data-driven background estimation method that applies the LCaT muon weight to anti-LCaT muon ID events is developed for background estimation. It enables background estimation with small systematic errors.

As a result, no significant excess over the estimated background has observed. Therefore, the exclusion limits to the Higgsino-like LSP scenario at the 95% confidence level have been calculated. The limit reaches a maximum of 125 GeV in $\tilde{\chi}_2^0$ and 1.4 GeV in $\Delta m(\tilde{\chi}_2^0, \tilde{\chi}_1^0)$. This is the result of the world's highest sensitivity. This result limits the parameters of the pMSSM with Higgsino like LSP scenario. Higgs mass parameter (μ) is rejected up to 125 GeV, and it is suggested that more than 2% of Higgsino like LSP is contained in the dark matter.

Acknowledgement

The experience of working at the forefront of particle physics during my master and doctoral course was undoubtedly the most valuable one of my life. I would like to express my sincere gratitude to the many people who have helped me to write this thesis. In particular, I would like to thank the following people.

First of all, I would like to express my gratitude to Hisaya Kurasige, who is my supervisor and gave me much advice for my analysis. He allowed me to do my research freely, and when I got stuck, he pushed my research forward with good advice. I am always surprised how he knew so much about everything from experiments to theories. Also, I would like to thank him for inviting me to Kobe University for my doctoral course. It gave me a lot of good experiences and wonderful encounters. I would like to also express my gratitude to Yuji Yamazaki and Junpei Maeda. Yuji Yamazaki was the Kobe staff member who gave many comments at the ATLAS Kobe meeting. Thanks to him, the meeting was very fruitful. Junpei Maeda is a staff who gave me a lot of technical support in physics analysis and the development of trigger simulation. Also, when I was tired or not, I could relax with a casual conversation with you. I am grateful for that.

I would appreciate the ATLAS Japan SUSY group. Tomoyuki Saito has been my support staff for six years, from undergraduate to doctoral courses. He has always been accommodating in discussing when my research was going well and when I was facing difficulties. Thanks to the discussion, I could achieve the solution. Furthermore, as the most important one, I had the most fun meeting with him. Shion Chen is the staff member who inspired me to do this research and gave me various advice on physics analysis. He understood my situation right away and gave me accurate comments each time. Thanks to this advice, I could do my research smoothly.

I greatly appreciate Michael Holzbock and Jeff Shahinian, the Compressed EWK SUSY group members, for their help and support. Despite my poor English, they always gave me critical questions and advice. Thank you very much for guiding me in the right direction under the difficult situation of COVID-19.

I am grateful to the staff at Shinshu University, Tohru Takeshita and Yoji Hasegawa. My first step as a researcher began at Shinshu. I could complete this research because I have an experience of enjoyable research life in Shinshu. I did my research in Kobe in the doctoral course, but my spirit as a researcher is in Shinshu. I would like to thank you again.

I would also like to express my thanks to my senior co-workers for the ATLAS experiment. In particular, I would like to thank Kenta Uno and Kosuke Takeda for teaching me not only physics analysis techniques, but also how to live CERN, how to enjoy alcohol, and many other things. All of them colored up my life at CERN. I am looking forward to having another drinking party that will make me lose my belt and destroy a toilet.

I much appreciate the colleague in the ATLAS experiment. Especially, Shota Hayashida, who is always called "RINRIN" by me, is the best colleague and the person I respect. His stoicism as a researcher amazes me every day and inspires me to keep hard work. Also, I remember clearly the day when we went on trips, had fun drinking parties, and talked until midnight on holidays. All of them are wonderful memories. I am grateful to have been blessed with a good colleague.

I would like to offer my special thanks to my junior co-workers at Kobe University. It is sad that I could not go to CERN for a long time due to COVID-19, but I am sure that I could have a more enjoyable research life in Kobe thanks to them. Takahiro Shiomi is the junior co-worker ,who had many discussions with me. The development and discussion of the trigger algorithm with him were always fun, and I was amazed at the speed of his growth. The statistical treatment that I studied with him was also very helpful in writing this thesis. Kohei Taniguchi is the best junior co-worker. I remember every detail of that day when we went to hot springs and camping together, I took him to drink parties until midnight, he taught me how to play the guitar. I have too many fun memories with him to list here. These gave me the energy to push forward my research. Genichiro Sumi is the junior co-worker with whom I spent a long time in the meeting room at night. While others were living a healthy life, he was always working at night. So when I was working at night, I was always chatting with him, and it was unstoppable. I am not sure if it helped my research progress, but I am sure that I had a good time. Kosuke Sueda was the junior co-worker who often went drink parties with me. His crazy drinking behavior was always impressive, and he inspired me in my life at Kobe and CERN. I would also like to thank Ryuici Ueno, Takuya Shimada, and Shotaro Yamamoto. I played Murder Mystery, practiced guitar, and talked all night with them. All of the memories are very good memory.

I would also like to thank the following people for sharing their computing resources with me and supporting my research not only mentally but also physically. Takahiro Shiomi, Kohei Taniguchi, Genichiro Sumi, Natsu Teramura, Ryutaro Ikemori. I would like to send a special thanks to them.

Of course, I would like to thank all members of Kobe University. Thank you for welcoming

me. Also, they told me a lot about the culture of Kobe University and their research, except for the ATLAS experiment. I appreciate them.

Finally, I would like to thank my family for their support. I would not have been able to write this paper without their support. I would like to express my deepest gratitude.

Bibliography

[1] G. Aadet al.[ATLAS collaboration]. Luminositypublicresultsrun2. `https://twiki.cern.ch/twiki/bin/view/AtlasPublic/LuminosityPublicResultsRun2`.

[2] G. Aad *et al.* [ATLAS]. The atlas experiment at the cern large hadron collider. JINST **3**, S08003, 2008.

[3] M. Aaboud *et al.* [ATLAS]. Performance of the atlas trigger system in 2015. Eur. Phys. J. C **77**, no.5, 317, 2017.

[4] R. D. Ball *et al.* [NNPDF]. Parton distributions from high-precision collider data. Eur. Phys. J. C **77**, no.10, 663, 2017.

[5] Alan D. Martin Francis Halzen. Quarks and Leptons: An Introductory Course in Modern Particle Physics. 1984.

[6] S. P. Martin. A supersymmetry primer. Adv. Ser. Direct. High Energy Phys. **18**, 1-98.

[7] B. Abi *et al.* [Muon g 2]. Measurement of the positive muon anomalous magnetic moment to 0.46 ppm. Phys. Rev. Lett. **126**, no.14, 141801.

[8] Aleph, delphi, l3, opal experiments, combined lep chargino results, up to 208 gev for low dm. LEPSUSYWG/02-04.1, 2002. `http://lepsusy.web.cern.ch/lepsusy/www/inoslowdmsummer02/charginolowdm_pub.html`.

[9] G. Aad *et al.* [ATLAS collaboration]. Searches for electroweak production of supersymmetric particles with compressed mass spectra in $\sqrt{s} = 13$ tev pp collisions with the atlas detector. Phys. Rev. D **101**, no.5, 052005, 2020.

[10] G. Aad *et al.* [ATLAS]. Search for long-lived charginos based on a disappearing-track signature using 136 fb^{-1} of pp collisions at $\sqrt{s} = 13$ tev with the atlas detector. ATLAS-CONF-2021-015, 2021.

[11] Ian Goodfellow, Yoshua Bengio, and Aaron Courville. Deep Learning. MIT Press, 2016. `http://www.deeplearningbook.org`.

[12] P. W. Higgs. Broken Symmetries and the Masses of Gauge Bosons. Phys. Rev. Lett. **13**, 508-509, 1964.

[13] F. Englert and R. Brout. Broken Symmetry and the Mass of Gauge Vector Mesons. Phys. Rev. Lett. **13**, 321-323, 1964.

[14] J. T. Ruderman M. Papucci and A. Weiler. Natural susy endures. JHEP **09**, 035.

[15] S. Robles K. Rolbiecki J. A. Casas, J. M. Moreno and B. Zaldívar. What is a natural susy scenario? JHEP **06** 070, 2015.

[16] F. Zwicky. On the masses of nebulae and of clusters of nebulae. Astrophys. J., 86:217–246, 1937.

[17] W. Kent and Norbert Thonnard Vera C. Rubin, Jr. Ford. Extended rotation curves of high-luminosity spiral galaxies. iv. systematic dynamical properties. Sa through Sc.Astrophys. J. Lett., 225:L107–L111, 1978.

[18] E. Corbelli and P. Salucci. The extended rotation curve and the dark matter halo of m33. Mon. Not. Roy. Astron. Soc. **311**, 441-447, 2000.

[19] M. M. Nojiri J. Hisano, S. Matsumoto and O. Saito. Direct detection of the wino and higgsino-like neutralino dark matters at one-loop level. Phys. Rev. D **71**, 015007, 2005.

[20] E. Aprile *et al.* [XENON]. Dark matter search results from a one ton-year exposure of xenon1t. Phys. Rev. Lett. **121**, no.11, 111302.

[21] G. W. Bennett *et al.* [Muon g 2]. Final Report of the Muon E821 Anomalous Magnetic Moment Measurement at BNL. Phys. Rev. D **73**, 072003, 2006.

[22] M. Benayoun-J. Bijnens T. Blum M. Bruno I. Caprini C. M. Carloni Calame M. Cè T. Aoyama, N. Asmussen and *et al.* G. Colangelo. The anomalous magnetic moment of the muon in the Standard Model. Phys. Rept. **887**, 1-166, 2020.

[23] T. Moroi. The Muon anomalous magnetic dipole moment in the minimal supersymmetric standard model. Phys. Rev. D **53**, 6565-6575, 1996.

[24] S. P. Martin and J. D. Wells. Muon Anomalous Magnetic Dipole Moment in Supersymmetric Theories. Phys. Rev. D **64**, 035003, 2001.

[25] M. Badziak and K. Sakurai. Explanation of electron and muon g − 2 anomalies in the MSSM. JHEP **10**, 024, 2019.

[26] S. Heinemeyer M. Chakraborti and I. Saha. Improved $(g-2)_\mu$ measurements and wino/higgsino dark matter. Eur. Phys. J. C **81**, no.12, 1069, 2021.

[27] M. Klasen A. Aboubrahim and P. Nath. What the fermilab muon g−2 experiment tells us about discovering supersymmetry at high luminosity and high energy upgrades to the lhc. Phys. Rev. D **104**, no.3, 035039, 2021.

[28] G. Aad *et al.* [ATLAS]. Search for long-lived charginos based on a disappearing-track signature using 136 fb^{-1} of pp collisions at $\sqrt{s}$= 13 tev with the atlas detector. ATLAS-CONF-2021-015. `https://cds.cern.ch/record/2759676`.

[29] L. Evans and P. Bryant. LHC Machine. JINST **3**, S08001, 2008.

[30] Joao Pequenao. Computer generated image of the whole atlas detector. `https://cds.cern.ch/record/1095924?ln=ja`.

[31] G. Aad *et al.* [ATLAS]. ATLAS Insertable B-Layer Technical Design Report. ATLAS-TDR-19, 2010. `https://cds.cern.ch/record/129163`.

[32] Joao Pequenao. Computer generated image of the atlas inner detector. `https://cds.cern.ch/record/1095926?ln=ja`.

[33] Joao Pequenao. Computer generated image of the atlas calorimeter. `https://cds.cern.ch/record/1095927?ln=ja`.

[34] Joao Pequenao. Computer generated image of the atlas muons subsystem. `https://cds.cern.ch/record/1095929`.

[35] M. G. Pia and G. Weidenspointner. Monte Carlo Simulation for Particle Detectors. arXiv:1208.0047 [physics.comp-ph].

[36] R. D. Ball *et al.* [NNPDF]. Parton distributions for the LHC Run II. JHEP **04**, 040.

[37] F. Krauss-M. Schonherr S. Schumann F. Siegert T. Gleisberg, S. Hoeche and J. Winter. Event generation with SHERPA 1.1. JHEP **02**, 007, 2009.

[38] S. Carrazza C. S. Deans L. Del Debbio S. Forte A. Guffanti N. P. Hartland J. I. Latorre R. D. Ball, V. Bertone and *et al.* J. Rojo.

[39] C. Oleari S. Alioli, P. Nason and E. Re. A general framework for implementing NLO calculations in shower Monte Carlo programs: the POWHEG BOX. JHEP **06**, 043, 2010.

[40] ATLAS Collaboration. A study of different colour reconnection settings for Pythia8 generator using underlying event observables. ATL-PHYS-PUB-2017-008, 2017. `https://cds.cern.ch/record/2262253(cit.onp.39)`.

[41] ATLAS Collaboration. ATLAS Computing: technical design report.

[42] S. Agostinelli et al. GEANT4 - a simulation toolkit. Nucl. Instrum. Meth. A 506, 2003.

[43] ATLAS Collaboration. Studies on top quark Monte Carlo modelling with Sherpa and MG5_aMC@NLO. ATL-PHYS-PUB-2017-007, 2017.

[44] O. Mattelaer P. Artoisenet, R. Frederix and R. Rietkerk. Automatic spin-entangled decays of heavy resonances in Monte Carlo simulations. JHEP **03**, 015, 2013.

[45] A. Rosenfeld and J. Faltz. Sequential Operations in Digital Picture Processing. Journal of the ACM, 1966.

[46] R. Fruhwirth. Application of kalman filtering to track and vertex fitting. Nucl. Instrum. Meth. A **262**, 444-450, 1987.

[47] M. Aaboud *et al.* [ATLAS]. Performance of the ATLAS Track Reconstruction Algorithms in Dense Environments in LHC Run 2. Eur. Phys. J. C **77**, no.10, 673, 2017.

[48] S. Boutle *et al.* [ATLAS]. Primary vertex reconstruction at the ATLAS experiment. J. Phys. Conf. Ser. **898**, no.4, 042056, 2017.

[49] G. Aad *et al.* [ATLAS collaboration]. Topological cell clustering in the atlas calorimeters and its performance in lhc run 1. Eur. Phys. J. C **77**, 490.

[50] M. Aaboud *et al.* [ATLAS]. Jet reconstruction and performance using particle flow with the

ATLAS Detector. Eur. Phys. J. C **77**, no.7, 466, 2017.

[51] G. P. Salam M. Cacciari and G. Soyez. The anti-k_t jet clustering algorithm. JHEP **04**, 063, 2008.

[52] G. Aad *et al.* [ATLAS]. Jet energy scale and resolution measured in proton–proton collisions at $\sqrt{s} = 13$ tev with the atlas detector. Eur. Phys. J. C **81**, no.8, 689, 2021.

[53] ATLAS Collaboration. Expected performance of the ATLAS b-tagging algorithms in Run-2. ATL-PHYS-PUB-2015-022. `http://cds.cern.ch/record/2037697`.

[54] G. Aad *et al.* [ATLAS]. ATLAS b-jet identification performance and efficiency measurement with $t\bar{t}$ events in pp collisions at $\sqrt{s} = 13$ TeV. Eur. Phys. J. C **79**, no.11, 970, 2019.

[55] G. Aad *et al.* [ATLAS collaboration]. Muon reconstruction and identification efficiency in atlas using the full run 2 *pp* collision data set at $\sqrt{s} = 13$ tev. Eur. Phys. J. C **81**, 578, 2021.

[56] N. M. Koehler [ATLAS]. ATLAS Muon Reconstruction Performance in LHC Run 2. ATL-PHYS-PROC-2015-186, 2015.

[57] M. Aaboud *et al.* [ATLAS]. Electron reconstruction and identification in the ATLAS experiment using the 2015 and 2016 LHC proton-proton collision data at $\sqrt{s} = 13$ TeV. Eur. Phys. J. C **79**, no.8, 639, 2019.

[58] M. Aaboud *et al.* [ATLAS]. Performance of missing transverse momentum reconstruction with the ATLAS detector using proton-proton collisions at $\sqrt{s} = 13$ TeV. ur. Phys. J. C **78**, no.11, 903, 2018.

[59] C. Di Donato [ATLAS]. Muon identification and performance in the atlas experiment. PoS **BEAUTY2018**, 068, 2018.

[60] G. Aad *et al.* [ATLAS collaboration]. Performance of the missing transverse momentum triggers for the atlas detector during run-2 data taking. JHEP **08**, 080, 2020.

[61] T. Faucett P. Sadowski P. Baldi, K. Cranmer and D. Whiteson. Parameterized neural networks for high-energy physics. Eur. Phys. J. C **76**, no.5, 235, 2016.

[62] P. Motylinski L. A. Harland-Lang, A. D. Martin and R. S. Thorne. Parton distributions in the LHC era: MMHT 2014 PDFs. Eur. Phys. J. C **75**, no.5, 204, 2015.

[63] J. Gao M. Guzzi J. Huston P. Nadolsky J. Pumplin C. Schmidt D. Stump S. Dulat, T. J. Hou and C. P. Yuan. New parton distribution functions from a global analysis of quantum chromodynamics. Phys. Rev. D **93**, no.3, 033006, 2016.

[64] G. Cabras D. Caforio N. Dehghanian A. Floderus B. Giacobbe F. Giannuzzi F. Giorgi G. Avoni, M. Bruschi and *et al.* P. Grafström.

[65] E. Gross G. Cowan, K. Cranmer and O. Vitells. Asymptotic formulae for likelihood-based tests of new physics. Eur. Phys. J. C **71**, 1554, 2011.

[66] CMS ATLAS and LHC Higgs Combination Group. Procedure for the lhc higgs boson search

combination in summer 2011. CMS-NOTE-2011-005.

[67] [ATLAS]. Formulae for estimating significance. ATL-PHYS-PUB-2020-025. `https://cds.cern.ch/record/2736148`.

[68] A. Mjallal G. Belanger and A. Pukhov. Recasting direct detection limits within micromegas and implication for non-standard dark matter scenarios. Eur. Phys. J. C **81**, no.3, 239, 2021.

[69] N. Murphy H. Bahl and H. Rzehak. Hybrid calculation of the mssm higgs boson masses using the complex thdm as eft. Eur. Phys. J. C **81**, no.2, 128, 2021.

[70] H. G. Fargnoli C. Gnendiger R. Greifenhagen J. h. Park S. Paßehr D. St P. Athron, M. Bach.

[71] M. Aaboud *et al.* [ATLAS]. Measurement of the higgs boson mass in the $h \to zz^* \to 4\ell$ and $h \to \gamma\gamma$ channels with $\sqrt{s} = 13$ tev pp collisions using the atlas detector. Phys. Lett. B **784**, 345-366, 2018.

[72] H. Baer K. J. Bae and E. J. Chun. Mixed axion/neutralino dark matter in the susy dfsz axion model. JCAP **12**, 028, 2013.